Classifying Retinal Ganglion Cells for Bionic Vision

Dissertation

zur Erlangung des Grades eines
Doktors der Naturwissenschaften

der Mathematisch-Naturwissenschaftlichen Fakultät
und
der Medizinischen Fakultät
der Eberhard-Karls-Universität Tübingen

vorgelegt

von

Hamed Shabani

aus Shiraz, Iran

2021

Tag der mündlichen Prüfung: September 29th, 2021

Dekan der Math.-Nat. Fakultät: Prof. Dr. Thilo Stehle

Dekan der Medizinischen Fakultät: Prof. Dr. Bernd Pichler

1. Berichterstatter: Prof. Dr. Eberhart Zrenner

2. Berichterstatter: Prof. Dr. Stefan Liebau

Prüfungskommission: Prof. Dr. Eberhart Zrenner

Prof. Dr. Stefan Liebau

Jun.-Prof. Dr. Anna Levina

PD Dr. Rer. Nat. Habil. Zohreh Hosseinzadeh

Declaration:

Ich erkläre, dass ich die zur Promotion eingereichte Arbeit mit dem Titel: *"Classifying Retinal Ganglion Cells for Bionic Vision"*. selbständig verfasst, nur die angegebenen Quellen und Hilfsmittel benutzt und wörtlich oder inhaltlich übernommene Stellen als solche gekennzeichnet habe. Ich versichere an Eides statt, dass diese Angaben wahr sind und dass ich nichts verschwiegen habe. Mir ist bekannt, dass die falsche Abgabe einer Versicherung an Eides statt mit Freiheitsstrafe bis zu drei Jahren oder mit Geldstrafe bestraft wird.

I hereby declare that I have produced the work entitled *"Classifying Retinal Ganglion Cells for Bionic Vision".*, submitted for the award of a doctorate, on my own (without external help), have used only the sources and aids indicated and have marked passages included from other works, whether verbatim or in content, as such. I swear upon oath that these statements are true and that I have not concealed anything. I am aware that making a false declaration under oath is punishable by a term of imprisonment of up to three years or by a fine.

Tübingen, den   ....
                                    Datum/Date   Unterschrift/Signature

Statement of contributions according to § 9 (2):

This project is carried out under the supervision of Prof. Zrenner, Dr. Rathbun, and Dr. Hosseinzadeh. Chapters 1-4 were written by Hamed Shabani. Useful comments and feedback were received from Daniel Rathbun and Zohreh Hosseinzadeh for recording and analysing data and during writing the thesis. Chapter 2 includes electrophysiological signals and calcium imaging traces of retinal ganglion cells. Electrophysiological data provided in this chapter are mainly recorded by Hamed Shabani. Daniel, Rathbun, Zohreh Hosseinzadeh and Klaudija Masarini also contributed to data collection and experiment preparation. Pre- and post- processing of data, including spike sorting and writing Matlab scripts, were carried out by Hamed Shabani. The calcium imaging data used in chapter 2 was provided by Baden et al., and is freely available on https://datadryad.org website. The OGB kernel used to estimate pseudo-calcium traces was provided by Yannik Bauer via personal communications. The electrical noise was made by Dr. Sudarshan Sekhar. Chapter 3 includes electrophysiological retinal ganglion cells. Electrophysiological data provided in this chapter were mainly recorded by Hamed Shabani. Dr. Daniel Rathbun, Dr. Zohreh Hosseinzadeh and Klaudija Masarini contributed to data collection and experiment preparation. Pre- and post- processing of data, including spike sorting and writing Matlab and python scripts, were carried out by Hamed Shabani. For the perspective paper, included as an appendix, Hamed Shabani contributed to the text and wrote Matlab scripts for simulating ganglion cell spiking responses (figure 1 of Appendix).

ABSTRACT

Current retinal implants implement pulsate stimuli to activate the neural circuits of the retina. This type of stimulation can activate antagonist retinal pathways which lead to improper perception of the visual scene. Developing a precise stimulation strategy with the ability to preferentially target retinal neural circuits is one of the alternative methods to improve the accuracy of restored vision. Previous studies tried to decipher the electrical properties of different retina ganglion cell (RGC) types by applying electrical Gaussian noise and estimating the electrical input filter of the cells. Sekhar et al reported that ON and OFF cells have different electrical input filters. In this study we aimed to pursue the same goal by using a similar approach to assess the electrical profiles for a wider range of ganglion cell types. We implemented an array of visual stimuli along with an electrical noise stimulus to fully characterize the light and electrical response properties of both healthy and degenerated retina ganglion cells.

The extracellular activity of ganglion cells were recorded using microelectrode arrays and cells were clustered using two different clustering frameworks. In the first attempt, the spiking activity of each cell was converted to pseudocalcium traces by convolving each spike train with a temporal kernel. Response features were extracted using sparse principal component analysis to project the data into a lower-dimensional space. Each RGC projection was assigned to one of the 39 RGC clusters reported by Baden et al. which mapped onto about half of the previously described clusters. Difficulty of matching spike train data to calcium imaging data encouraged us to use a different clustering framework in which a hierarchical clustering algorithm was implemented to cluster cells based on their visual and electrical induced responses. The light based clustering was performed on the spike time based distance matrices and detected 37 and 12 clusters for wild-type and rd10 retina, some of which showed a strong correlation between the cell types and the shape of electrical input filters. In addition to that, a separate hierarchical clustering of electrical input filters showed that clusters with upward input filters reflect the activity of ON cells and clusters with downward deflections are mostly representative of OFF and ON-OFF cells. Moreover, pharmacological manipulation of degenerated retina revealed that input filters with downward deflection were removed by blocking the synaptic connection between photoreceptors and On-bipolar cells, while electrical input filters with upward deflection were subjected to smaller changes after blocking this circuit. The pharmacological manipulation was performed only on degenerated retina and was limited to the blockage of only one pathway,

which did not reveal conclusive results to interpret how different retinal pathways contribute to the generation of upward and dwonward input filters. Further experiments on wild-type retina by implementing different pharmacological blockers is required to fully inspect the effect of subthreshold noise stimulation on each retinal pathway. Although theses results have not met our expectation of finding a larger diversity among the electrical input filters of ON and OFF ganglion cell subtypes, they may provide useful information to better understand the circuit mechanism leads to the generation of upward and downward electrical input filters and help to leverage the stimulation performance in retinal implants.

TABLE OF CONTENTS

INTRODUCTION

In 2015 there were over 200 million people around the world suffering from blindness or visual impairments; of those 36 million were blind [1]. Visual disorders can be caused by damage or disease in the optical and retinal parts of the eye, parts of visual pathways or the visual cortex. Retinitis Pigmentosa (RP) and Age-Related Macular Degeneration (AMD) are among the most common forms of progressive retinal degeneration [2] that can lead to blindness. Although several therapies such as gene therapy, stem cell, and treatment based on optogenetics methods have been suggested to cure or slow down the progress of these types of retinal degeneration, retinal prosthetics have shown the most successful results in restoring vision so far. In this method, electrical stimulation of neurons induces bright spots in patients' perception called phosphenes. By using an array of electrodes and proper stimulation of the cells it is possible to reconstruct meaningful two-dimensional patterns of phosphenes. In the last two decades, a growing body of research has been dedicated to the development of state-of-the-art electrode-based visual prosthesis technologies. Consequently, the field witnessed substantial progress in the development of implantable devices with the ability to restore vision [3]. The success of cochlear implants in the market motivated research teams around the world to develop commercial retinal prosthetics with regulatory approval. However, financial issues, in addition to falling short of expectations in long-term usages, made them stop providing their products on the market, indicating that still more basic research is required to develop visual prostheses with the ability to restore high acuity vision. Hardware limitation is not the only challenge in designing visual prostheses. Gaining more knowledge about retinal coding and translating that to retinal prosthetics' application is one of the essential steps in improving the quality of artificial vision. This will help to find better stimulation strategies for designing the next generation of retinal prosthetics. Amplitude, phase, shape duration, and stimulation paradigm -voltage or current

controlled-, are some other factors that must be considered for having a robust stimulation. Several studies have been conducted to find the parameter for designing the optimum stimulus. However, finding the proper coding strategy for stimulation so that it sends a pattern of action potential to the brain, similar to the natural pattern of a healthy retina, is another challenge that has not been addressed very well. In this study, In line with the recent study of Sekhar et al [4, 5], we aim to find the optimum stimulus of different ganglion cell types by using electrical noise stimulation.

1.1   Retina

The human retina is approximately 0.5 mm thick and located in the back of the eye with three layers of cell bodies and two layers of synapses. The density of cones in the central part of the retina is higher than the peripheral, this is why the center of the retina is thicker than the peripheral part. The peripheral part of the retina is more dominated by rods and cones are mostly located at the center [6]. The location of rods and cones is called the outer nuclear layer. The inner nuclear layer consists of Bipolar Cells (BC), Amacrine Cells (AC), and Horizontal Cells (HC). The location of Retinal Ganglion Cells (RGCs) and displaced Amacrine Cells (d-AC) is called the ganglion cell layer. The connection between rods and cones, with BCs and HCs, is known as the Outer Plexiform Layer (OPL). The layer where the processed information from BCs is conveyed to the RGCs is named the Inner Plexiform Layer (IPL). ACs make synaptic connections with BCs and affect their output at this layer. Ganglion cells convert neurochemical signals into binary format and send them to the brain via the optic nerve [6] (figure 1.1).

1.1.1   Photoreceptors

Photoreceptors (PR) absorb light photons and translate them into electrochemical signals, which are then sent to the OPL via the first synaptic layer of the retina. The mammalian retina consists of two or three types of cones and one type of rod photoreceptors. Cones are more prevalent in the center of the retina and construct the basis of color vision. Depending on their opsins structures, visual pigments of cones are sensitive to three different spectra of light, ranging from long light wavelengths with a peak around 560nm (red), to medium wavelengths that have a peak around 530nm (green) and also short light wavelength peaking at 420nm (blue). Rods are more sensitive than cones and are specialized for dim light detection. They have visual pigment-rhodopsin, sensitive to blue-green light, with the highest sensitivity around 500 nm wavelengths of light [7].

1.1.2   Bipolar cells

Bipolar cells receive parallel information from photoreceptors and send the pre-processed information to the inner retina via excitatory inputs [8]. The other side of BC branches to the IPL layer and synapses onto RGCs and ACs. Eleven different types of BC are reported in mammalian
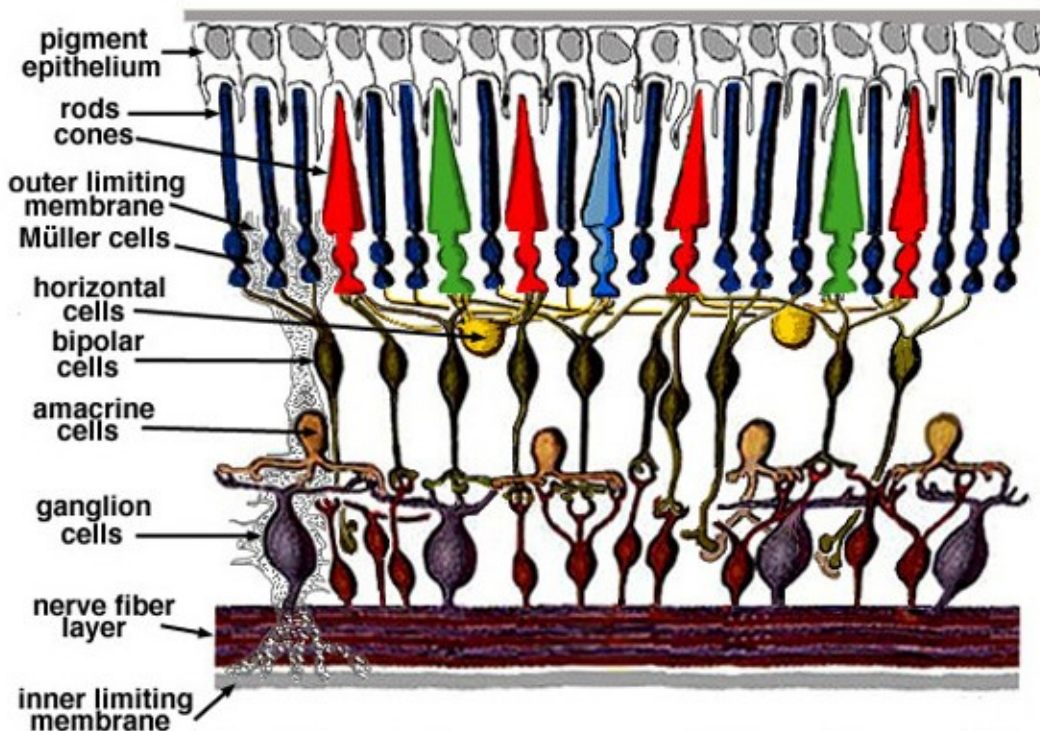
Figure 1.1: Structure of different layers in the retina. Image is taken from http://webvision.med.utah.edu/ [6]

retinas. Most of them are ON-BC. Dendritic morphology, shape, and IPL stratification are the most important ways to distinguish types of BCs [8]. BCs with a connection to cones are called Cone Bipolar cells (CBC) and those that receive signals from rods are named Rod Bipolar cells (RBC). ON-BCs depolarize in response to the light onset whereas OFF-BCs depolarize in response to light off-set [8]. ON-CBC are connected to cones via an inverting connection from one side and send input to ON-Ganglion cells from the other side. Cone OFF pathways have connection to OFF-CBCs via non inverting connections providing input to OFF-Ganglion cells ON-CBC are connected to cones via an inverting connection from one side and send input to ON-Ganglion cells on the other side. Cone OFF pathways have connection to OFF-CBCs via non inverting connec- tion s providing input to OFF-Ganglion cells [9]. RBCs do not have a direct connection to RGCs and their outputs go to RGCs through AII ACs. The output of AII ACs provides sign-inverting glycinergic input onto OFF-CBCs and sign-preserving input to ON-CBC via gap junctions [8]. ON-CBC are connected to cones via an inverting connection from one side and send input to ON-Ganglion cells from the other side. Cone OFF pathways have connection to OFF-CBCs via non inverting connections providing input to OFF-Ganglion cells ON-CBC are connected to cones

via an inverting connection from one side and sends input to ON-Ganglion cells the other side. Cone OFF pathways have connection to OFF-CBCs via non inverting connections providing input to OFF-Ganglion cells [9]. RBCs do not have a direct connection to RGCs and their outputs go to RGCs through AII ACs. The output of AII ACs provides sign-inverting glycinergic input onto OFF-CBCs and sing-preserving input to ON-CBC via gap junctions [9].

1.1.3 Horizontal cells

HCs act as interneurons. They provide either local or long interaction between photoreceptors building up the lateral inhibition structure that facilitates the process of edge detection and image sharpening in the retina. By making feedback networks with themselves and bipolar cells, HCs adjust the gain of photoreceptor synaptic output to BCs. HCs construct the basis of spatial and color opponency by their interaction with PRs, BCs, and other HCs. Two major morphological types of HCs are identified in vertebrate retinas. B-Types that have axons and distinguish changes in brightness and A-type HCs that are axon-less and only connected to cones (also known as H2 and H3 cells). A-Type HCs build up the first elements of color vision processing in the retina [10].

1.1.4 Amacrine Cells

ACs are also interneurons. They are the most diverse cell type in the retina. Most ACs are inhibitory with GABA or glycine neurotransmitters. They make the second synaptic connection level in IPL, and modulate the activity between RGCs and BCs [11]. ACs can act as local inhibition by interacting with BCs and RGCs, acting as both lateral and vertical inhibition between different synaptic layers. They help the retina to perform complex signal processing. For example, AII ACs facilitate interactions between RBC and RGCs and seem to play a role in approach detection. Poly axonal ACs have shown to be sensitive to motion and starburst. ACs are direction-selective [12].

1.1.5 Ganglion cells

RGCs accomplish the last layer of signal processing in the retina. They receive input from BCs and ACs in chemical form and send the processed information in the form of binary spike trains to the brain through the optic nerve. It has been shown that some RGCs are sensitive to a unique combination of visual stimuli. In other words, RGC types are tuned to detect a specific feature of the visual scene. For example, some cells are direction-selective while some can be sensitive to motion or color. The brain interprets the perception of the world by combining and processing the parallel information received from RGCs [13]. In the first electrical recording from RGCs in 1938, three different patterns were reported [14]. Some RGCs were responding only to the onset of light and were named ON cells. Another category of RGCs generated action potential during stimulus offset (darkness) termed as OFF cells. Some RGCs were sensitive either to stimulus

onset and offset known as ON-OFF cells. Later in 1953, the lateral inhibition mechanism was discovered by Kuffler [15]. He observed that RGCs have the highest rate of activity, not necessarily after increasing the intensity of light, but rather by increasing the contrast of light between the center and surrounding of the cell's receptive field. This phenomenon can be observed in ON and OFF cells and is known as lateral inhibition (figure 1.2). By performing more sophisticated experiments in the last few decades, new subtypes of the putative cells were discovered. In a recent study by Baden et al., clustering mouse RGCs, based on their morphology and functions using machine learning techniques, yielded more than 30 different RGC cell types [16] including sustained/transient, color selective, direction/orientation selective, and edge detectors with different level of sensitivity to contrast and spatiotemporal frequency. The input image of the visual scene is processed by this complex network of different cell types and decomposed into plenty of parallel digitized feature vectors and sent to the brain via the optic nerve. In retinal Prostheses, to achieve a proper perception of the visual scene, a precise stimulation strategy that can mimic both temporal and spatial details of retinal coding, plus the ability to stimulate the correct neuronal target, is essential. Since RGCs are the last layer of signal processing in the retina, understanding the coding mechanism in this layer can help us to design a more efficient stimulation strategy for retinal implants.
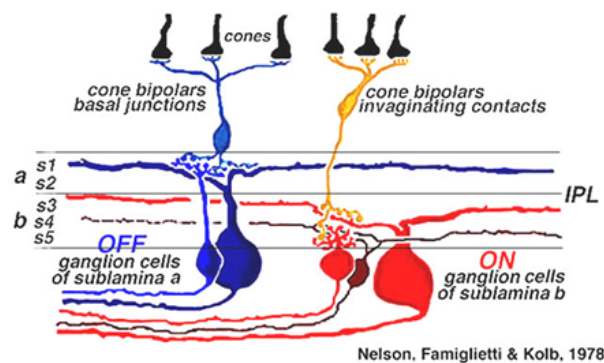
Figure 1.2: Synaptic connections of ON and OFF retinal ganglion cells. Image is taken from http://webvision.med.utah.edu/

1.1.6 Retinal diseases

Age-Related Macular Degeneration (AMD) is a progressive retinal disease caused by damage to the Macula. AMD often happens in elderly people and leads to a lack of vision or blurred vision in the central visual field. Over time this black or blurred spot may get larger. Although currently, no treatment can restore vision for people with AMD it has been reported that dietary supplements may slow down the speed of progress [17]. Retinitis Pigmentosa (RP) is another retinal disease that causes the degeneration of rod photoreceptors. Unlike AMD in RP, loss of vision starts from the periphery, is known as tunnel vision. Night blindness, the problem with

vision under dim light conditions, and difficulty in color vision are some of the symptoms of RP. Currently, there is no therapy that stops the progress of RP [18]. RP and AMD together form about 10% of the causes of blindness [19].

1.2 Therapy approaches to restore vision

Different technologies are developed and tested to treat the degenerated retina. Cell therapy, Gene therapy, and artificial retinal stimulation are among the major approaches to restore vision.

1.2.1 Cell therapy

In this method, ectopic cell transplantation is used to replace damaged cells. Cell therapy uses transplanting stem cells obtained from pluripotent cells to restore the damaged tissue. These cells can be taken from a donor or the patient. The important point about stem cells is the ability to yield different cell types and self-renewal. Cell therapy can be done either by using Pluripotent stem cells or multi potent. To make Pluripotent stem cells two approaches are suggested. One approach uses human embryonic stem cells. The internal cell mass of the embryonic stem cells contains about thirty pluripotent cells with the ability to generate the body's cells. Under proper culturing conditions, these cells can multiply. Depending on the culture conditions they may differentiate different cell types such as muscle cells or neurons. In the other approach, the induced pluripotent stem cells (iPSC) of adults are used to make pluripotent cells using genetic engineering [20].

Multipotent stem cells can be found in the whole body and are able to differentiate in a smaller number of cell types. Muscle fibers, bone cells, and fat cells can be generated by these cells. It has been shown that retinal organoids can generate cell lines useful for cell therapy. Retina cell therapy is more difficult since it requires the migration of transplanted cells to the precise location and exhibits specific physiological activity with true synaptic connection [21].

1.2.2 Gene therapy

Inherited retinal degeneration can be caused by a mutation in 300 different genes [22]. Therefore, finding an approach to tackle this issue is very challenging. Gene therapy in the retina is applied by injecting a vector of adeno-associated viral vectors (AAVs) that contains the gene of interest for the retina. Because primate eyes have a thicker membrane the diffusion of the delivered gene vector is limited and affects the efficacy of the method [21]. An alternative method is to deliver the gene vector via sub-retinal injection. Although this approach may damage the photoreceptors by separating the pigmented epithelium from the rest of the retina, in 2017 FDA approved AAV gene therapy for the treatment of the monogenic disorder [23]. In Another gene therapy approach, the DNA and RNA fragments will enter the cell by applying electrical discharge or laser to the

cell membrane. The method is called Non-viral gene delivery and the target protein has transient expression [21].

Optogenetic therapy is another method that is suitable for the type of retina degeneration in which only the photoreceptors are lost and the remaining layers are maintained intact. In this strategy, the surviving cells become sensitive to light by delivering light-sensitive molecules to the residual neurons that are insensitive to light. Bi et al generated artificial photoreceptors by delivering AAV of channelrhodopsin (ChR2), a transgene that encodes light-sensitive protein to surviving cells of the retina. One of the challenges of this method is that the light intensity required to activate ChR2 is higher than normal light conditions and can be toxic for the retina [22, 24, 25].

1.2.3   Electrical stimulation

Using microelectrode arrays to electrically stimulate retinal surviving neurons to restore vision has been extensively tested by many teams around the world. Clinical studies showed promising results in restoring vision by placing an array of electrodes on the retina surface with different configurations [26]. In the following sections, we will assess the principles of electrical nerve stimulation and its application in retina implants.

1.3   History and applications of electrical nerve stimulation to vision

In 1775 LeRoy induced the sensation of light by applying electrical stimulation on the scalp of the blind [27]. One of the earliest nerve electrical stimulation studies was carried out in 1780 by Galvani. He observed muscle contraction by applying electrical charge into the nervous system of the frog [28]. More than 100 years later in the late 19th century, other scientists showed the connection between limb movement of dogs and humans through stimulation of their motor cortex [29, 30]. After the development of stereotaxic techniques in the early 20th century scientists successfully performed localized deep brain stimulation of the human brain. Gradually electrical nerve stimulation became a useful approach to help people with neurological related disorders. Cochlear implants, pacemakers, transcutaneous electrical nerve stimulation (TENS), deep brain stimulation, and recently retinal implants, are among the successful applications of nervous system related rehabilitation strategies [28]. In the second half of the 20th century, the first successful attempts to use a device to generate the perception of light via stimulation of the visual cortex and retina were reported [27, 31, 32]. Since retinal stimulation elicits a more natural perceptual neural code by activating the neural circuits between the retina and the brain, it may have a better perceptual performance compared to cortical stimulation. In the mid-1990s a new generation of retinal prosthetics for human subjects was developed by locating an array of small

electrodes on the surface of the retina. Blind subjects reported a perception of light corresponding to the location and time of stimulation [27, 33] (figure 1.3).
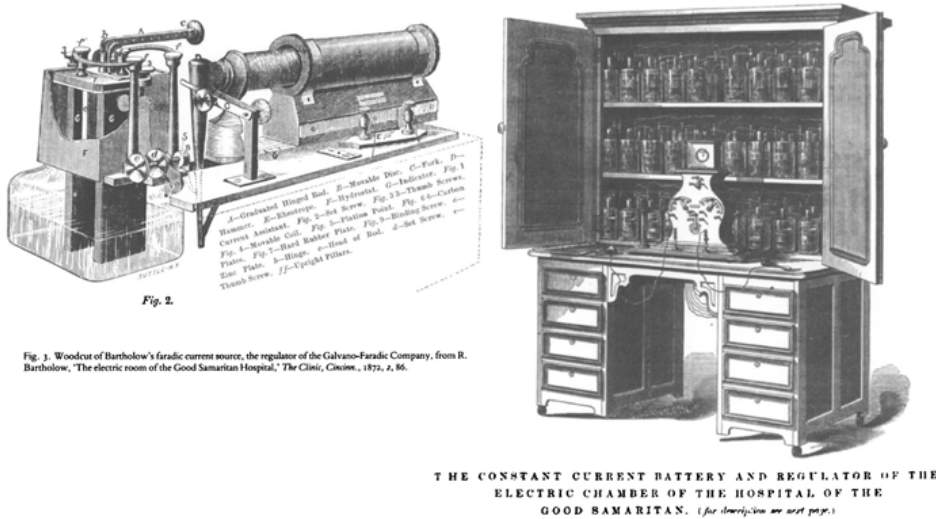
Figure 1.3: One of the early electrical stimulators designed to apply electrical current to the human brain, used in 1872 at Good Samaritan Hospital. Figure adapted from Morgan 1982.

1.4 Principle of electrical nerve stimulation

Electrical stimulation of nerves can be performed either intracellularly or extracellularly. Extracellular stimulation is employed for the application of retinal prosthetics. In this method the electrical current applied through an electrode placed into tissue will generate an electrical field. This electrical field affects the charge density around cells and can lead to the generation of an Action Potential (AP). The higher amount of electrical current generates a stronger electrical field that increases the probability of AP generation [34]. Electrical stimulation can be done either by cathodic or anodic pulses. In cathodic stimulation, the outer layer of the cell membrane that is closer to the electrode receives a negative charge and gets depolarized, on more distant parts of the membrane a weak hyperpolarization might occur. Anodic stimulation on the other hand is less efficient because of the hyperpolarization of the membrane in the vicinity of the electrode [27].

1.5 Retinal prostheses

For the first time in 1956, it was reported that electrical stimulation of Ganglion Cells in the retina generates bright spots known as phosphenes[32]. Generation of the action potential by RGCs can be performed directly, via soma and axon, or indirectly by activation of Bipolar Cells (BC) through

synaptic connection to the Ganglion Cell layer. In a direct stimulation, depending on the location of the electrode, cells can be stimulated via axons or soma [35, 36](figure1.4). Some cells have larger axons passing around the proximity of other cell's somas. In such cases, activation of cells through their axons is challenging, since it can lead to concurrent activation of either the adjacent cells and/or cells located in more distant locations. In retinal implants, an array of electrodes is placed in proximity to the retina. Axonal stimulation in such arrangements generates an elongated percept of phosphenes. This is one of the practical challenges in reconstructing the true perception of the real-world image by extracellular microelectrode array stimulation.

Success in the development of cochlear implants in addition to advancement in electronics and fabrication of microelectrode arrays, encouraged researchers to develop chronically implantable prostheses for the retinas of blind people with the aim of restoring vision. RP and AMD diseases lead to degeneration of photoreceptors [18]. However, the rest of the retina in some cases remains intact. It has been shown in such cases applying current into the tissue through an array of electrodes can elicit phosphenes. Depending on the site of electrodes on the retina, two main configurations are suggested and tested for multielectrode stimulation. In one configuration electrodes are surfaced on the Ganglion cell layer, known as the epiretinal approach [27, 33, 37]. In another approach, electrodes are located between the retina and the retinal pigment epithelium known as subretinal configuration [26, 38]. Results of an epiretinal implant with a 16 channel electrode array were released in 2003 [39]. In 2011 results of a subretinal implant with 1500 electrodes showed the possibility of distinguishing objects and letters by blind patients [26].
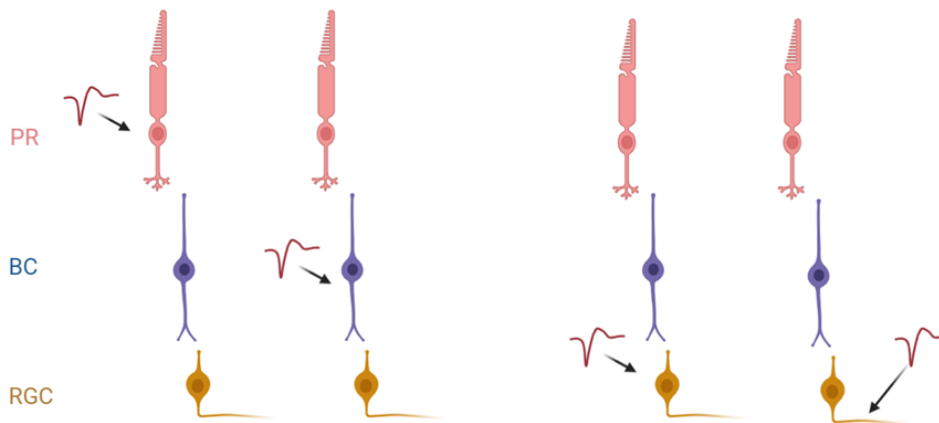
Figure 1.4: Schematic of direct and indirect stimulation. Left, indirect activation of RGC through activation of BC (purple) or PR (red). Right shows direct stimulation of a RGC via soma and axon. Figure is modified from Yue et al. 2016.

1.5.1 Subretinal

In this configuration metallic electrodes are positioned on a degenerated photoreceptor layer and interact with BCs (figure1.5). Indirect stimulation of GCs via BCs is possible in this configuration.

Furthermore, an array of photodiodes can be implanted to transform light into electrical current. With this arrangement an external camera is not required, giving the advantage of receiving natural scenes by eye movement instead of head movement [3]. Tübingen's Alpha IMS is an example of a subretinal implant. This implant employs 1500 microelectrodes for stimulation plus photodiodes for converting light to electrical signals. The visual acuity reported by this implant is 20/546 which enables some patients to identify objects as small as kitchen cutlery or distinguish large letters of the alphabet [38].
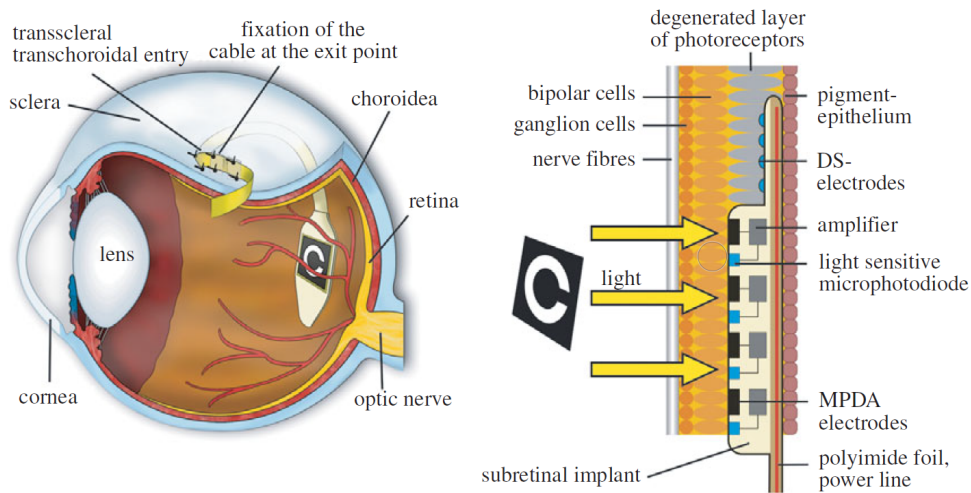
Figure 1.5: Subretinal configuration. Image is taken from Zrenner et al 2011

1.5.2 Epiretinal

Electrodes in this configuration interface with RGCs in the inner limiting membrane of the retina [35]. This approach can be applied to the late-stage degenerated retina. Depending on the pulse duration and polarity, BC and RGCs have been shown to be stimulated separately [3, 35]. Arguss II is an example of an FDA approved epiretinal implant with 60 electrodes that enabled motion detection and alphabet discrimination in some patients[40] (figure1.6). This device has an external camera and a signal processing unit to perform the task usually done by the retinal network.

1.6 Retinal stimulation strategies

Traditionally a cathodic charge-balanced pulsatile waveform is used for neural stimulation in retinal implants[33]. Cathodic pulses depolarize the RGCs membrane and lead to the generation of action potentials (figure1.7). Adding a positive pulse after the negative phase makes the stimulus charge-balanced and avoids electrode corrosion during long-term stimulation[33]. Several studies
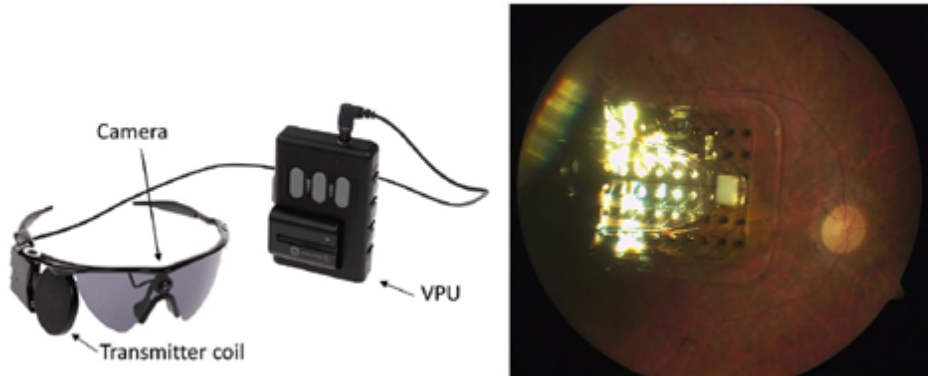
Figure 1.6: Arguss II with epiretinal configuration. Image from Hornig et al. 2007.

have been carried out by changing the stimulation parameters such as phase, pulse duration, and frequency to find optimum parameters of stimulation [41–43].

1.6.1 Selective stimulation

It has been reported that when increasing the number of electrodes above a specific number, changes in the quality of restored vision will only increase slightly, however, retinal prostheses with larger numbers of dense electrodes do not significantly improve the ability to recognize objects. This suggests that further improvement in restoring high acuity vision requires more investigation into retinal neural coding and stimulation strategies such as preferential stimulation of distinct cell types rather than merely increasing the electrode numbers.

Preferential activation can be done by targeting specific retinal cell classes i.e. BC, PR, AC, RGC or subtypes of a certain class, for example RGCs. For both forms of stimulation, different techniques are suggested. For example, probing the stimulation parameters to find the preferred stimulus of distinct neuronal targets, or using alternative energy delivery strategies such as magnetic stimulation, by replacing conventional electrodes with micro coils[44]. Stimulation of soma without activation of distal axons, to avoid elongated bright spot perception is another form of the selective activation, and is one of the unsolved challenges of current retinal implants [45]. Tsai, David, et al. assessed the effect of pulse width to preferentially recruit neuronal targets in the retina. They observed that some cell classes respond more strongly than others in response to pulse stimulus with a specific duration [46]. In addition to magnitude and phase, some studies investigated other parameters such as waveform shape and stimulation frequency [4, 46, 47]. Freeman et al. applied sinusoidal waveforms with different frequencies on the rabbit retina to reach a level of control over the target neuronal network [47]. They used sinusoidal waveforms with a wide range of various frequencies from 5 up to 100 Hz. They observed that low-frequency stimulation (10 Hz) elicits spikes when the electrode is located near the soma and elicits no spike when the electrode is in the proximity of the axon, while the high frequency stimulation (100 Hz)

elicits a response if the electrode is positioned either close to the soma or axon. This is an example of the advantage of alternative stimulus strategies over classical pulsatile stimulation. Boinagrov et al. investigated the effect of pulse duration and polarity for direct and indirect stimulation. They observed that cathodic stimulation has a lower threshold for direct activation of RGCs, whereas for network mediated stimulation, the threshold of anodic stimulation is smaller and network selectivity is higher with longer pulses.
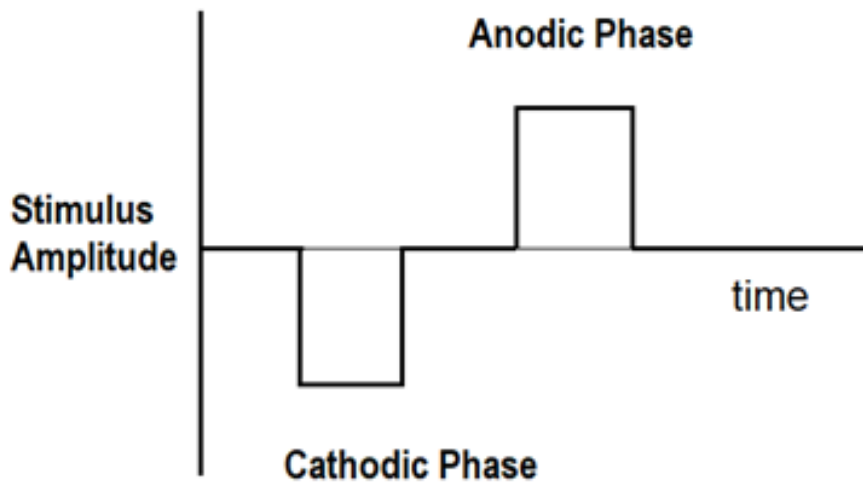
Figure 1.7: Charge balanced pulsatile stimulus waveform. Image modified from Humayun et al. 1998.

Apart from preferential activation of cell classes, some studies assessed the possibility of preferential activation of different RGCs types, which is the main focus of our study. Likewise, different stimulus parameters were tested to find the preferred stimulus of distinct cell types. Heterogeneous expression of ion channels across different cell classes, in addition to activation/inactivation kinetics of each channel type, raised the question of whether stimulation frequency can be used as a parameter for selective activation. Freeman et al showed that positive and negative peaks of a 5 Hz sinusoidal stimulus can elicit different spiking patterns in ON and OFF cells [47]. Gue et al. showed the efficacy of high frequency stimulation on preferential activation of ON and OFF cells [48]. Twyford et al. tested sinusoidal waveform at different frequency ranges and showed that ON sustained RGC have a weaker response at lower frequencies [49]. They also showed that ON and OFF cells have different response patterns using a 2000 pulses per second stimulus modulated with a diamond shaped envelope [50]. Im et al. assessed the effect of stimulus duration on selective activation of RGCs. They reported that increasing the duration of stimulus will decrease the spike rate of ON cells[51]. In another effort to find the preferred stimulus of different RGC types, some groups applied electrical white noise to

the retina. By taking the advantage of the spike triggered averaging (STA) method they were able to estimate the linear electrical input filters for different RGCs [5, 52–54]. These results exhibited the diversity of electrical input filters across different cell types. Sekhar et al. reported that electrical profiles of two major ON and OFF RGC types are different and correspond to their visual input fillers [4].

1.7 Aim of this study

Although many parameters are involved in developing retinal prostheses with a higher level of performance the ability to selectively target neural pathways in the retina seems to be one of the important factors that is not very well addressed in designing current retina implants.

Several research groups around the world have been working on preferential stimulation of neural pathways. Different stimulation strategies such as using electrical stimuli with different frequencies or amplitude have been suggested. Despite their relative successes, none of them were completely successful in reaching this goal. Gaussian noise has been tested by some researchers to explore the potential stimuli subspace by estimating the electrical input filters of different RGC types [4, 52–55]. In this thesis, we aim to continue the past works of Sekhar et al. [4] who used the STA technique to characterize the electrical input filter of ON and OFF RGCs by applying electrical noise stimulus. Our goal is to shed more light on this matter by providing a catalog of electrical profiles for a wider range of RGCs. It has been shown that in mouse retina over 30 different subtypes of RGCs exist [16]. To our knowledge, no exhaustive research has been performed so far to elaborate the property of their electrical input filters in order to design electrical stimuli.

CLASSIFYING RGCS WITH PSEUDOCALCIUM TRACES

2.1 Introduction

Having information about the electrophysiological features of the neuronal targets in the retina is an essential part 0f obtaining proper electrical stimulation for the retinal implant. In retinal stimulation, RGCs are recognized as the main neuronal target involved in the visual processing network to achieve artificial vision. Several studies have been carried out to reveal the physiological features of RGCs in different species. Although there is a disparity in neural circuits of different species, the basic structure of the visual system is similar in most mammals. Therefore, investigating the visual system of animals such as mice can enhance our understanding of the retinal organization and may help us for developing the newer generation of retinal prostheses.

RGCs can be classified either functionally and morphologically [56]. In the earlier stage of visual neuroscience studies ganglion cells were usually classified subjectively into ON, OFF and ON-OFF according to their response to flash light stimulation. Each cell type could be categorised as a transient or sustained cell based on their response patterns[57]. In 2003, Carcieri et al. suggested a quantified clustering algorithm based on response properties such as latency, duration, and amplitude of mouse RGCs responses [58]. By classifying cells using putative features, they reported five different ganglion cell classes. In 2006 Segev et al. divided salamander ganglion cells into six functional classes. They showed that six broad cell types can be recognized by using the information revealed by the temporal dynamics of their receptive field [59]. Two years later Zeck et al. clustered rabbit RGCs into nine different clusters based on the information coded in inter-spike interval timing [60]. In 2010 by using Multi-Electrode Arrays (MEA) recordings, Farrow et al. classified mouse RGCs into 12 functional types based merely on a

physiological basis [61]. Advancements in machine learning and cell imaging techniques allowed researchers to perform more elaborated classifications that lead to the detection of new cell types. In 2016 Baden et al., by recruiting both anatomical and physiological features, reported more than 30 different ganglion cell types in mouse retina [16].

Although these studies give us a deeper insight into retinal circuits' structures, we should notice that most of the studies aim to characterize RGCs through visual stimulation. For the development of retinal prostheses, in addition to visual-induced activities, we need to be able to predict the retinal circuit's behavior to electrical stimulation. To this end in our experimental design, we applied both visual and electrical stimuli. Since the study carried out by Baden et al. was the most comprehensive work on the functional classification of mouse retinal ganglion cells when this project began, we used their result as a reference for our clustering. By applying unsupervised clustering on 2-photon calcium imaging data of about 11000 cells and using anatomical criteria, Baden et al. showed that the mouse retina has more than 30 different functional outputs. They presented four visual stimuli including a full-field chirp to assess the temporal frequencies and contrast preference, a moving bar stimulus to examine the degree of direction selectivity, a binary noise to extract cell's receptive field, and a blue/green full-field stimulus to characterize chromatic sensitivity of RGCs. They also used immunohistochemistry to detect displaced Amacrine Cells (dACs) as well as RGCs. In addition to that for a few RGCs, they performed a simultaneous recording of Ca^{2+} and spike activity to estimate the kernel that transforms spike data into calcium traces. For clustering RGCs, at first, they performed unsupervised clustering and used sparse principal component analysis (sPCA) to extract light-induced features. Direction-Selective (DS) and non-direction-selective cells were first separated and then clustered independently. Afterward, for clustering cells into different groups, they collected all extracted features and applied a mixture of Gaussian models to them. In addition to functional clustering, they performed post clustering to identify dACs and alpha RGCs with large soma. Finally, their method clustered cells into 46 groups. Including 32 RGC types and 14 dACs groups [16].

In this chapter, the main goal is to classify each RGC into one of the 49 RGC clusters defined by Baden et al. and afterward, assess cell activity in response to white noise electrical stimulation. Baden et al. performed a calcium imaging technique to record the neural activity of the retina. We used a similar set of visual stimulation, however, since our recording was performed with the microelectrode array, to match our data with their recordings we needed to transform electrophysiological signals into pseudocalcium traces before performing clustering. The following chapter describes in detail the method used for converting spiking data into pseudocalcium traces. For electrical stimulation, we used a white Gaussian noise that gives us the privilege of estimating electrical input filters of stimulated RGCs using the STA method. This offers us the opportunity to assess the electrical preference of the classified cells. Clustering was performed based on visual induced activity. To this end, after estimating pseudocalcium traces from spiking

activity we assigned each cell to one of the defined clusters of the Baden et al. based on their response similarities (see figure 2.1).
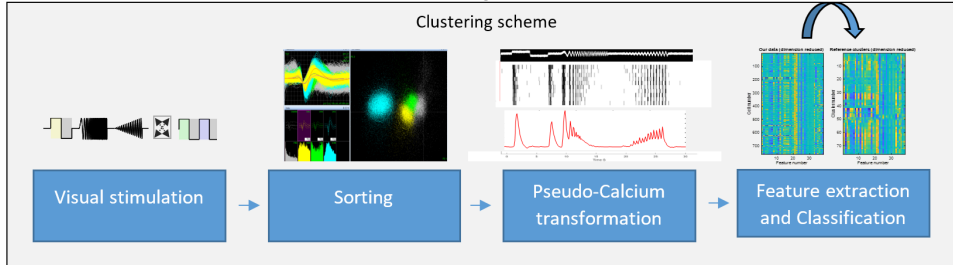
Figure 2.1: Schematic of the proposed workflow for clustering RGCs.

2.2 Materials and Methods

2.2.1 Retinal preparation

C57BL/6 mice were housed under standard white cyclic lighting and had free access to food and water. All procedures were done in accordance with the ARVO statement for the use of animals in ophthalmic and visual research; and experiments were approved by the Tübingen University committee on animal protection (Einrichtung für Tierschutz, Tierärztlicher Dienst und Labortierkunde). Animals were anesthetized with isoflurane and killed after cervical dislocation. After making a mark on the cornea with a heat pen, eyes are pulled out carefully and kept in carbogenated (95% O2, 5% CO2) Artificial Cerebrospinal Fluid (ACSF) solution [42]. Heat marks on the cornea allowed us to hold down the scissor's tip and cut it and pull out the lens. This detaches the retina from RPE and makes it ready for recording. The optic nerve is then cut and before placing the retina on MEA (Multichannel Systems; Reutlingen, Germany) the invisible layer of Vitreous humor is removed and the retina is cut into two parts. The retina is then laid on the MEA with their ganglion cell layer facing electrode tips. A teflon chamber covered with a dialysis membrane is put on the retina to keep it fixed on the MEA. Appropriate conditions in terms of pH level, oxygenation, temperature, and nutritional requirements were ensured via a pump continuously perfusing the tissue with artificial cerebrospinal fluid. The dialysis membrane on the teflon ring is penetrable and allowed the retina to receive fresh ACSF solution conditions to keep them alive and responsive as long as possible [62].

2.2.2 Visual stimulation

For light stimulation, we focused a developer module projector (DLP® LightCrafter 4500, Texas Instruments) through a custom light path of lens, mirror, and condenser onto the MEA. Stimulator intensity (as photoisomerization rate, 10^3 P*/s/cone) was calibrated to match the previous Baden

et al. 2016 study as closely as possible with the white stimulus set close to 3×10^4 P*/s/cone photoisomerization rage for mouse UV- and M-cones and the black stimulus set close to 10^4 P*/s/cone. A steady mean illumination 2×10^4 P*/s/cone was present during the electrical stimuli and remaining recording period to maintain the adaptation state. For all experiments, the tissue was kept at a constant intensity level for at least 30 s before light stimuli were presented.

Visual stimuli including chirp, moving bar color, and noise, were adapted from Baden et al [16]. The chirp stimulus consists of two sinusoidal modulations, one with increasing frequency and one with increasing contrast; drifting bars with horizontal bars at 15 locations, vertical bars at 10 locations, and diagonal bars at 17 locations for each diagonal axis, bar size was 1000 x 300 µm with the centers of adjacent bars separated by 200 µm; full-field color flashes for 3 sec each in a sequence of blue, black, green, black. In addition to Baden et al. stimuli, a full-field flash stimulus with 2 seconds light on followed by a 2 sec light off period is used for all experiments. Each block of flash stimulation includes 20 repetitions (figure 2.2).

2.2.3 Electrical stimulation

After visual stimulation, one electrode from the site of the MEA with maximum activity was chosen for electrical stimulation. An STG4000 Series (MCS, Reutlingen, Germany) stimulus generator was used for electrical stimulation. Electrical signals are applied from the ganglion side of the retina through one of the 59 MEA electrodes.

Electrical stimulus was adapted from the previous work of Sekhar et al [5]. The amplitude was drawn from white Gaussian noise with a mean of -800 mV, SD of 35% (280 mV), with 100-second duration. 1 ms monophasic cathodic rectangular voltage pulses with 39 ms intervals that give a stimulation rate of 25 Hz were used for stimulation. By setting the amplitude of most pulses subthreshold, we were able to examine the integrative filters of the network. We used the 10 msec lockout after each pulse to eliminate direct responses such that only indirect responses remained.. Using this stimulus Sekar et al. were able to extract the electrical STA of different RGC types [4, 55]. The number of trial repetitions varies between 15 to 36 for different experiments (figure 2.2).

2.2.4 Recording System

The extracellular activity of cells recorded by Multi-Channel Systems 60 standard MEA with 30 µm electrode tips diameter and 200 µm spacing. The sampling rate was set at 50 kHz and signal amplification was performed with a Multichannel system amplifier in two phases with a total gain of 1100. Data are monitored and stored on the PC equipped with MC-Card data acquisition hardware and MC-Rack software (figure 2.2).
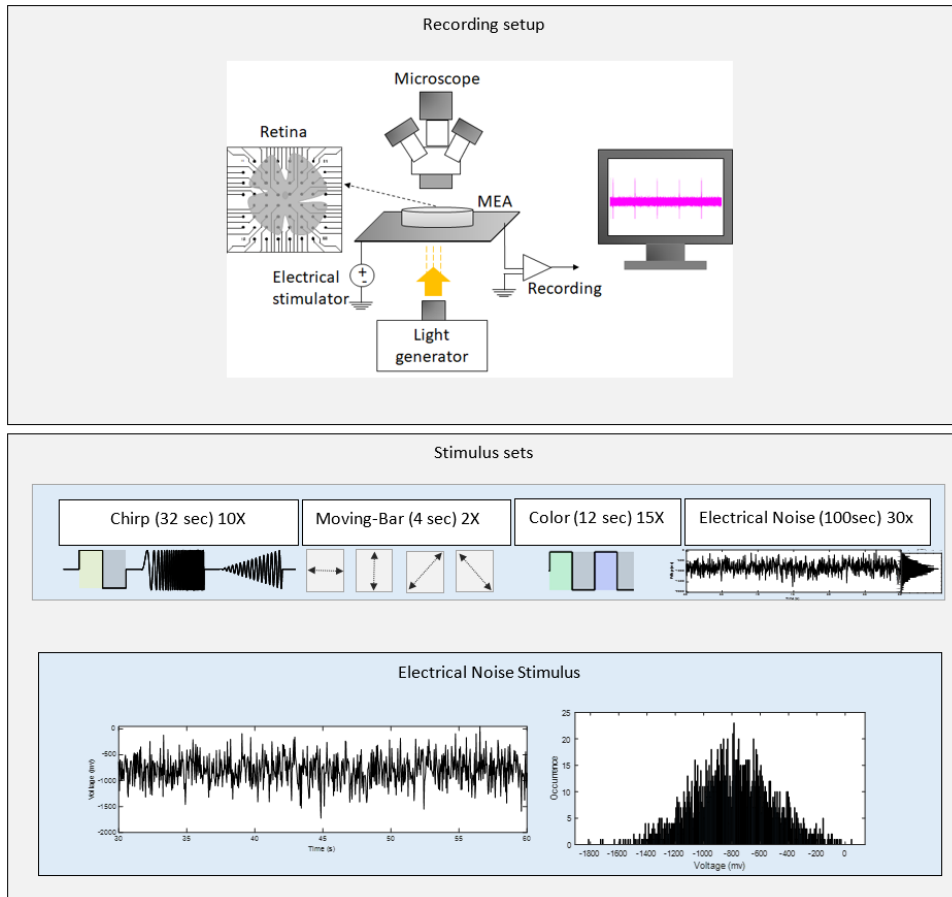
Figure 2.2: Recording setup and visual and electrical stimuli with number of repetitions for each stimulus. Top: experimental setup for recording extracellular activity of retina (figure from Hosseinzadeh lab, Leipzig). Bottom: Visual stimuli derived from Baden et al. including Chirp (10 rep), Moving-Bar (2 rep) and Color (15 rep). Electrical stimulus is a white Gaussian noise drawn from Sekhar et al (30 rep).

2.2.5 Data pre-processing and unit selection

Pre-processing includes three steps: filtering, spike detection, and spike sorting using Offline Sorter (Plexon Inc., TX, USA). After high pass filtering raw data through a second-order 300Hz Bessel filter, sharp negative deflections, whose standard deviations from the mean were beyond -5, were considered as events (Action Potentials). These events clustered later into different units using T-distribution Expectation-Maximization(TEM). Ultimately, sorted clusters were visually inspected and manually resorted if necessary. During the inspection step, criteria such as spike waveform and inter-spike interval histograms were used to remove low-quality clusters or to merge similar clusters.

2.2.6 Spike Triggered averaging

In the early stage of visual electrophysiology studies, visual stimuli such as moving bar or gratings were widely used for probing response features of the stimulated neurons. However, constraints such as adaptation and the limited stimulus manifold, resulted in inferior estimation of the receptive field. Therefore white Gaussian noise was suggested as an alternative stimulus[55]. Although white Gaussian noise is a common tool to estimate the parameters of the unknown system in the field of linear system identification, the applicability of this method in neural systems has been a matter of debate because of the nonlinear properties such as saturation and spike threshold. In 2001 Chichilinsky et al. implemented a method of white noise analysis applicable to neural systems despite their nonlinearities [63]. This approach assumes that spikes generated by a neuron originate from a generator signal that is shaped by the linear combination of its temporal and spatial visual inputs. In this approach the expected response 'R' of a neural system to the stimulus can be stated as the average number of spikes 'f' in a time bin after stimulation:

$$R(s) = <f|s> = \sum_f f P(f|s)$$

$\sum_f$ represents the average over different repetitions. In other words the relation between stimulus and response can be written as $R(s)$, the linear combination of stimulus 's' with corresponding weights 'w' that represents the neuron's selectivity to a given stimulus:

$$R(s) = N(w.s)$$

The inner product of each 'w' vector with 's' makes its generator signal. $N(.)$ is the nonlinear function and adds the nonlinearity part of the neuron to this architecture. To find the stimulus-response relationship R(s), Chchilinsky et al. suggested using the well-known method STA that is the average of stimuli preceding all spikes.

$$f(x) = \frac{\sum_{t=1}^{T} s_t f_t}{\sum_{t=1}^{T} f_t}$$

For large recording time, one can rewrite it as:

$$a = \frac{<sf>}{<f>} = \frac{1}{<f>} \sum_s \sum_f sf P(s\&f) = \frac{1}{<f>} \sum_s \sum_f sf P(s)p(f|s) = \frac{1}{<f>} \sum_s sP(s) \sum_f f P(f|s)$$

$$= \frac{1}{<f>} \sum_s sP(s)R(s)$$

Therefore, one can show that 'a' is proportional to 'w', which means STA can explain the linear part of the model [63].

2.2.7 Estimating calcium traces from spiking data

After processing data, we have the binary vectors of spike times. Since the classification of our reference paper is performed by calcium traces we need to estimate the Ca^{2+} from spiking activity before clustering. This is done by convolving spiking activity of the cells with a time kernel estimated from simultaneous recording of Ca^{2+} and spiking binary data [16]. This kernel is drawn from the Baden et al. study. They computed it by averaging over Ca^{2+} events triggered by spikes for six cells [16]. The kernel then was up-sampled to match with the 50khz sampling rate. Convolution of this kernel with binary spiking data will give pseudocalcium traces that can be used for clustering (figure 2.3).
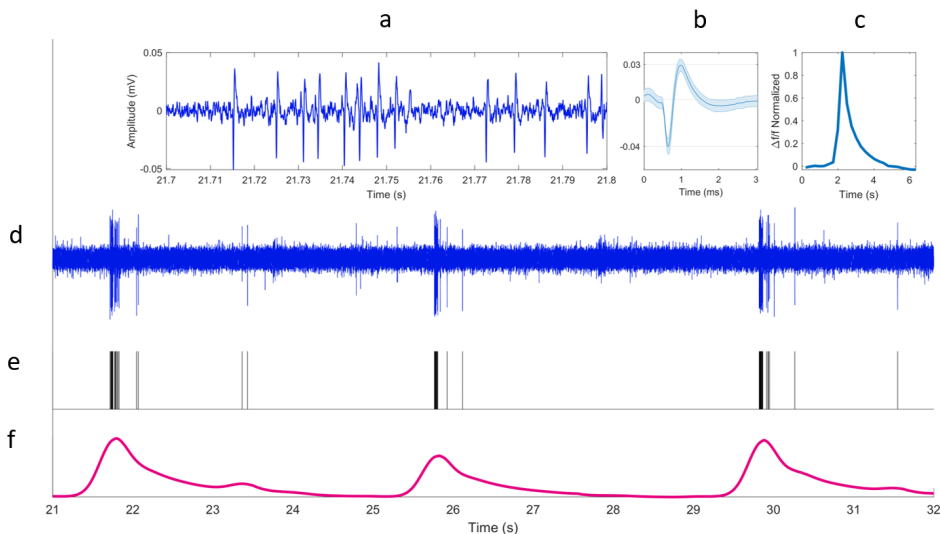
Figure 2.3: Sample raw data and equivalent Pseudo-calcium trace. (a) 100 ms of filtered voltage recording excerpted from d. (b) Average of extracellular action potentials (mean+/-SD). Dashed lines highlight baseline and peak. (c) OGB kernel. (d) 11 s sample of filtered data from an ON cell in response to the cycling flash stimulus. (e) Rastergram of spike times for this cell (note excluded spikes around 25 s assigned to a different cell). (f) Pseudocalcium trace produced by convolving the rastergram e with the OGB kernel c.

2.3 Results

2.3.1 Removing noisy units

In the first step of analysis, the electrical activity of 892 mouse RGC from 9 retinas were used for this study. Since many recorded RGCs do not reflect sufficiently strong stimulus-driven activity we removed them before clustering data. This was done by dividing the average of response variances across trials over the overall variance of responses. The variance was calculated for 100ms time binned Poststimulus Time Histograms (PSTHs) of the chirp dataset across 10 trials.

Then the overall variance of the flattened data of all 10 trials was calculated and divided by the average of variances of each trial. We expected a response variance smaller than the overall variance for stimulus-driven data and excluded the cells with a variance ratio less than one from analysis, leaving 653 RGCs for classification (figure 2.4).

2.3.2 The estimation of pseudocalcium traces

The spike train data then were convolved with the time kernel to estimate pseudocalcium traces of all units (figure 2.3). The estimated pseudocalcium traces were normalized similar to Baden et al. and for each cell, the median of recorded trials was used for clustering. Baden et al used sPCA as a feature extraction method. By using the sPCA we projected the data onto the feature set provided by Baden et al. For most of the cells, we were not able to estimate the linear kernels of visual noise stimulation. Therefore, since the recorded data from noise stimuli did not have proper quality they were excluded from the analysis. For other stimuli, the dimension of the feature set was similar to Baden et al. Which includes 20 features from Chirp, 6 from color, 8 features from the Moving bar, and 4 features from its derivatives [16]. This yields a 38-dimension feature space for classifying.
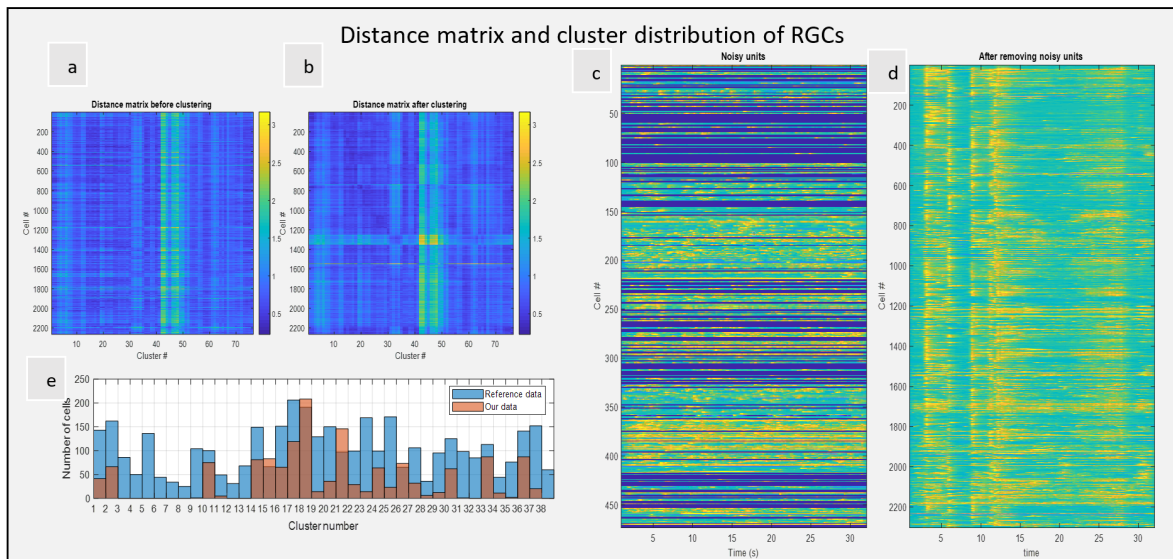
Figure 2.4: Distance matrix of data and pseudocalcium traces of chirp stimulus. (a,b) distance matrix before and after clustering. (c) Pseudocalcium traces of chirp data excluded from analysis. (d) Pseudocalcium traces of chirp data after removing data in c. (e) comparing cell numbers per cluster for our data versus reference data.

2.3.3 Assigning pseudo-calcium clusters to the calcium clusters

In order to assign cells to one of the 75 clusters of the reference dataset, we computed the Euclidean distance between the projected data of our recordings and reference data. Each cell

was assigned to the cluster with maximum similarity. We also performed clustering by computing the distance matrix of the calcium traces of two datasets, but the clustering results were quite similar (results are not shown). After initial clustering, we realized that the time kernel that we used produced pseudocalcium traces and was more transient than real calcium traces and many clusters that represent the cells with sustained activity were not detected. Therefore, we doubled the duration of the time kernel and performed the clustering again. The results of clustering are shown in figure 2.5. This plot shows the first 49 clusters corresponding to 32 RGC groups defined by Baden et al. The method was able to detect 26 of 39 'certain' RGC clusters (70%). We also observed 2 of 10 'uncertain' RGC clusters defined by Baden et al. (clusterss 40-49), thus, 57% of the RGC clusters were matched. However, most of the clusters that correspond to OFF sustained cells (group 4 and 5) failed to match our data. One of the missed categories is alpha cells. These cells were re-clustered based on their soma size in the Baden study [16]. At the end, we assigned the clusters into groups according to Baden's definition. The algorithm could detect 23 of 32 defined RGC types (72%) (figure 2.5, middle column). The clusters containing dACS (50-57) and noisy data (76) are not shown.

2.3.4   The impact of sample size in clustering quality

In order to test the effect of sample size in clustering quality, we also performed analysis on a larger dataset including 2303 stimulus-driven cells recorded from 29 retinas (figure 2.5, right column). Despite a drastic increase of cell numbers, the number of detected clusters increased slightly. Compared to the smaller dataset only five more clusters (9,39, and 43-45) of certain RGCs were detected. All of these clusters were generated from the activity of a very small faction of RGCs(<1%). This shows that the shortcoming in the detection of some clusters is not caused by the lack of enough data, rather the intrinsic limitation of the proposed classification method.
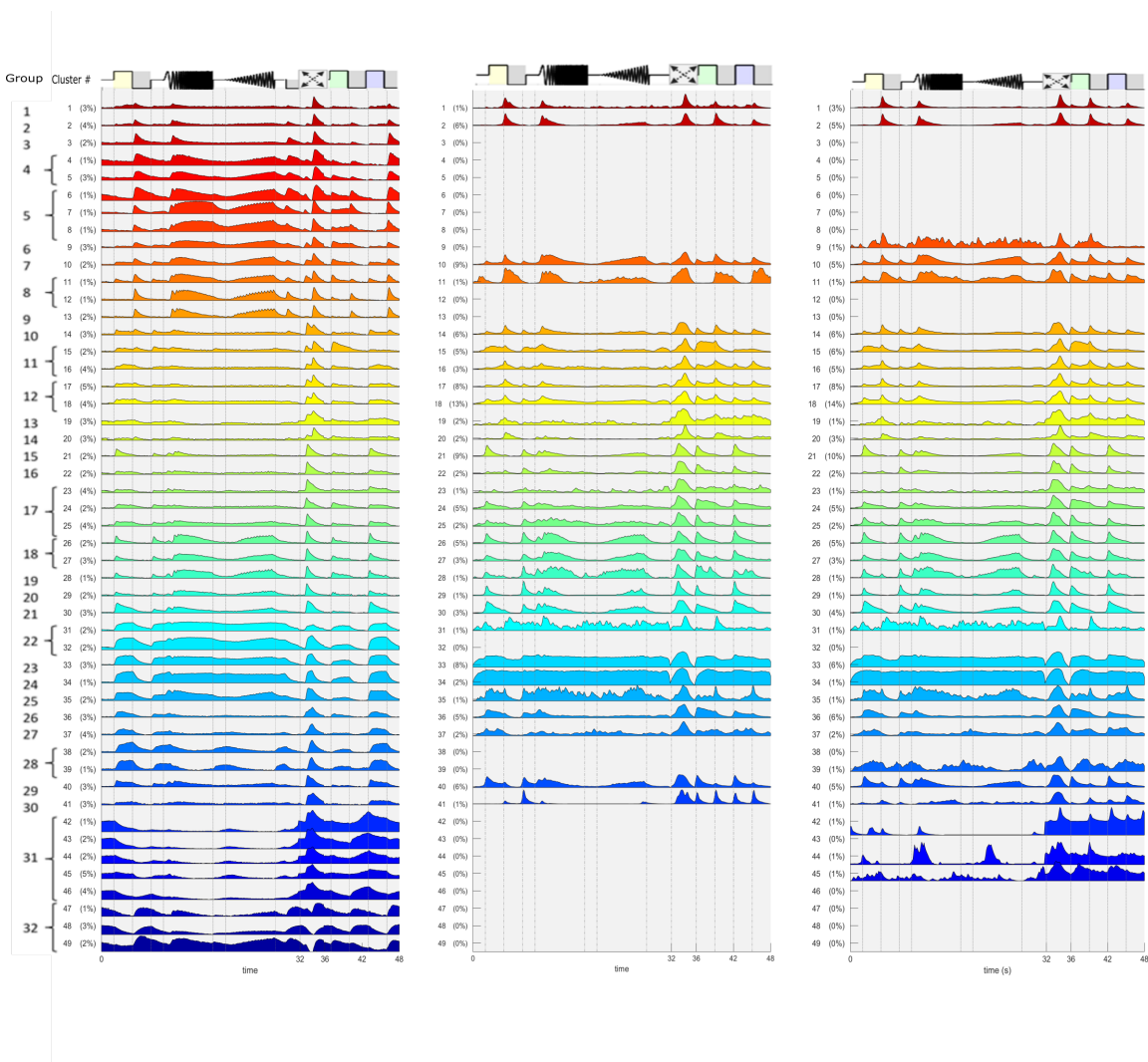
Figure 2.5: Clustered RGCs. Left; reference data, middle; dataset with 653 cells, right; dataset with 2303 cells. Most of the OFF sustained cells were not detected (clusters 3-8). Increasing data samples from 653 to 2303 cells did not change the clustering results significantly.

2.3.5 Electrical input filters

As was mentioned earlier, in addition to light stimulation we used white Gaussian noise to electrically stimulate the retina via epiretinal configuration. This allows us to estimate the electrical input filter of each cell using the STA method. To assess network mediated activity the direct responses were removed by excluding the first 10ms of data after stimulus onset and then the STAs were computed. Figure 2.6 shows the visual and electrical properties of a sample OFF cell. The electrical STA of this cell has a downward peak before time zero. This cell is assigned to cluster 10 (type 7) of Baden's defined clusters which corresponds to the *OFF transient*. The

vertical lines in the spike rates (C) and (G) show high reliability of the response to both electrical and visual stimulation. Figure 2.7 shows the activity of a cell with positive STA. This cell is assigned to cluster 28 (type 19) which corresponds to *ON transient large* cell.
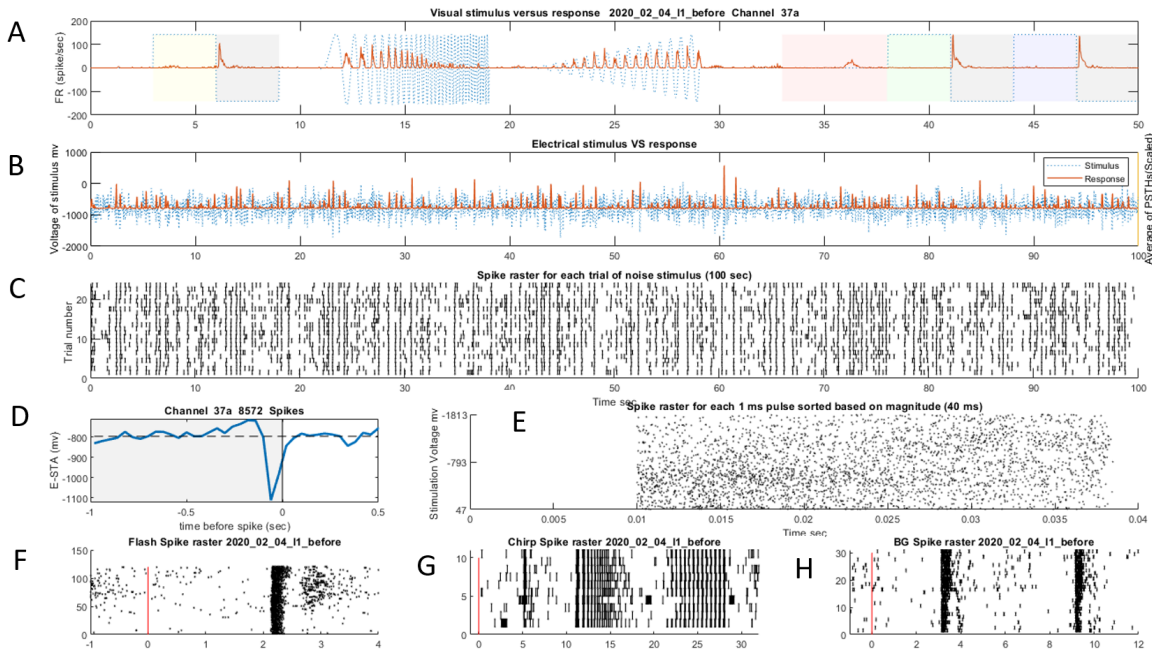
Figure 2.6: Electrical STA of a sample OFF RGC. (A). PSTH of the light-evoked activity of the cell classified as type 7 OFF transient. (Order of visual stimuli is as figure 2.5). (B) Scaled average over PSTHs of 30 repetitions of electrical noise stimulus (notice that y axes show stimulus and response amplitudes). (C) Spike raster of 25 repetitions of electrical noise stimulus, each 100 second duration. (D) Electrical STA shows a negative peak before time zero. (E) Spike raster of electrical noise stimulation for each individual stimulation (sorted based on the amplitude of stimulus voltage). First 10 ms of data was removed to exclude direct spikes in estimation of STA. (F-H) Spike raster of flash, chirp, and color stimulus respectively.

2.3.6 Clustering electrical STAs of RGCs

Since for each experiment, only 1 of 59 electrodes was used for stimulation, mostly the channels in close proximity of the stimulation electrode show a meaningful STA. Therefore, to find the electrical input filter of each cluster we applied the clustering only on the units with significant electrical STAs. The criteria to test the significance of STAs was drawn from Sekhar et al. study [5]. In this approach, the positive and negative peaks of each STA are computed and their significance is tested against the hypothesis that they come from a distribution with similar mean and variance of the baseline signal using a z-test method (alpha=.001). Cells without significant STA were excluded from analysis, leaving 792 units for final clustering (figure 2.8). After clustering data based on the light-evoked activity of the cells, the average of STAs was
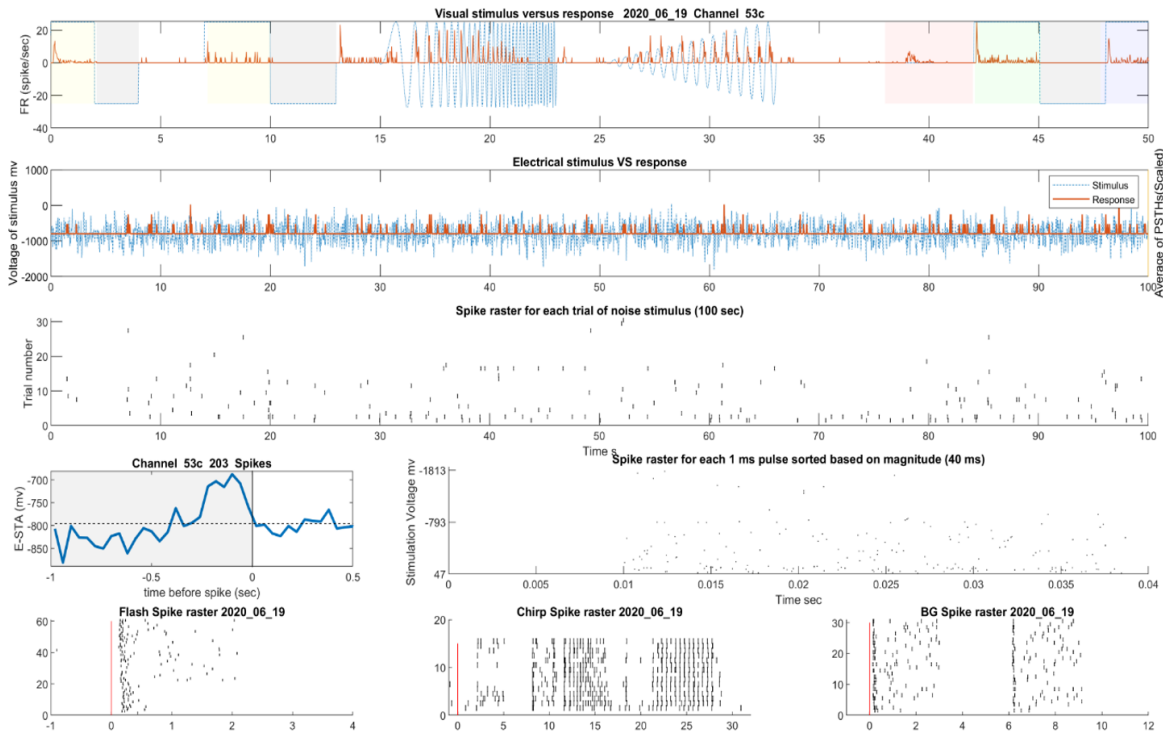
Figure 2.7: Electrical STA of a sample ON RGC classified as type19 (ON trans, large). Legends are as figure 2.6.

computed for each cluster and the significance test was performed in a similar way for positive and negative peaks. The results are shown in the right column of figure 2.9.

Clusters 2, 10, 11, 14, 16 , 17, 18, 23 and 37 reflect electrical STAs with negative peaks. In Baden et al.'s definition, these clusters respectively correspond to 'OFF DS', 'OFF sust', 'OFF alpha trans', 'ON-OFF local-edge W3','ON–OFF local', 'ON–OFF DS 1', 'ON local trans OS', and 'ON slow'. 7 clusters of the 9 mentioned clusters contain an OFF visual response. This shows that there is a relative correspondence between cells with OFF visual response and their electrical input filters. Moreover, for ON RGCs also we can see a similar effect. Clusters 21, 22, 24, 25, 26, 28, 29, 30, 33, and 40 show STAs with positive peaks. These clusters respectively correspond to 'ON step', 'ON DS trans', 'ON local trans OS', 'ON local trans OS', 'ON trans', 'ON trans large', 'ON high freq', 'ON low freq', 'ON mini alpha' and 'ON DS sust. 3' according to Baden et al.'s definition. All putative clusters correspond to ON RGC subtypes which show the correspondence between ON cells and their electrical profiles. These results are in agreement with the previous report of Sekhar et al [4]. The mentioned study reported the correspondence between ON and OFF cells and their electrical STAs but their hypothesis made no prediction for ON-OFF cells. This may explain why some clusters with significant STAs (1, 15, 20, 36, 41) have shapes different from normal upward or downward STAs. These clusters probably contained both upward and downward STAs but their final STAs are disrupted after averaging.
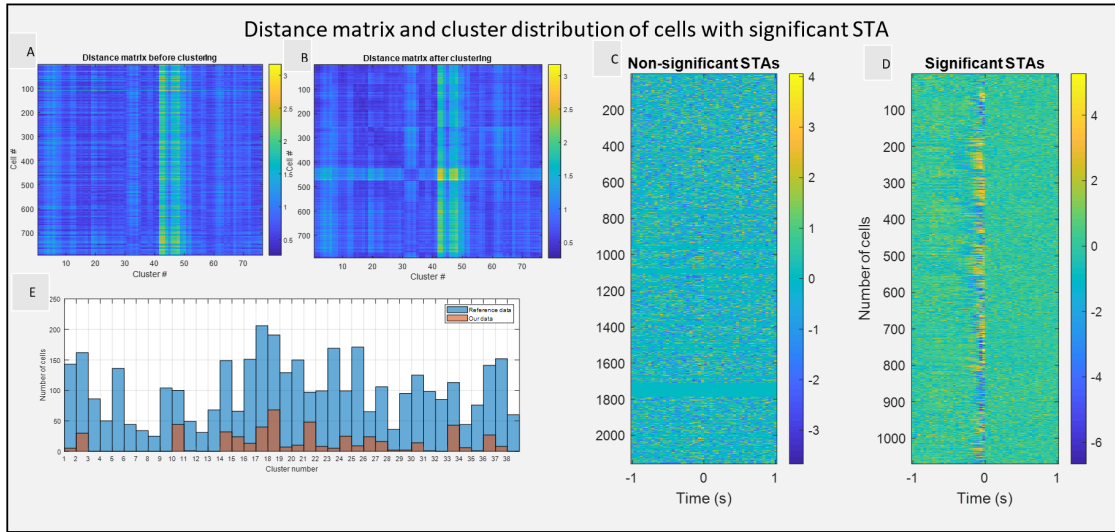
Figure 2.8: Distance matrix and electrical STAs of individual cells. (A, B) Distance matrix before and after clustering. The matrices demonstrat the euclidean distance between the pseudocalcium traces of each cell with calcium traces of reference clusters.(C) Heat map of non-significant STAs. (D) Significant STAs before exclusion of noisy data. (E) comparing cell numbers per cluster for our data versus reference data.

2.4 Discussion

The main purpose of this chapter was to classify MEA based extracellular RGC recordings by matching them with calcium traces and then assign them to one of the 32 clusters defined by Baden et al [16]. Using spike-triggered estimated calcium kernels provided by Baden et al. we were able to transform extracellular electrophysiology recordings to pseudocalcium traces. Although the method failed to detect all defined clusters, especially clusters corresponding to cells with the sustained activity, we were able to assess visual and electrical profiles of the majority of 32 defined RGC types.

2.4.1 Subthreshold Calcium Signals

We speculated that failing to detect all defined clusters is mainly due to the lack of subthreshold signals in pseudocalcium data estimated from spiking activity. The calcium imaging technique is able to capture subthreshold activities caused by low contrast or high-frequency stimulation of chirp stimulus. These subthreshold activities however, were absent in spiking recordings and missed in transformed pseudocalcium traces. We found that most of the clusters in reference data with sustained activity were not detected (e.g. clusters 5-9 and 32), also some of the detected clusters reflected chirp responses with noticeably more transient dynamics than the reference clusters(e.g. clusters 14 and 40).

26
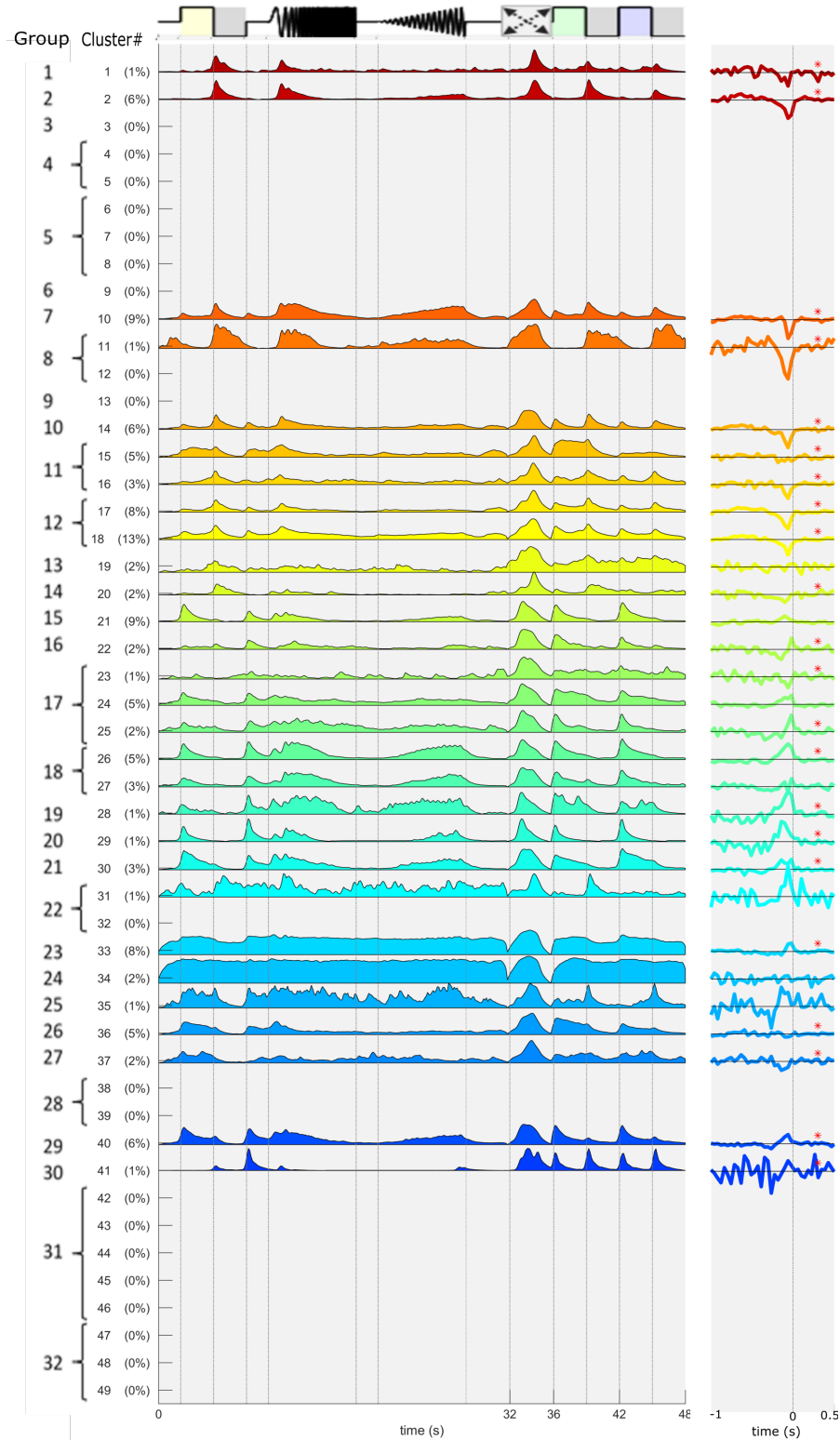
Figure 2.9: Visual responses of 792 Classified RGCs and their corresponding electrical STAs. Left; response to visual stimulation. Right, average of electrical STAs for each cluster. Red points denote a significant deflection in averaged STA (alpha=.001)

2.4.2 Cluster Misassignment

Another reason for having a high number of misassignments is that our data were limited to physiological signals whereas in the Baden et al. study other features such as cell size were used for clustering. For example alpha cells and displaced amacrine cells were re-clustered based on their soma size and staining information after physiological clustering [16]. Since we used the information of all 75 clusters of reference data including ACs clusters, there was the possibility to assign RGCs to ACs clusters or vice versa. For example, only 1% of our data was assigned to the ON-sustained RGC clusters 31 and 32, however about 17% of our RGCs were assigned to ON-sustained amacrine cell clusters.

2.4.3 Direction Selectivity

To ensure that all 8 directions are presented to all recording electrodes we applied the moving bar drifting over the MEA. However, drifting bars were not always centered on the recording electrodes. Therefore, we used the information of 3 closest bars to the recording electrode. In addition to that for each electrode we had to compute the hitting time of the drifting bars to align their responses. Additionally, based on the type of the recorded cells the receptive field size could be different, a parameter that was not included in computing the hitting times. These limitations caused the imperfect alignment of the responses. Also, with only 2 or 3 repetitions of bar stimulus for each location the averaged data were too noisy to detect a reliable direction selectivity index.

2.4.4 Electrical profiles

Ultimately, we examined the electrical profiles associated with each of the 26 clusters matched to reference clusters. As we expected and in agreement with previous reports many clusters had consistent electrical input filters for ON and OFF types [4, 52, 54]. We showed that 7 out of 9 clusters with negative input filters come from the OFF or ON-OFF types of the RGC family and all 10 clusters with positive electrical input filters belong to one of the ON subtype RGCs. Furthermore, we observed that within-class diversity in latency and duration of electrical profiles of ON and OFF cells, although we did not quantify them. These results affirm our hypothesis that different RGC types can be characterized based on their electrical input filter. However, owing to the shortcomings in our classification method such as missed clusters or wrong assignment of some clusters we decided to re-do clustering using a different clustering framework.

In the next chapter we will apply a hierarchical clustering on a spike-based distance metric proposed by Jouty et al. [64]. This gives us the opportunity to detect and examine the clusters that were not detected by the current clustering paradigm. In addition, it allows us to reproduce the known clusters and ascertain the correspondence between their visual and electrical profiles.

CLASSIFYING RGCS BASED ON SPIKE DISTANCE METRICS

3.1 Introduction

The shortcomings in clustering RGCs based on pseudocalcium transformation urged us to search for alternative methods. To minimize errors that come from the presumptions in finding optimum parameters for clustering and to avoid inconsistency between results achieved by different methods we decided to apply a nonparametric method for clustering [65]. Spike distance-based clustering has shown to be an effective method for clustering spiking activity of RGCs in different species like mouse and salamander [59, 64]. Kreuz et al. suggested a parameter-free and scale-independent method for the detection of spike synchrony by using information collected from Inter Spike Intervals (ISI) of instantaneous firing rate [65]. Using information encoded in spike distance, they introduced two complementary measures for computing response dissimilarity profiles; ISI-distance that captures local dissimilarity based on firing rate pattern and SPIKE-distance that measures the dissimilarity profile using differences in spike timings [65, 66].

Depending on the application, each of the two mentioned measures can be used to find dissimilarity profiles of neurons. Jouty et al. proposed a nonparametric method for clustering RGC data recorded by high dense MEA using ISI-distance and SPIKE-distance measures [64]. The advantage of nonparametric clustering is that no search for hyperparameters such as feature representation's dimensionality is required. Using synthetically generated ground truth data, with biological variability, they showed that their method performs the clustering well and is robust to noise. Moreover, the fact that this approach is optimized for clustering cells that are simultaneously stimulated by the same stimulus makes it effective for clustering MEA recordings [64].

PCA-based clustering used in the previous chapter was dependent on the PSTH bin size as well as shape and duration of the OGB kernel used for generating pseudocalcium data. This method does not require these parameters and only implements the information coded in spike times by calculating the spike distance matrix. Furthermore, binning limits time resolution. Since this method does not apply, binning the time resolution is maximized [64].

In addition to studying the response properties of wild-type retina, in this chapter, we will assess the electrical properties of degenerated retina by performing similar experiments on rd10 mouse models with the intention to deepen our understanding of the neurophysiological behavior of the healthy and degenerated retinal circuits during electrical stimulation. Furthermore, by performing pharmacological manipulations on the degenerated retina during the experiments, we aim to elucidate the mechanism by which upward and downward input filters are generated.

3.2 Method

3.2.1 ISI distances

ISI distances measure is the ratio of instantaneous rates of a pair of spike trains. The measure is set to be zero during the iso-frequent period and inclines to +1 or -1 respectively if the firing rate of one of the spike trains increases and the other decreases or vice versa [67]. To compute this measure, the instantaneous distance of each time instance, with the closest spike times occurring before and after that, is computed for each pair of spike trains [66]. In the second step $I(t)$; the ratio of distances for each pair of spike trains over time is evaluated. Finally by summing over the absolute value of $I(t)$ the spike-weighted ISI-distance is computed as follows:

$$x_{isi}(t) = min(t_i^x | t_i^x > t) - max(t_i^x | t_i^x < t) \quad t_1^x < t < t_M^x$$

$$y_{isi}(t) = min(t_i^y | t_i^y > t) - max(t_i^y | t_i^y < t) \quad t_1^y < t < t_M^y$$

$$I(t) = \begin{cases} x_{isi}(t)/y_{isi}(t) - 1 & if \quad x_{isi}(t) <= y_{isi}(t) \\ -(x_{isi}(t)/y_{isi}(t) - 1) & else \end{cases}$$

$$D_I^s = \sum_{i=1}^{M} |I(t_i)|.$$

Where $x_{isi}(t)$ and $y_{isi}(t)$ represent the instantaneous isi distance at the timestamp t for each spike train, and M is the number of spikes, i refers to each spike. ISI-distance can quantify the neurons' spiking (dis)similarities. However, it is not optimized to detect the fraction of coincident spikes that is prevalent in some neural circuits, such as the visual cortex and retina [67]. In order to overcome this issue, Kreuz et al. proposed a new measure called SPIKE-distance. This measure keeps the advantages of ISI-distance, i.e., to be parameter-free and have an adaptive time scale with a focus on spike timing [67].

3.2.2 SPIKE-distance

To compute SPIKE-distance, the previous and the following spike times are detected for each time instant using the following formula [66]:

$$t_P^{(n)}(t) = max(t_i^{(n)}|t_i^{(n)} \le t) \quad t_1^{(n)} \le t \le t_{M_n}^n$$

$$t_F^{(n)}(t) = max(t_i^{(n)}|t_i^{(n)} > t) \quad t_1^{(n)} \le t \le t_{M_n}^n$$

where n is the number of spike trains. Then the time interval between two spike times is computed as follows:

$$x_{isi}^n(t) = t_F^{(n)}(t) - t_P^n(t)$$

In the next step, the distance between the previous and following spike time pairs is calculated as follows:

$$\Delta t_P(t) = t_P^1(t) - t_P^2(t)$$

$$\Delta t_F(t) = t_F^1(t) - t_F^2(t)$$

Finally, the SPIKE-distance S(t) will be defined as follows:

$$S_1(t) = \frac{\frac{\Delta t_P^{(1)}}{x_P^{(1)}} + \frac{\Delta t_F^{(1)}}{x_F^{(1)}}}{\frac{1}{x_P^{(1)}} + \frac{1}{x_F^{(1)}}}$$

$$= \frac{\Delta t_P^{(1)} x_F^{(1)} + \Delta t_F^{(1)} x_P^{(1)}}{x_F^{(1)} + x_P^{(1)}}$$

$$= \frac{\Delta t_P^{(1)} x_F^{(1)} + \Delta t_F^{(1)} x_P^{(1)}}{x_{ISI}^{(1)}}$$

$$S(t) = \frac{S_1(t)x_{ISI}^{(2)}(t) + S_2(t)x_{ISI}^{(1)}(t)}{2\langle x_{ISI}^{(n)}(t)\rangle_n^2}$$

$$\Delta t_P^{(1)} = min(|t_P^{(1)} - t_i^{(2)}|)$$

Similar to ISI-distance, this measure evaluates the instantaneous (dis)similarity time profiles of each pair of spike trains. Figure 3.1 shows the comparison of Spike-distance versus ISI-Distance for multivariate artificial spike trains. In the first half of the spike trains plot, there are some synchronised spiking events (samples 400,800 and 1200) with noisy background and in the second half, there are spiking events with less noise in the background. An ideal measure of synchrony

should be able to report the synchronised events regardless of the background noise. Figure 3.1 shows that for this sample data the SPIKE-distance metric can track the spike train synchrony faithfully during the noisy period by showing a reduction in the SPIKE metric, whereas the dissimilarity index is increased for ISI-distance metric during the same time period.
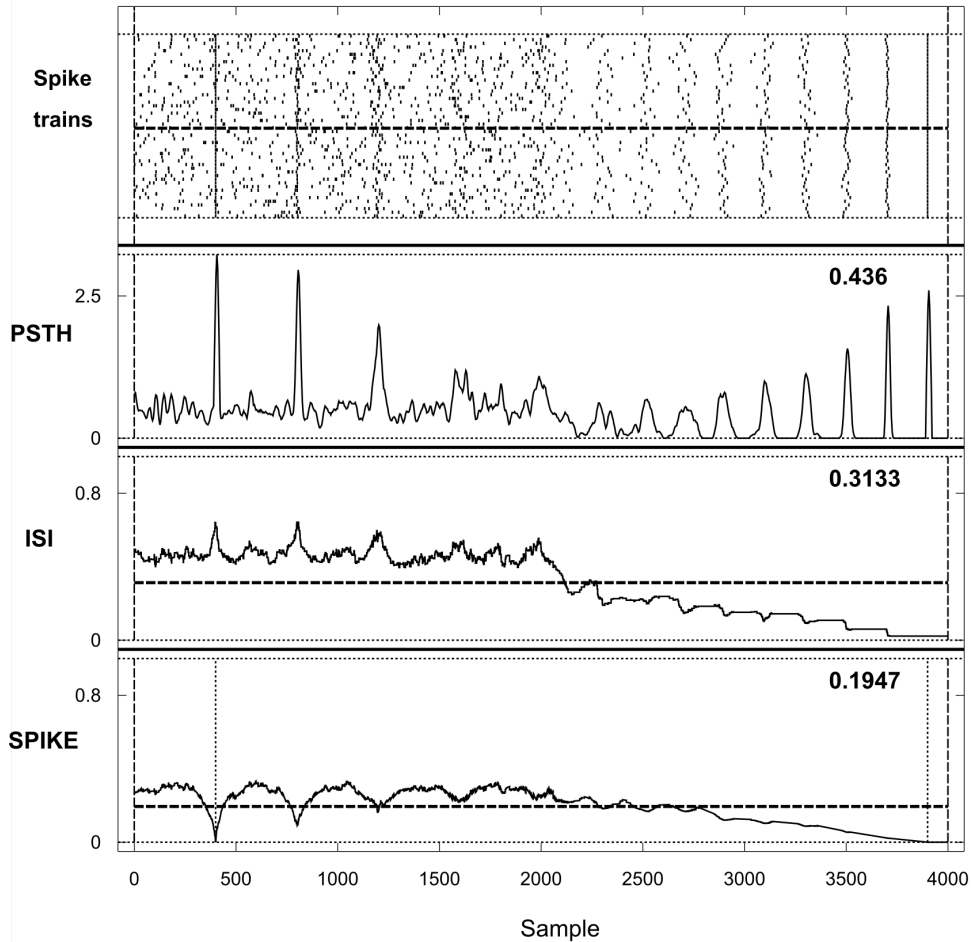
Figure 3.1: Evaluating ISI-distance and Spike-distance for synthetic data. First row shows the artificial spike trains. Second row shows the PSTH. Third row represent the instantaneous value of ISI-distance (Lower values represent higher synchrony). Last row illustrates the instantaneous value of Spike-distance and shows that this measure outperforms in detecting spike synchrony in presence of the noise. Synthetic data and plots are generated by SPIKY toolbox (Kreuz et al. 2015).

To assess the validity of the ISI and SPIKE-distance on our data we computed the measures for three sample neurons with different patterns of activity in response to identical stimuli (figure 3.2). For stimulus-driven cells with lower background noise and a higher level of synchrony, both

ISI and SPIKE-distance metrics had smaller values for either full-flash and chirp data. This implies that in addition to the separation of stimulus-driven cells with different patterns of activities the measure is able to distinguish noisy data as a separate cluster. Figure 3.2.A shows a stimulus-driven cell with background noise. Compared to (B) which is less noisy, both distance measures are higher for cell (A); Respectively 0.45 and 0.25 versus 0.38 and 0.17 for ISI and SPIKE-distances. Figure 3.2.C shows the activity of a noisy unit in response to chirp stimulus. The value of ISI and SPIKE-distance are highest for this unit; 0.51 and 0.29 respectively, which reflects the low synchrony across trials. The three plots in the right column (D, E, F) show similar results for flash stimulus.

After computing, ISI and SPIKE metrics the distance matrix was computed for all single cell pairs. Since the measures fulfill the requirement of non-negativity and symmetry, agglomerative clustering can be implemented to construct a dendrogram for hierarchical clustering [64]. In this method, each unit is considered as a separate cluster, then iteratively, and based on a variance constraint the clusters are merged to reach the best result. In order to set the dendrogram cut-off point, different criteria can be used. Similar to Joutyet al. we used two measures to estimate cluster numbers. At first, we computed a measure called the gap statistic. This measure uses the shuffled distance matrix as a random surrogate data and compares it with clusters computed by agglomerative clustering [64, 68]. It has been reported that gap statistics can be too conservative in terms of cluster numbers for data with higher variability [64]. In addition to that, we also computed the Adjusted mutual information [69] as a consensus method to estimate the valid number of clusters.

Additionally, t-distributed Stochastic Neighbor Embedding (t-SNE) was used to assess the quality of clustering. This measure plots the two-dimensional embedding of high dimensional data using non-linear transformation. [70].

3.2.3 ON-OFF bias index and direction selectivity

The ON-OFF bias index was computed based on the Carcieri approach [58]. This method uses the spiking activity of neurons to show the relative amplitude of ON and OFF responses and is computed as follows:

$$OOi = \frac{\langle r_{ON} \rangle_t - \langle r_{OFF} \rangle_t}{\langle r_{ON} \rangle_t + \langle r_{OFF} \rangle_t}$$

Where $\langle r_{ON} \rangle_t$ and $\langle r_{OFF} \rangle_t$ are spike numbers during light on and light off periods respectively. This measure was not used for clustering and used to evaluate the performance of the clustering method [64].

Direction Selectivity Index (DSI) was computed according to the Jouty et al. approach [64]. In this approach, the relative maximum firing rate is computed for each of the 8 directions and then transformed to a vector that represents each direction. Two first eigenvalues of the vector are used to compute the DSI index:
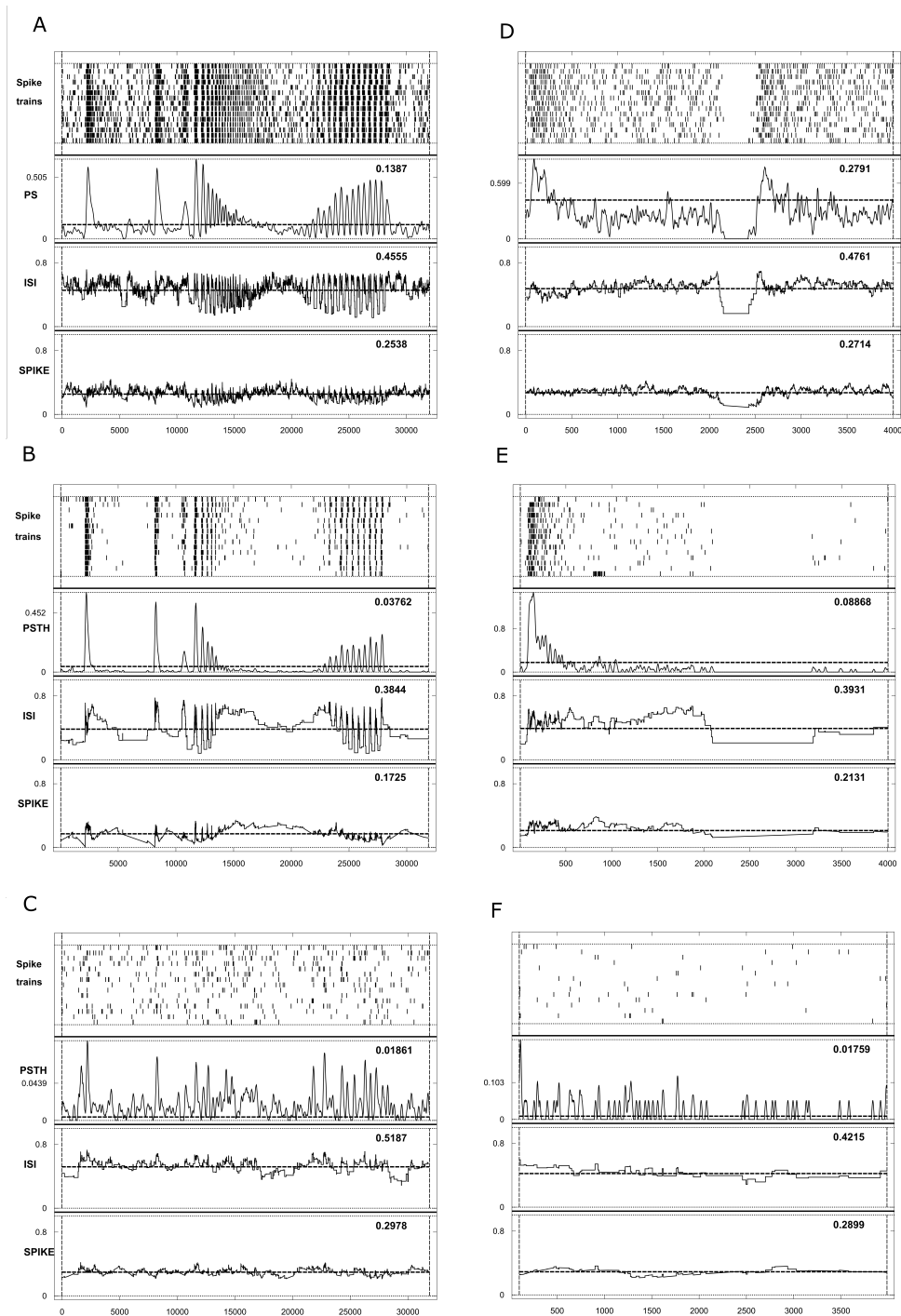
Figure 3.2: ISI and SPIKE-distance metrics for three sample neurons in response to chirp (A, B, C) and flash (D, E, F) stimulus. Each sub-plot shows the spike raster, PSTH , ISI-distance and SPIKE-distance respectively from top to bottom.

$$DSi = 1 - \frac{\lambda_1}{\lambda_2}$$

3.3 Results

3.3.1 Clustering healthy mouse retinal ganglion cells.

The electrical activity of 2632 detected units from 22 wild type C57Bl/6 mouse retina recorded with 60 channel MEA (see method), was used for clustering. Only units with a significant STA were used for clustering. To test the significance of STAs, the null hypothesis that the data came from a normal distribution was tested using Python *normaltest* function. The units with a p-value >.001 are considered as non-significant STAs. This left 476 cells with significant STAs. In the next step, the ISI histogram was computed for all cells. Cells whose average of ISI were two-fold larger than the σ (standard deviation) of all data were considered as outliers. In addition, the Pearson correlation between full-field flash stimulus and PSTH was computed for each cell. Only cells with a correlation value higher than 0.1 were included for clustering. Ultimately, similar to chapter two, the ratio of the average of variance across trials to the variance of the whole responses were computed. Cells with a variance ratio less than one were used for final clustering. This yields a total number of 269 cells for analysis (figure 3.3).
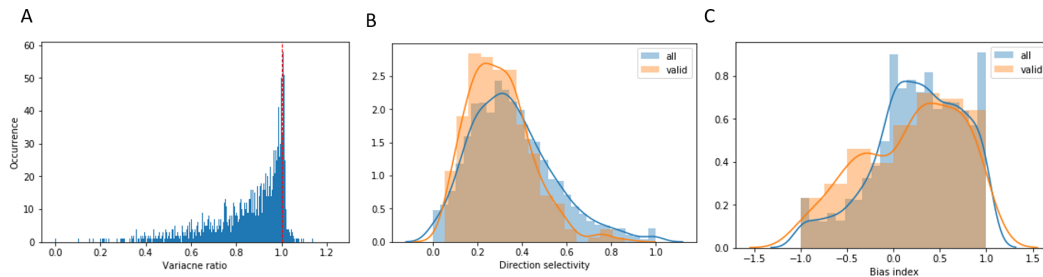
Figure 3.3: Distribution of variance ratio, Direction selectivity and ON-OFF bias index. (A) Distribution of variance ratio of wild-type data. Units with Variance ratio >= 1 excluded from analysis. (B) distribution of DSI index for wild-type data. Higher values reflect more direction selective cells. Blue, all recorded units. Orange, data included for final clustering. (C) Distribution of ON-OFF bias index computed from full-filed flash data.-1 indicates OFF preference, +1 indicates ON preference, and zero reflects no preference. Blue shows the occurrence rate for all units, Orange shows the occurrence rate of the units that included for final clustering.

3.3.2 Clustering

As mentioned earlier we used the RGC clustering toolbox provided by Jouty et al. (`https://github.com/mhhennig/rgc-classification`). Clustering was performed in two modes. In the first step, clustering was performed based on light-evoked responses and the corresponding

electrical STA of each cluster was assessed. In the second step, the estimated STAs extracted from electrical noise stimulation were used for clustering. Results of the first step will help us to detect different RGC types and see their corresponding electrical input filters. The results of the second step helps us better address the diversity of electrical profiles and evaluate their corresponding visual characteristics.

Spike distance-based information collected from full-field flash, color, and chirp stimuli were used for clustering light-evoked activity recordings. For electrical induced activity, hierarchical clustering was performed on 1 sec from temporal STA's before time zero ($-1 \leq t \leq 0 \quad (sec)$).

Extracting the gap statistics of the Jouty et al. dataset showed a peak at 17 clusters. Applying this measure to our data (the light-evoked activity of healthy retina) yielded values between 9 to 13 for different visual stimuli (figure 3.4.A). Since the number of clusters was much smaller than the 32 clusters suggested by the reference study of Baden et al., adjusted mutual information was used as an alternative metric as it was suggested by Jouty et al. [64]. They compared mutual information of ISI and SPIKE distance and reported that the highest cluster number can be achieved by SPIKE-distance metric with peaks on 17 and 28 clusters for full-field and chirp data respectively. After assessing the confusion matrices and the value of mutual information for different stimuli across different cluster numbers they finally chose the SPIKE-distance metric as an optimum metric for final clustering. Extracting adjusted mutual information of SPIKE distance for our data showed peaks at 4 and 18 for full-field and chirp data respectively. After combining all three stimuli (full field flash, chirp and color) adjusted mutual information metric peaked at 37. Ultimately by considering the 32 as a reference cluster number, the overlap between clusters obtained with ISI-distance and SPIKE-distance metrics, and visual observation of obtained clusters, we set cluster numbers at 37 for clustering visual-induced activity of the healthy retina (figure 3.4).

Figure 3.5 shows the result of the clustering that includes light-evoked responses to full field flash, chirp, and color stimuli as well as the distribution of DSi index and electrical input filter profile for each cluster. The average PSTH of corresponding clusters are shown in each row (binsize=20ms). Despite applying strict criteria for removing noisy units, there are still some clusters with a high level of noise in their light-evoked responses and might not reflect the activity of a specific RGC type. A similar observation was reported by Jouty et al. indicating that this method can sort noisy data in a separate cluster.

Assessing chirp responses reveals that different light-evoked patterns with diverse temporal kinetics and contrast sensitivity are detected by the algorithm. The dendrogram is colored based on the ON-OFF bias index (red=ON, green=OFF). This helps us see how well ON and OFF cells are separated using this clustering paradigm. The dendrogram organization loosely correlates with the ON/OFF index with green toward the OFF end and purple/red toward the ON cells.

Since in this study we aimed to characterize the electrical properties of RGCs, we focus on the electrical profile of each cluster. Clusters 1 to 7 form a sub-branch of the hierarchical tree that
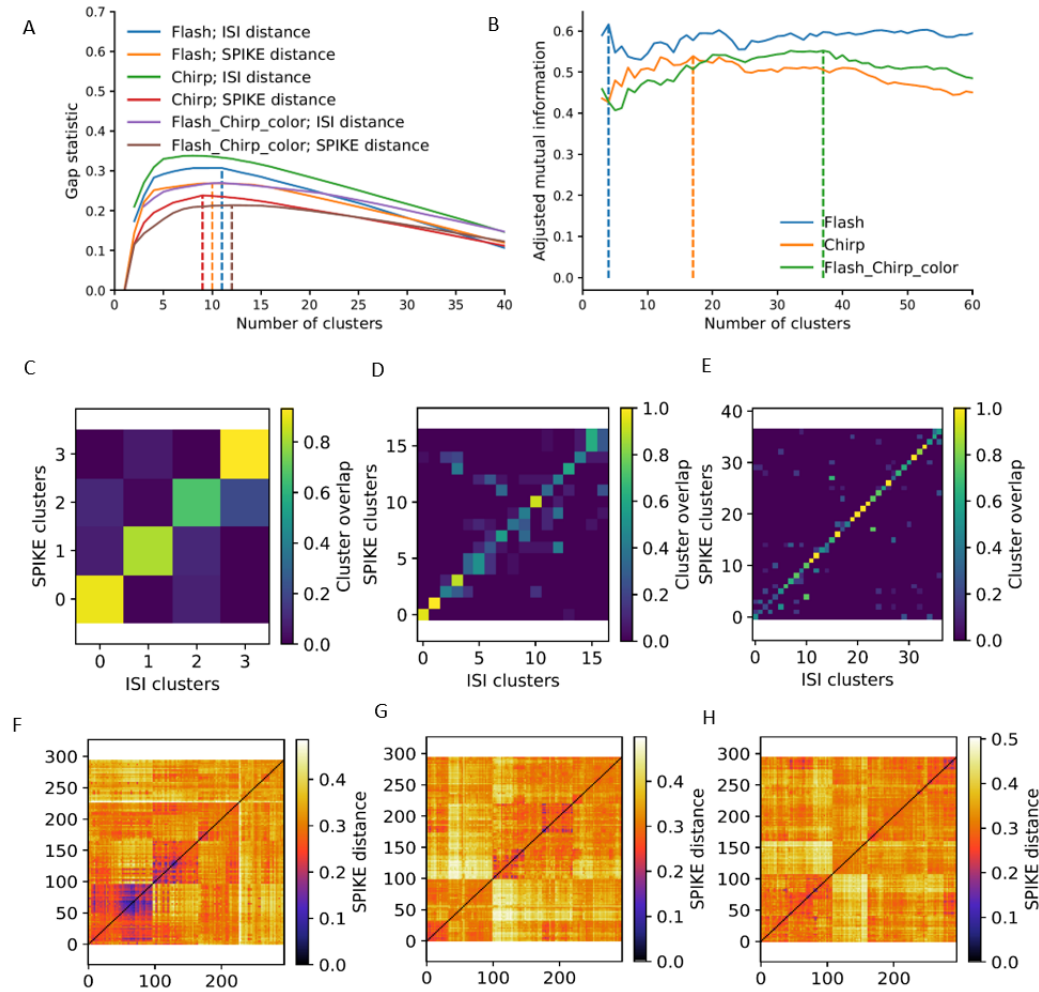
Figure 3.4: Comparing GAP distance and Mutual information for wild-type retina. A. Gap statistics of ISI and SPIKE-distance metrics for responses to different visual stimuli (flash, chirp and combination of flash, chirp and color). The highest value for each dataset is shown by vertical lines that correspond to optimum cluster number. B. Mutual information between ISI and SPIKE-distance metrics for different visual stimuli (flash, chirp and combination of flash, chirp and color). The measure peaked at 4,17 and 37 respectively. C. Cluster overlap after applying hierarchical clustering on ISI and SPIKE-distance with 4 clusters. D. similar to C for 17 clusters. E. same as C with 37 clusters. F. Distance matrix of clustered unit with 4 clusters using Spike-Distance. G. same as F with 17 clusters. H. Same as F with 37 clusters.

is dominated by OFF cells. In most of these clusters (1, 3, 5, 6 and 7), we can see a monophasic *downward STA*. Clusters 8-10 form another sub-branch of the hierarchical tree with two ON cells and one ON-OFF cell. The cluster with ON-OFF activity reflects the STAs with a negative peak. Clusters 11-15 and 16-24 from two other sub-branches and include a mix of ON and OFF preference mostly with a high level of noise. Among clusters 11 (OFF), 16 (ON-OFF), 17 (ON), and 18 (OFF) that reflect light-stimulus driven activity, clusters 17 (ON) and 18 (OFF) have upward

and downward STAs respectively. Clusters 25-31 are located in another sub-branch and represent a mixture of ON, OFF, and ON-OFF preference. Clusters with OFF and ON-OFF activity (25-28, 30) have monophasic *downward STAs* whereas in ON clusters (29,31) deflections are eliminated after averaging. Clusters 32-37 shape the last sub-branch of the hierarchical tree. Except cluster 33, the light-evoked activity of the other 5 clusters reflect only the response of the cells with ON preference (clusters 32, 34-37) in four of them (clusters 32, 34-36) the average of STAs has an upward deflection.

To get a better look over the visually clustered cells and their corresponding electrical STAs we sorted representation of clusters based on the ON-OFF bias index value of each cluster(figure 3.6). With this new visualisation it is easier to visually inspect the relationship between RGC types and their electrical input filters. Almost all clusters with a bias index value smaller than -0.5 (at the top of the plot) reflects *downward STAs*. Also, for clusters with the bias index larger than 0.5 (at the bottom of the plot) three clusters have meaningful STA, with *upward STAs*. The other four clusters have a diversity of STAs being averaged, suggesting that the clustering might not be accurate or that these clusters don't have a characteristic STA shape. Clusters with the bias index value closer to zero include cells with ON-OFF preference or noisy data. The average of STAs for most of these clusters are flat.

As a summary, we observed that many OFF preference clusters have STAs with downward deflection while none of them showed STAs with upward deflection. Analogously, for clusters with ON preference, we observed positive STAs. These results confirm previous findings [4, 52–54] that electrical input filters of ON cells have a dominant positive peak and electrical profiles of OFF cells show a negative peak. Nevertheless, in the mentioned studies only the electrical characteristics of two major ON and OFF cell types were elaborated. Although the clustering framework used in the current work is able to detect a wider range of RGCs, a clear difference between the electrical profiles of sub-types of ON and OFF cells was not observed. To elaborate the diversity of electrical STAs in a more systematic way we performed similar hierarchical clustering on electrical STAs. The results are presented in the following section.

To check the clustering quality, we also plotted the 2d representations of the PSTH of clustered data using the t-SNE method (figure 3.7). The plots are shown for full-field flash, chirp, and combination of all stimuli. Each point represents one cell and the color of each point indicates cluster membership. The distance between points does not necessarily represent the similarity, but the overall colored structures show the limitation of the area of each cluster [64]. In the right column of the figure, data points are colored according to the ON-OFF bias index. The spatial proximity of similar colors indicates that this feature is captured well by the clustering algorithm.

3.3.3 Clustering electrical STAs of healthy retina

To see the diversity of electrical profiles of recorded RGCs we performed agglomerative clustering on electrical STAs of individual cells. This helps us to figure out to what extent the shape of these
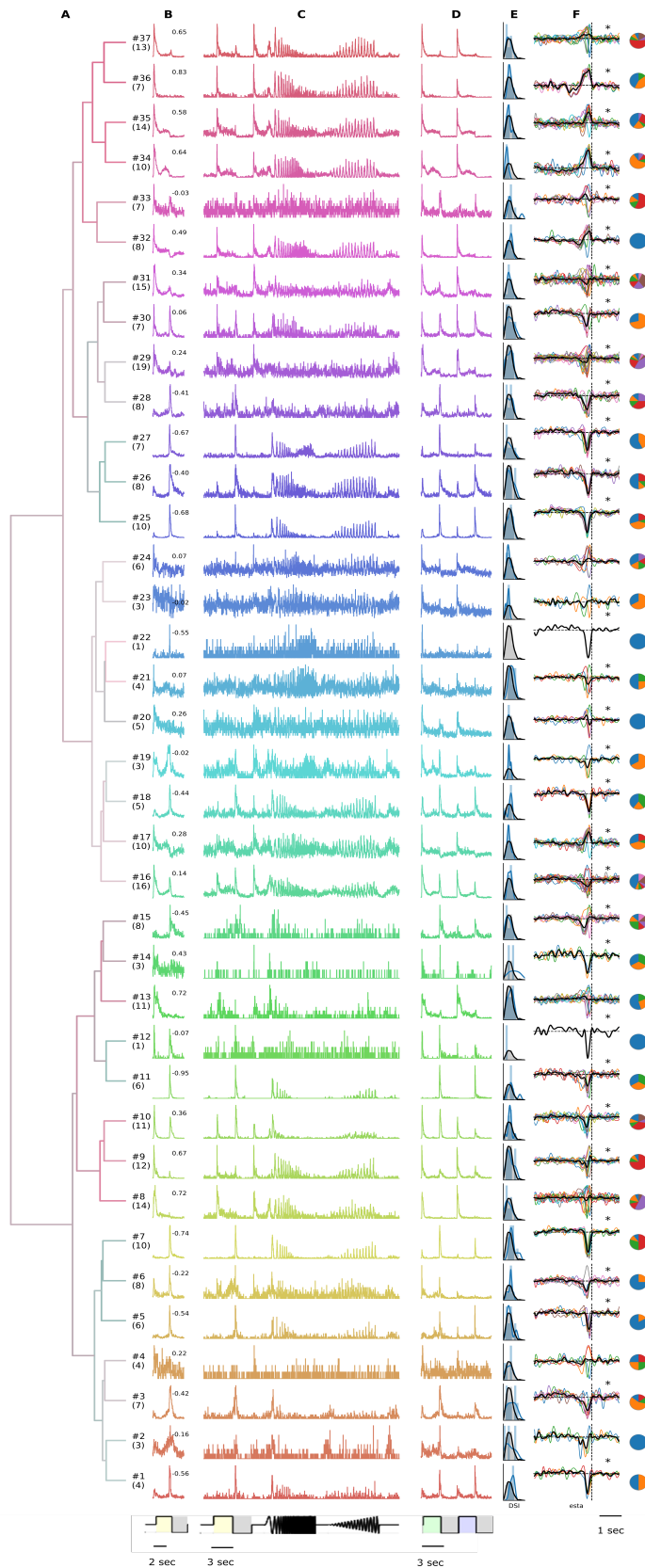
Figure 3.5: Hierarchical clustering of wild-type retina RGCs. (A) Cluster dendrogram of 37 detected clusters based on adjusted mutual information criteria (see figure 3.4.B). (B, C, D) Respectively, the PSTH of visual-induced activity of full field flash, chirp and color stimuli. Numbers on plots at (C) denotes the ON-OFF bias index for each cluster. (E) Histogram of direction selectivity index. (F) Corresponding electrical input filters of each cluster. Colored traces show e-STA of each individual cell. Black trace shows the average of e-STAs for one cluster. Significant deflections are marked with black asterisks (alpha=0.0001). Pie charts show the proportion of the neurons form each recording. Each color in pie charts represents one retina.
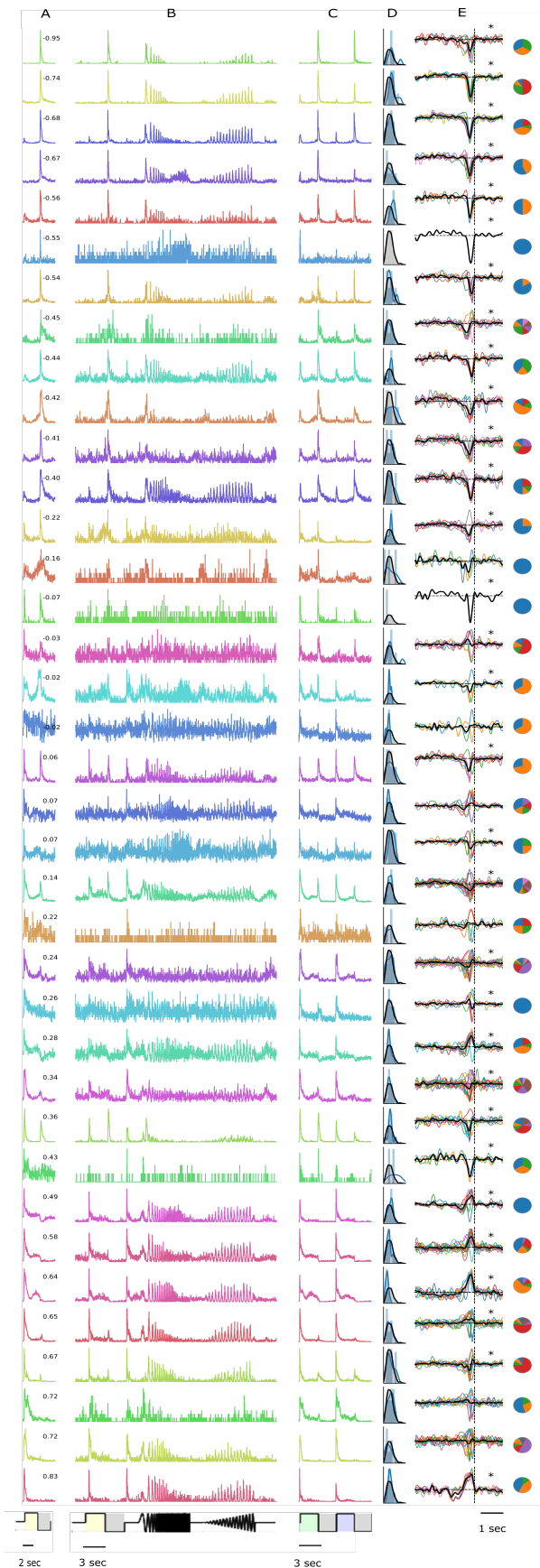
Figure 3.6: Reordering clustered data based on ON-OFF bias index. (A-E) correspond to (B-F) in figure 3.5. Color map is similar to figure 3.5.
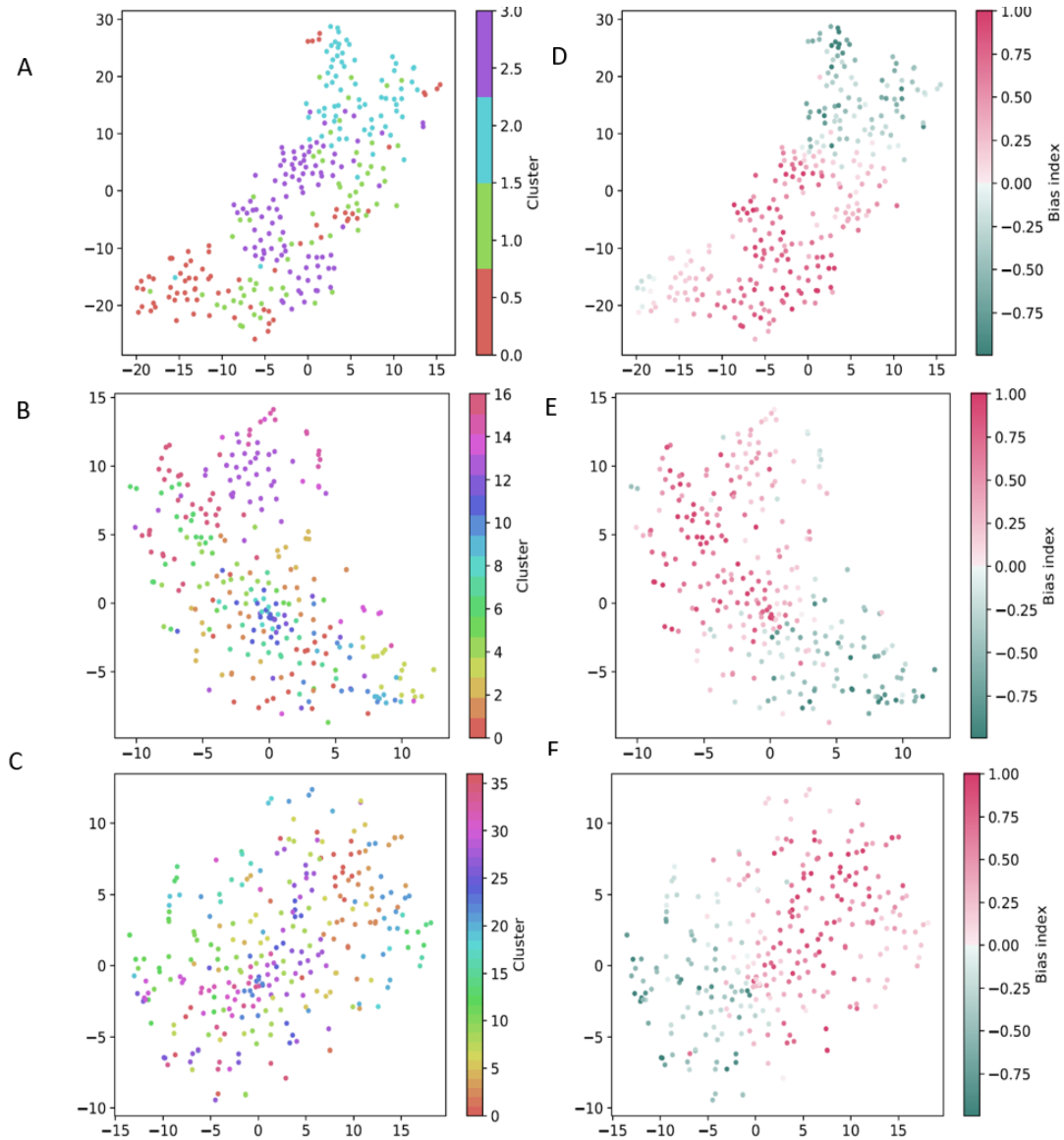
Figure 3.7: t-SNE plots of PSTHs for different visual stimuli. (A, B, C) Respectively, t-SNE embedding generated from full field flash, chirp and combination of all stimuli. For these plots color codes indicate the clusters membership. (C, D, E). t-SNE embedding for the same data in the left column. For these plots units are colored according to the ON-OFF bias index.

STAs can vary across different units. Also, it allows us to compare the light-evoked activity of the cells with different electrical input filters. To assess the frequency spectrum of the STAs, the Power Spectrum Density (PSD) of each STA is computed using the Welch method [71].

The gap statistic metric peaked at 15 clusters for STA data. Hierarchical Clustering of STAs into 15 clusters divided them into two main branches (figure 3.8). Clusters 1 to 7 form the first branch. All of them include STAs with a positive deflection prior time zero, we name them *upward*

STAs. Inspecting the light-evoked activity of these clusters for full field flash stimulus reveals a high level of ON preference all with a positive ON-OFF bias index (figure 3.8.C). The same behavior can be observed for green and blue visual stimuli of color stimulus(figure 3.8.E).

Clusters 8 to 15 are located in the second branch, all of them show a strong negative deflection before time zero. We name these clusters *downward STAs*. While clusters with upward STAs reflect no OFF preference in their light-evoked responses, all clusters with downward STA include OFF preference in response to full field flash and color stimuli. This indicates a lack of contribution of OFF cells in generation of upward STAs and a high contribution of OFF cells in the generation of downward STAs. Different levels of contribution of ON preference can be observed in clusters with downward STA. For example, clusters 9 and 12 show OFF preference while clusters 8 and 11 represent the combination of ON and OFF preference. Cluster 5, shows biphasic STAs. This cluster can be assigned to a separate group named *biphasic upward STA*. The ON-OFF bias index value of the cluster is 0.19, which is much smaller than the other cluster with upward STA.

The average of PSDs of STAs of each cluster is shown in Figure 3.8.G. For most of the clusters the PSD has a peak at the frequency range smaller that 3 Hz, whereas the clusters with more biphasic shape STAs (clusters 5 and 6) show a peak at higher frequencies (4.4 Hz and 3.6 Hz respectively). It is worth noting again that this clustering is done only based on electrical STAs and none of the visual features were included for clustering. Table 3.1 shows the frequency of the peaks of PSDs and the bandwidths at 50% of PSD for 15 identified clusters of figure 3.8.

To evaluate the clustering quality, similar to light-evoked clustering, we used the t-SNE method to show data in a 2d plane with the same cluster color maps (figure 3.9.A). Additionally, by computing 1st, 2nd, and 3rd Principal Components (PCs) using principal component analysis we showed the projection of electrical input filters on the 2d plane (figure 3.9). Both plots show a decent separation of clusters.

As a summary, clustering wild-type retina RGCs based on both light-evoked responses and electrical-stimulation responses revealed that there is a consistent correspondence between visual and electrical profiles for two major categories of ON and OFF RGCs. Although including 7 different clusters we observed an inside-class diversity for *upward STAs*, no significant difference was observed in their visual activity. For *downward STAs* on the other hand, a higher diversity including 8 different clusters was detected. For some of these clusters, the visual preferences are distinguishable from one cluster to another.

3.3.4   Rd10 retina

Since in real-world application the retina implants are used by patients whose retina photoreceptors are degenerated, we decided to perform similar experiments on mice with the degenerated retina. We used the rd10 mouse model to better understand how a progressively degenerated retina responds to electrical stimulation. Furthermore, it allows us to compare electrical profiles
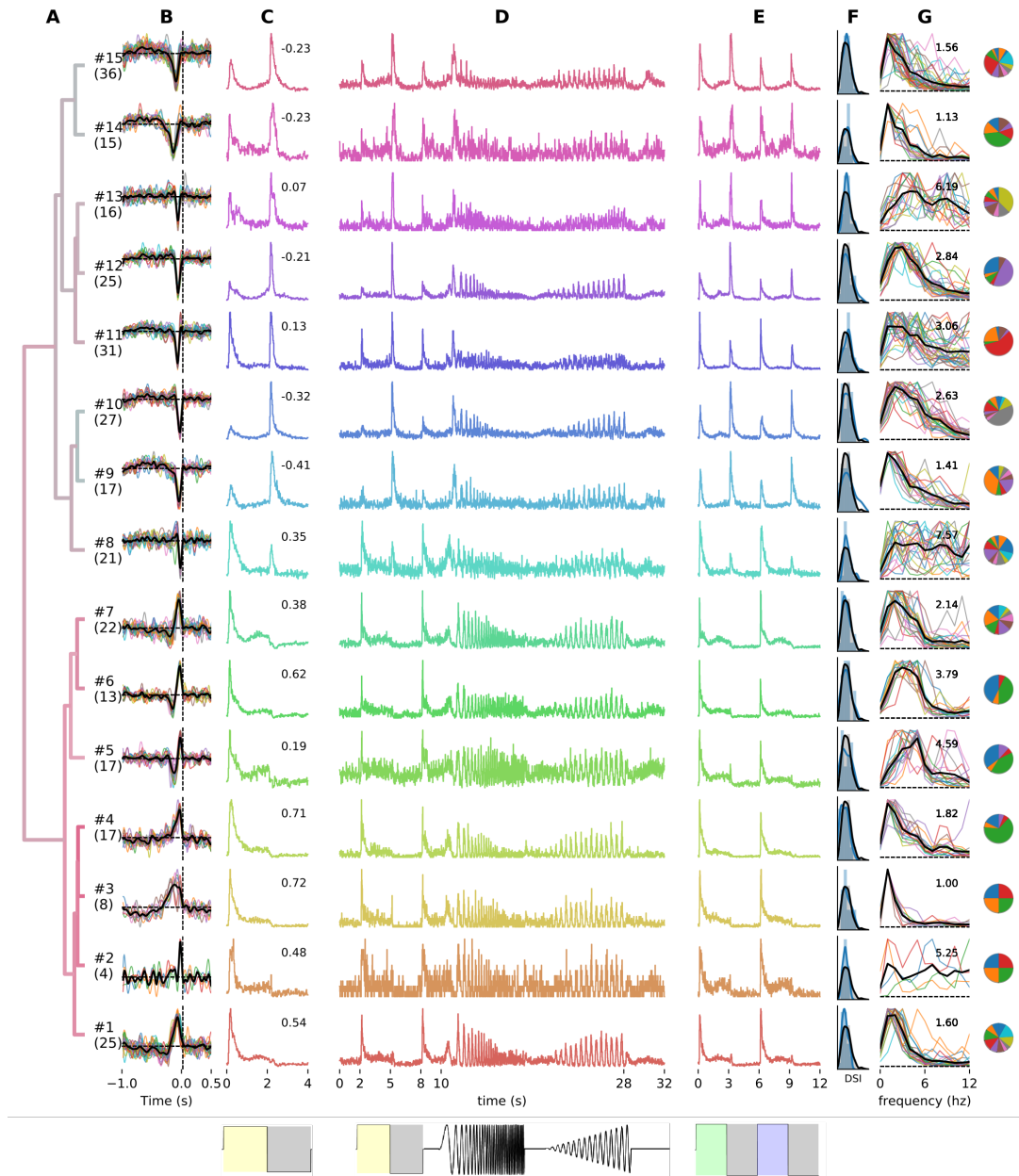
Figure 3.8: Hierarchical clustering of electrical input filters of wild-type retina shows correspondence between visual electrical profiles of RGCs. (A) cluster dendrogram shows two branches. (B) Clustered electrical input filters. First branch includes 5 clusters of STAs with a positive peak. Second branch contains 7 clusters of STAs with a negative peak. (C, D, E) visual induced activity of Full field flash, chirp and color stimulus respectively. The numbers at plot (C) represents the ON-OFF bias index of each cluster. All cells in the first branch (clusters 1-7) respond only to stimulus onset. While, in the second branch (clusters 8-15) the light-evoked responses reflect the sensitivity to stimulus offset. Some of them have ON-OFF preference and some of them only OFF preference. (F) distribution of direction selectivity index (similar to Joutyet al). (G) Power spectrum of individual STAs(colored) and the average of power spectrum of STAs for each cluster(black). The number on each plot shows the frequency at which the peak of the average of the power spectrum occurs. Pie charts show the proportion of the neurons of each recording. Each color represents one retina.

43

Table 3.1: Power spectrum features of STAs for each cluster of wild-type data. Columns from left to right: cluser number, frequency of peak of PSD, lower band frequancy of 50% of PSD, upper band frequancy of 50% of PSD, band width of the 50% of PSD.

$Cluster\#$	$Peak-freq$	$f1_{50\%}$	$f2_{50\%}$	BW
1	1.6	1.08	2.84	1.76
2	5.25	3.75	9.5	5.75
3	1	1	1.75	0.75
4	1.82	1	4.12	3.12
5	4.59	2.94	6.06	3.12
6	3.79	2.07	4.79	2.71
7	2.14	1.41	4.05	2.64
8	7.57	2.57	9.57	7
9	1.41	0.94	4.35	3.41
10	2.63	1.44	4.93	3.48
11	3.06	1.65	6.68	5.03
12	2.84	1.48	4.4	2.92
13	6.19	3.19	8.41	5.12
14	1.13	1.13	2.93	1.8
15	1.56	1.06	3.28	2.22
Median	**2.63**	**1.44**	**4.4**	**3.11**

of the degenerated retina with wild-type retina. Since the rd10 model has a later start and slower pace of photoreceptor degeneration compared to the rd1 mice model it can be considered as a better model of retinitis pigmentosa. Ultimately, the electrical and visual-induced activity of 4 rd10 degenerated retina were used to assess their electrical property. We employed the same electrical and visual stimulation sets used for the wild-type experiment with the exception that visual noise and moving bar stimuli were not used for these experiments. Age of all four rd10 retina were between p29 to p31 and the visual-induced activity was observed in some cells. In addition to that, to investigate the mechanism underlying the spike generation in the degenerated retina during electrical stimulation, we performed pharmacological manipulation of the network while recording RGCs activity. The Selective group III metabotropic glutamate receptor agonist L-AP4 was used to block the synaptic connection of Photoreceptor-ON bipolar cells [72]. Full-field flash and color stimuli were used for light stimulation. Clustering was performed based on light-evoked responses to full-field flash and color stimulus before injection of blocker. Color stimulus data after application of the blocker were not used because of the incomplete data recording for this stimulus.
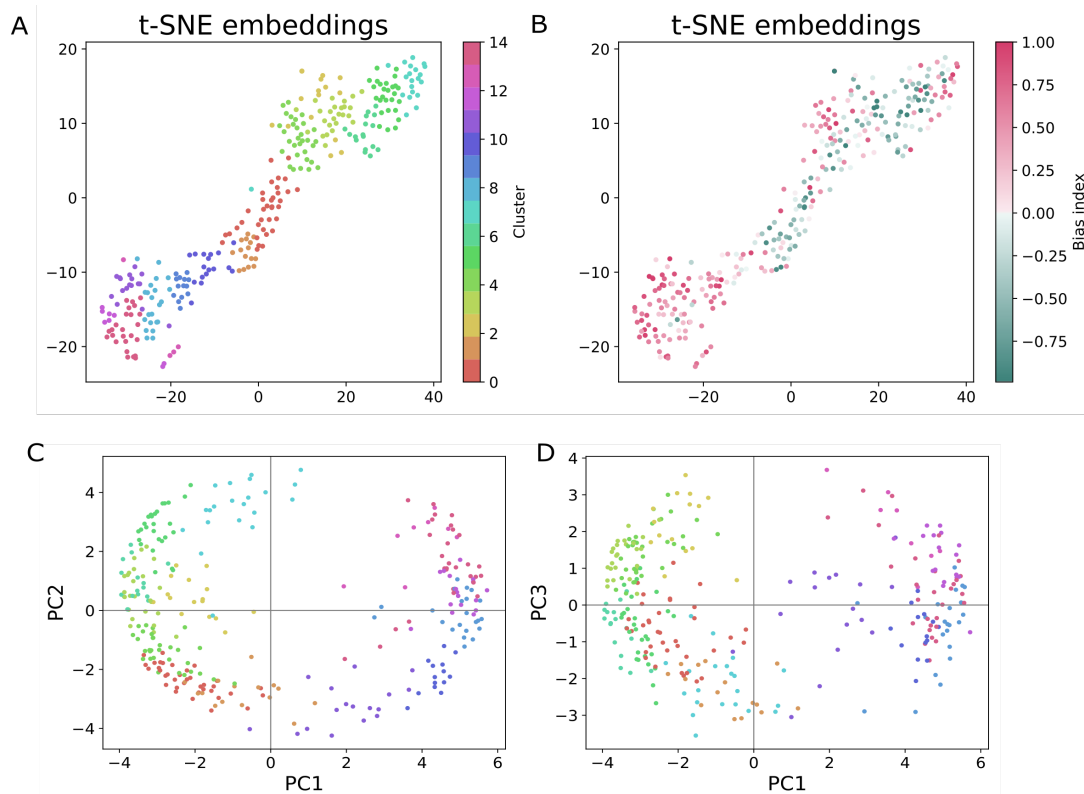
Figure 3.9: t-SNE plot and scatter plots of projection of STAs of wild-type retina onto first, second and third principal components. (A) t-SNE embeddings of STAs. Each point represents one unit. Colors represent cluster assignment. Color map is the same as figure3.8. (B) t-SNE embeddings of STAs colored based on ON-OFF bias index. (C) projection of STAs on 1st and 2nd PCs. (D) projection of STAs on 1st and 3nd PCs. Colors represent cluster membership.

3.3.5   Oscillation in rd10

cGMP is the messenger molecule that plays the main role in the absorption of light energy and converting that to neurochemical changes in the retina. Defects in the Pde6b gene that are supposed to encode -subunit of rod photoreceptor cGMP phosphodiesterase type 6 leads to degeneration of the retina. The gene symbol Pde6brd1 is abbreviated as rd1. The Rd1 model causes the death of rods in the first week of postnatal [73]. The Rd10 model was developed later and has a missense of mutation in the same gene but with a later and slower rate of degeneration. It has been shown that the rd10 retina has a higher spontaneous activity with oscillatory rhythmic patterns. Goo et al. reported 5hz phase-locked spontaneous activity in rd10 [73]. Biswas et al reported 3–7 Hz oscillation frequency in the same mouse model [74]. Although the mechanism underlying the generation of these oscillations is not understood well, recent studies suggest that these oscillations originate from the coupled networks of On-bipolar cells and AII amacrine cells [75]. Biswas et al. showed that glutamatergic excitation of cone bipolar cells might be the reason for rhythmic activity [74]. Menzler et al. reported that rhythmic RGC

spiking can be abolished by the inhibition of ionotropic glutamate receptors in the rd1 retina [76].
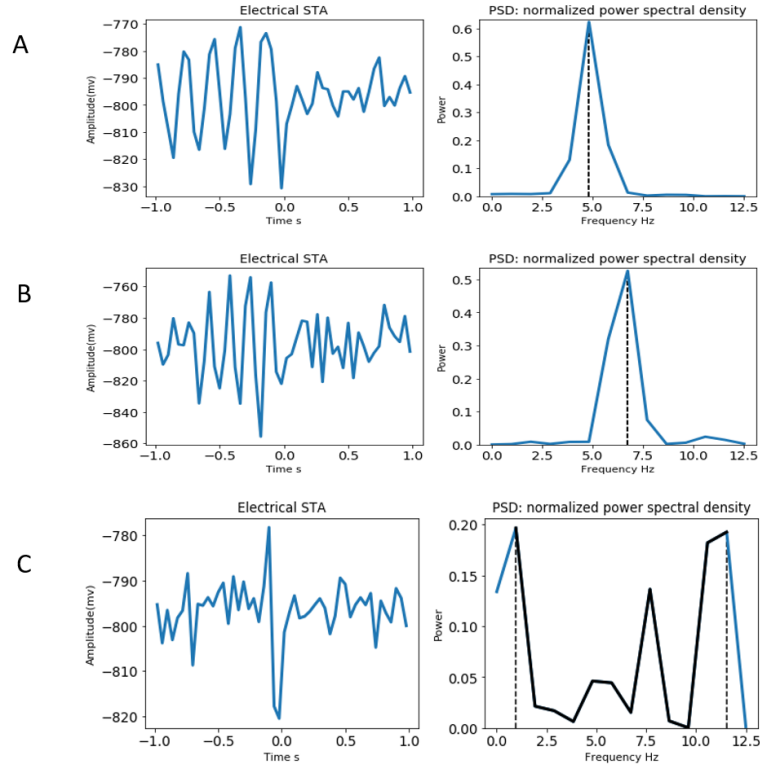
Figure 3.10: Power spectrum of three sample rd10 STAs. (A) Time domain presentation (left) and PSD (right) of a sample STA with 5 Hz rhythmic oscillation. (B) Another sample STA with 7 Hz rhythmic oscillation. (C) Sample biphasic STA without oscillation. Dashed vertical lines show the region that include at least 50% of total power

Since the rd10 retinas used in this study were not older than 6 weeks, their photoreceptor layer was not completely degenerated. Therefore, some recorded RGCs might show light-evoked activity, and clustering can be performed based on visual activity. Extracting the electrical STAs of rd10 RGCs revealed a diverse pattern of oscillations. For some cells that were not sensitive to light stimulation, we observed rhythmic oscillation between 5Hz and 7Hz in their electrical STAs (figure 3.10).

Although there is an oscillatory pattern in the spontaneous activity of these cells, by inspecting the electrical STAs we can see that the phase of oscillation is synchronized with stimulus which shows the influence of electrical stimulation on these oscillations. For most of the cells, however, the oscillations vanished after the injection of the blocker. For those RGCs that were responsive to light stimulation, we could observe biphasic STAs as well. Figure 3.11 illustrates either light-evoked or electrical response of three sample cells with different STA patterns. Left plots demonstrate the response properties of the cells before application of the blocker and right plots show their activity after injection of the blocker. First two sample cells (plots A.d and B.d) include

STAs with rhythmic oscillations with different phases (downward and upward respectively) . Both cells do not reflect light-stimulus driven response. After injection of the blocker the STA of cells with *downward STA* is abolished (figure 3.11.A.h), while for the second cell that has an upward STA only the oscillations are removed and a biphasic upward STA can be observed (figure 3.11.B.h). Figure 3.11.C illustrates the activity of a cell with response to light stimulus. The spike rates of the light-evoked activities (figure 3.11.C.d) show that the cell has an OFF preference to light stimulation. This cell reflects a downward biphaisc STA without rhythmic oscillations which is abolished after injection of the blocker (figure 3.11.C.h).

3.3.6 Clustering rd10 retina cells

The electrical activity of four rd10 retinas was recorded and 696 units were detected. Only units with significant electrical STA were included for clustering. Significance test was similar to chapter one (p-value<.0001), leaving 234 cells for final clustering. Since we do not expect the regular light-evoked activity of RGCs for degenerated retina, the preprocessing phase for removing noisy data was not performed and only cells with significant electrical STAs were included for analysis. Thus, we expect to see some clusters with noisy light-evoked activity. The results of wild-type clustering showed that the algorithm performs well in sorting noisy data into different clusters.

Similar to wild-type data, we extracted the gap statistics and adjusted mutual information to estimate the number of the clusters. Adjusted mutual information metrics peaked at 3, 12, and 13 for the combination of all stimuli, full-field flash, and chirp respectively (figure 3.12). Visual inspection of the clustered data revealed that consensus is higher for more than 5 clusters. Thus, we only consider the 12 and 13 as proper candidates for cluster number. By comparing the cluster overlap and ordered distance matrices for color and flash data and the fact that flash stimulus is more reliable for stimulation of the degenerated retina, we chose the cluster number reported from the flash stimulus for clustering. Figure 3.13 shows the t-SNE embeddings of the PSTHs for flash and chirp stimuli. The ON-OFF bias index is better separated for flash data compared to chirp (figure 3.13.B).

Figure 3.14, shows results of clustering based on the light-evoked activity before injection of the blocker. Except for cluster 8 that has ON preference, most clusters reflect OFF preference to full-field flash stimulus. Unlike wild-type retina for color stimulus, only green light causes some activity and stimulation of blue light does lead to any activity in rd10 RGCs. For clusters with higher signal to noise ratio (7, 11 and 12), the average of STAs show a biphasic downward deflection. Some clusters have STAs with rhythmic oscillation (clusters 3-5). After applying the blocker, On-bipolar cells are inhibited and only OFF activity can be observed (figure 3.14.E). Electrical STAs of most clusters are disrupted after the application of the blocker. This can be interpreted as the contribution of On-bipolar cells in the generation of the spikes elicited by the electrical stimulus.
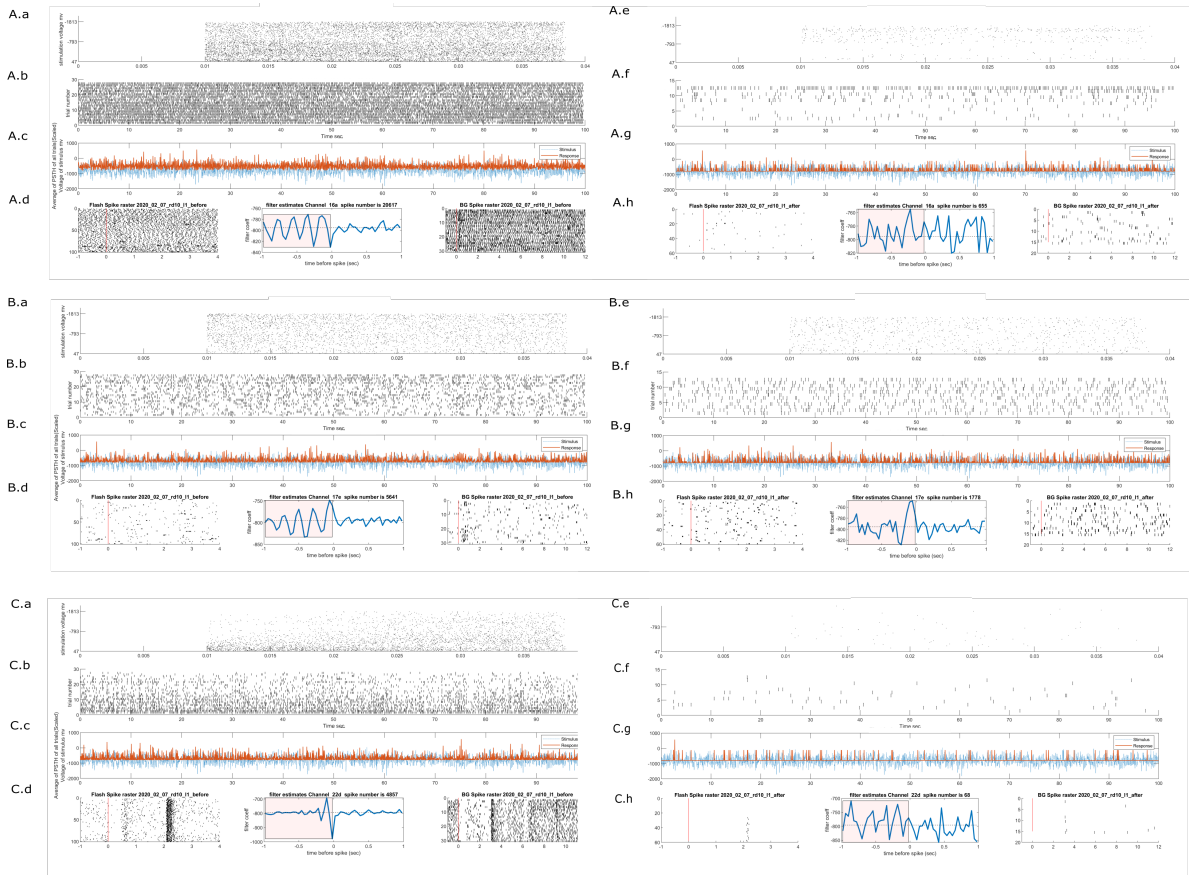
Figure 3.11: Comparing electrical profiles of three sample rd10 cell before and after injection of blocker. Left plots: activity before injection of blocker. Right plots: activity after injection of blocker. (A) Activity of a cell that does not respond to light stimulation with 5Hz electrical STA with negative phase. (A.a) Spike raster for each stimulation pulse with 40 ms periods. Data in the first 10ms is removed to exclude the effect of direct spikes in estimating STA. (A.b) spike raster shows the neuron's response to electrical stimulation for 100 sec interval. (A.c) Stimulus versus the average of PSTHs. Blue, electrical noise stimulus. Red, average of PSTHs over all trials. (A.d) Left, spike raster of full-field flash stimulus . Middle, electrical STA. right, spike raster of full-field color stimulus. (A.e, A.f, A.g , A,h) similar to (A.a, A.b, A.c, A,d) after injection of blocker. After applying blocker, the spiking activity is reduced and the STA is abolished. (B) activity of a sample neuron with rhythmic oscillation with positive STA phase. The plot order is the same as (A). Applying blocker removed the oscillations in STA but the two first peaks of STA are not removed. (C) Activity of a light sensitive neuron with biphasic STA. After applying blocker the spiking activity is reduced and the STA is abolished.

3.3.7 Clustering STAs of rd10 ganglion cells

To achieve a detailed overview of electrical input filters of rd10 retina we performed hierarchical clustering on z-scored STAs of rd10 data. To find the optimum cluster number, the gap statistics were computed for the time period of -1 to zero sec of STAs. The metric showed a peak at 23 (figure 3.12.H). Hierarchical clustering performed on STAs of 234 rd10 cells (figure 3.15). Averages of
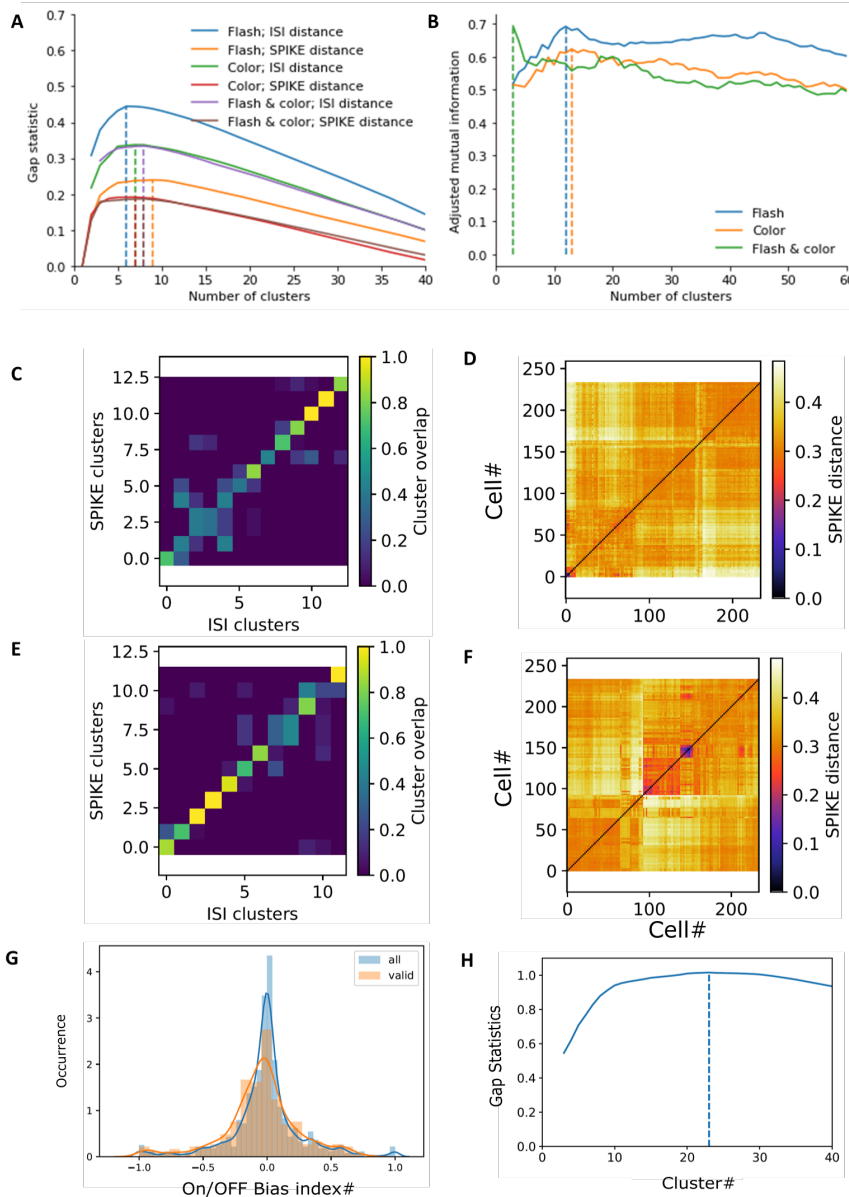
Figure 3.12: Comparison of gap statistics and mutual information for rd10 data. (A) Gap statistics for ISI and SPIKE metrics for different stimuli. (B) Adjusted mutual information for pairwise comparison between the ISI and SPIKE metric for different visual stimuli. (C) Cluster overlap after applying hierarchical clustering on ISI and SPIKE-distance of full field flash data with 12 clusters. (D) Distance matrix ordered by linkage for Spike-Distance of full field flash. (E) Cluster overlap after applying hierarchical clustering on ISI and SPIKE-distance of chirp data with 13 clusters. (F) Distance matrix ordered by linkage for Spike-Distance of chirp. (G) ON-OFF bias index of rd10 data. (H) Using gap statistics to find the optimum cluster number of e-STAs.
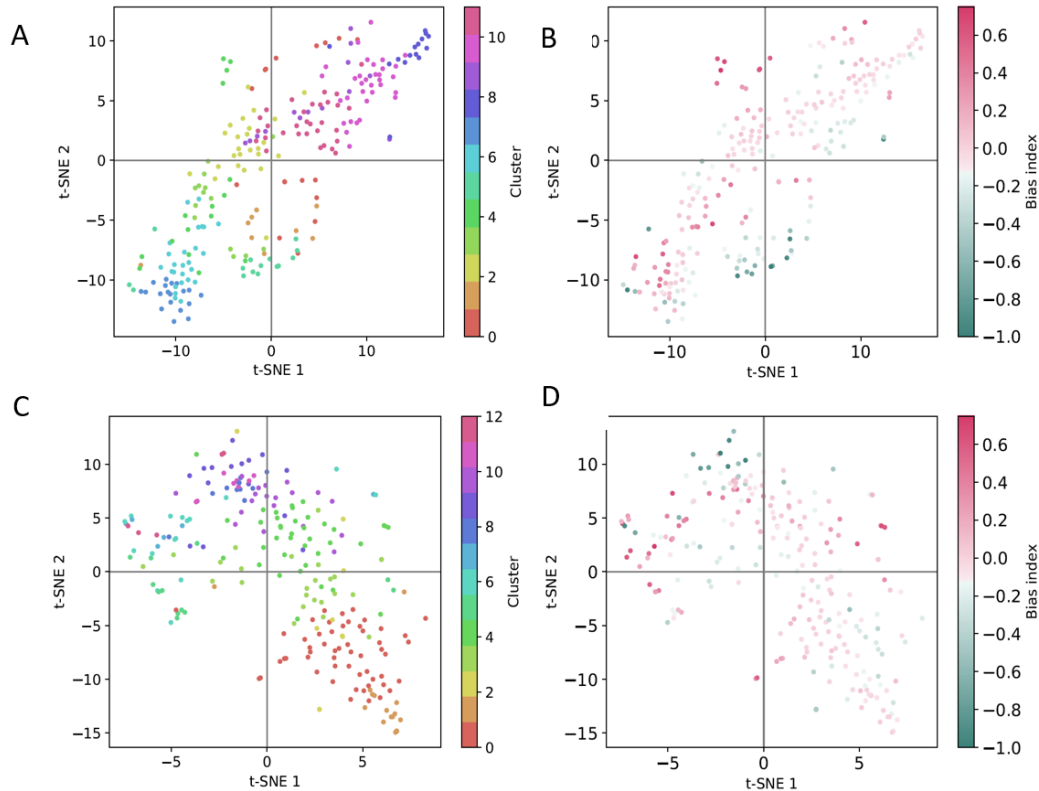
Figure 3.13: t-SNE plots of rd10 data. (A) t-SNE plot of flash PSTHs. Each point represents one unit. Colormap is the same as fig 32. (B) t-SNE plot of flash stimulus PSTHs. Units colored based on their ON-OFF bias index values. (C) similar to (A) for chirp stimulus. (D) similar to (B) for chirp stimulus.

all STAs in clusters 1 to 6 (the first branch of the hierarchical tree) have a positive deflection before time zero (*upward STA*). Except for cluster 2 which reflects a noisy visual-evoked response, all other 5 clusters reflect ON preference in response to the full field flash and color stimuli. Clusters 7-11 form another sub-branch. Most of the clusters in this branch reflect the OFF visual preference. By excluding cluster 9 because of its noisy response only cluster 8 shows ON preference to green light stimulus. For this group of cells the average of power spectrum is 4.32±0.61 Hz (figure 3.15.E) which is relatively smaller than the average of PSDs for STAs in the clusters 12-23 located in the third sub-branch that is 5.81±0.85 Hz. The common feature of the second and third branches is that they all reflect OFF visual preference. Although the patterns of visual response for most of these clusters were similar, a careful inspection of the visual activities revealed that there is a relation between the visual and electrical response of the cells. We observed that clusters with a stronger visual response (clusters 12-14 and 22-23) tend to have more biphasic STAs with less oscillations. Similar to wild-type retina here, we can also see the correspondence between the visual and electrical profiles of the recorded RGCs. All six
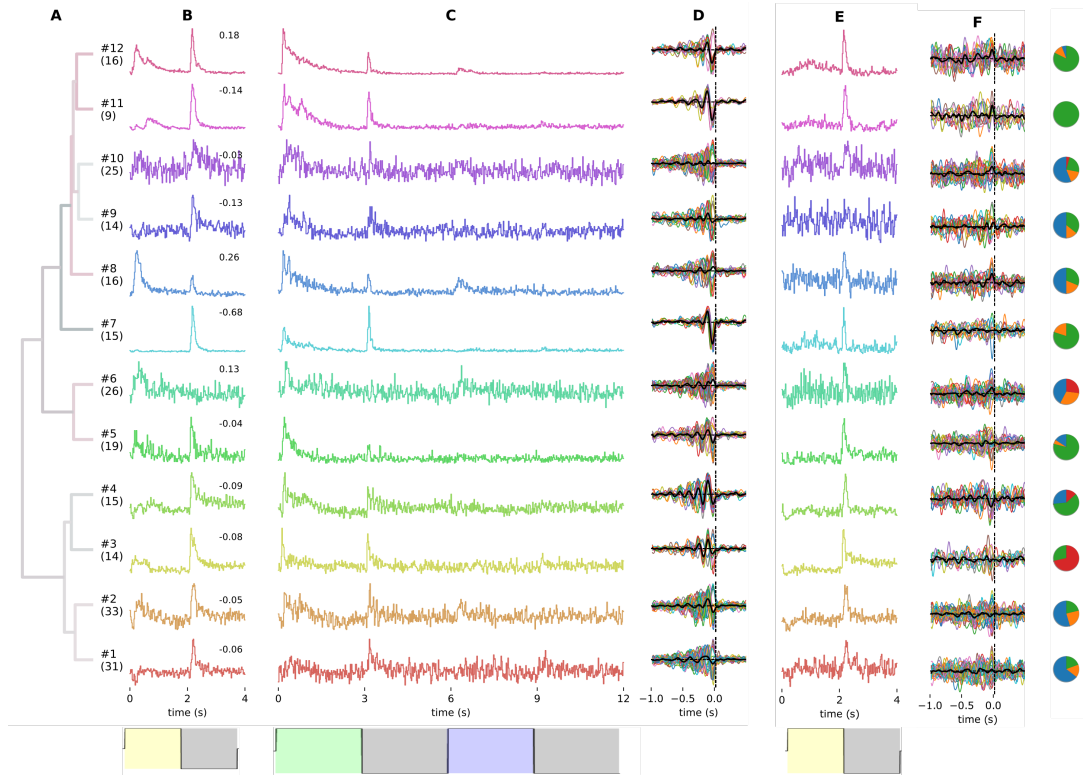
Figure 3.14: Hierarchical clustering of rd10 RGCs. (A) Dendrogram. (B) Response to full field flash stimulus. (C) Response to color stimulus. (D) Electrical STAs before injection of blocker. (E) Response to full field flash stimulus after injection of blocker. (D) Electrical STAs after injection of blocker. Pie charts show the proportion of the cells for each recording.

clusters with *upward STAs* (clusters 1-6) respond to stimulus onset of flash and color stimuli, while none of the clusters with *downward STA* (clusters 7-23) have the visual response only to stimulus onset. However, unlike wild-type STAs, in the rd10 retina for most clusters, we can see the STAs with rhythmic oscillations.

After injection of the blocker, the ON pathways are inhibited, and only Off activity can be observed (figure 3.15.G). For all clusters with *downward STAs* (clusters 7-23), the STAs are wiped out after injection of the blocker. However, in five of six clusters with *upward STA*, the rhythmic oscillations are eliminated after injection of the blocker but the average of STAs shows a positive peak (clusters 1, 3-6 figure 3.15.F). Results of power spectrum analysis show that these STAs have a frequency range of 1-5 Hz (figure 3.15.H). We found these results interesting, since they show, (i) ON and OFF cells have different electrical profiles, (ii) the underlying mechanism leads to generation of *upward STAs* implements a different pathway that cannot be shut down by AP4 blocker (group III metabotropic glutamate). This may explain the mechanism by which ON and OFF RGC types can be stimulated selectively.

To check the clustering quality, the t-SNE plot and projection of the STAs on three first
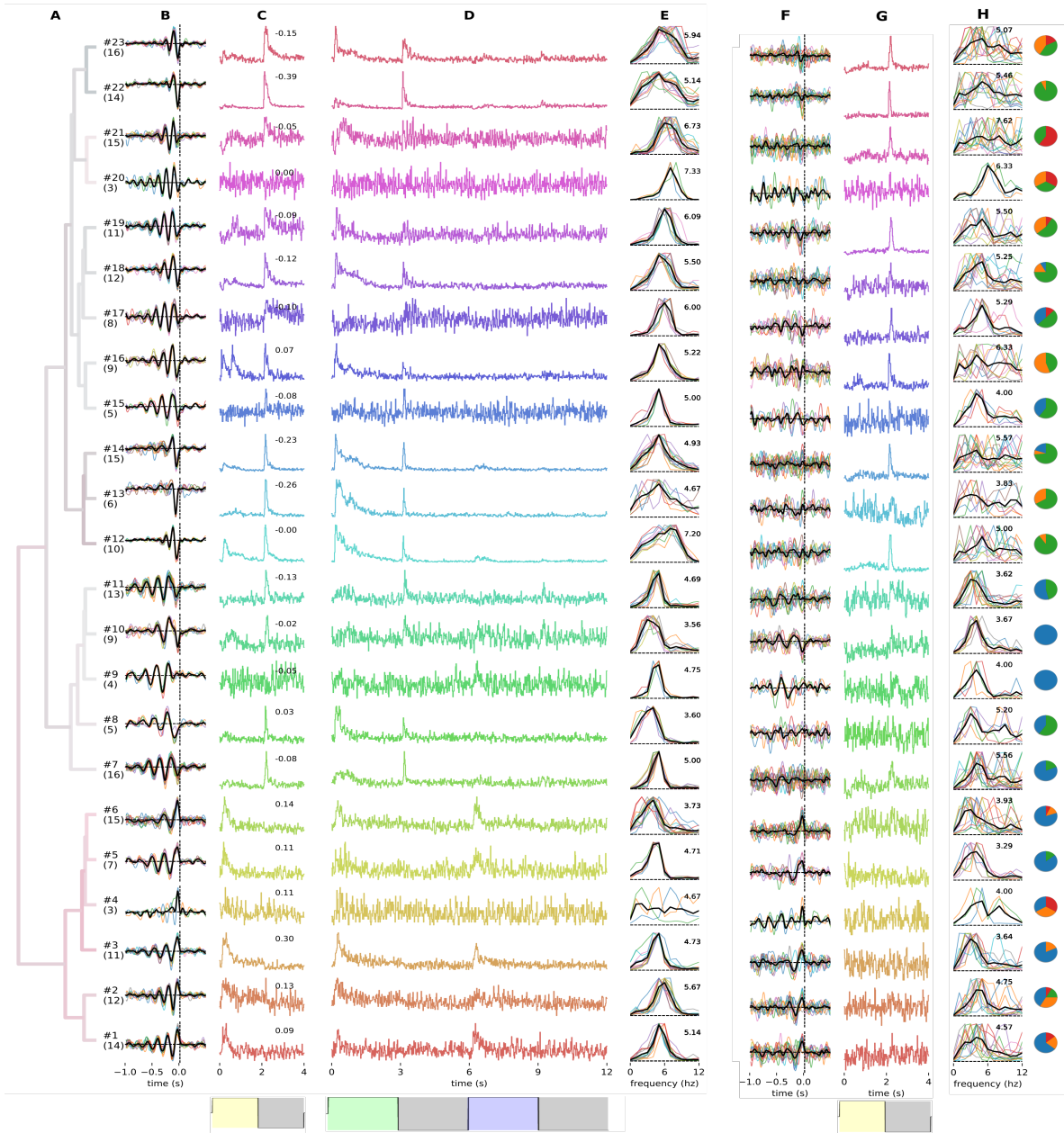
Figure 3.15: Hierarchical clustering of electrical input filters of rd10 retina. (A) Cluster dendrogram. (B) Clustered electrical input filters (STAs). First branch includes 6 clusters (clusters 1-6) of STAs with positive peaks. Second branch contains the rest of clusters with downward STAs (clusters 7-23). (C, D) PSTH of light-induced activity of Full field flash and color stimulus respectively. The visual response for all cells in the first 6 clusters reflect only ON preference while the visual response of clusters in the second branch is dominated by OFF cells. (E) Power spectrum of STAs for each cluster. (F) STAs after injection of the blocker. (G) Full-field flash response after injection of blocker. (H) Power spectrum of STAs after injection of blocker. Pie charts show the proportion of the neurons of each recording. Each color represents one retina.

Table 3.2: Power spectrum features of STAs for each cluster of rd10 data before and after (numbers in parentheses) injection of blocker. Columns from left to right: cluster number, frequency of peak of PSD, lower band frequency of 50% of PSD, upper band frequency of 50% of PSD, band width of the 50% of PSD.

$Cluster\#$	$Peak-freq(Hz)$	$f1_{50\%}(Hz)$	$f2_{50\%}(Hz)$	$BW(f2-f1)$
1	5.14 (4.57)	4.5 (2.79)	5.86 (6.5)	1.36 (3.71)
2	5.67 (4.75)	4.92 (3.42)	6.42 (6.33)	1.5 (2.92)
3	4.73 (3.64)	3.64 (2.45)	5.09 (4.64)	1.45 (2.18)
4	4.67 (4)	3.67 (3.33)	7.67 (7.33)	4 (4)
5	4.71 (3.29)	3.86 (2.71)	5 (4.29)	1.14 (11.57)
6	3.73 (3.93)	2.53 (2.43)	4.8 (5.93)	2.27 (3.5)
7	5 (5.56)	4.19 (3.31)	5.06 (7.56)	0.88 (4.25)
8	3.6 (5.2)	2.4 (2.6)	4 (6.6)	1.6 (4)
9	4.75 (4)	4.25 (3.25)	5 (5.75)	0.75 (2.5)
10	3.56 (3.67)	2.67 (3.11)	4.78 (4.78)	2.11 (1.67)
11	4.69 (3.62)	4.08 (2.62)	5.15 (5.62)	1.08 (3)
12	7.2 (5)	4.6 (3.3)	7.9 (8.3)	3.3 (5)
13	4.67 (3.83)	2.33 (2.83)	7.33 (8)	5 (5.17)
14	4.93 (5.57)	3.47 (2.23)	6 (8.71)	2.53 (6.36)
15	5 (4)	4.4 (2.6)	5.6 (7)	1.2 (4.4)
16	5.22 (6.33)	4.33 (3.78)	6 (8.56)	1.67 (4.78)
17	6 (5.29)	5.38 (4.57)	6.5 (6.71)	1.12 (2.14)
18	5.5 (5.25)	4.58 (3.08)	6.67 (6.92)	2.08 (3.83)
19	6.09 (5.5)	5.55 (3.4)	6.73 (7.8)	1.18 (0.67)
20	7.33 (6.33)	6.67 (5)	7.33 (8.67)	0.67 (3.67)
21	6.73 (7.62)	5.6 (3.69)	7.53 (9.15)	1.93 (5.46)
22	5.14 (5.46)	3.5 (2.92)	7 (8.62)	3.5 (5.69)
23	5.94 (5.07)	4.65 (3.64)	7.76 (8.14)	3.12 (4.5)
Median	**5(5,3)**	**4.2(3,11)**	**6(7)**	**1.63(4)**

principal components computed by the PCA method are shown in figure 3.16.

3.4 Discussion

A nonparametric hierarchical clustering paradigm using spike train distance metrics was used to classify RGCs based on either visual or electrical stimulation. The method is optimized for clustering the neurons that are stimulated simultaneously by the same stimulus. It can effectively assess the response behavior of RGCs with MEA [60, 64]. The validity of clustering was examined by looking at t-SNE plots. The method was able to sort noisy data into separate clusters and successfully cluster different patterns of light-induced activity.

The same Gaussian White noise as in chapter two was used for electrical stimulation. Along
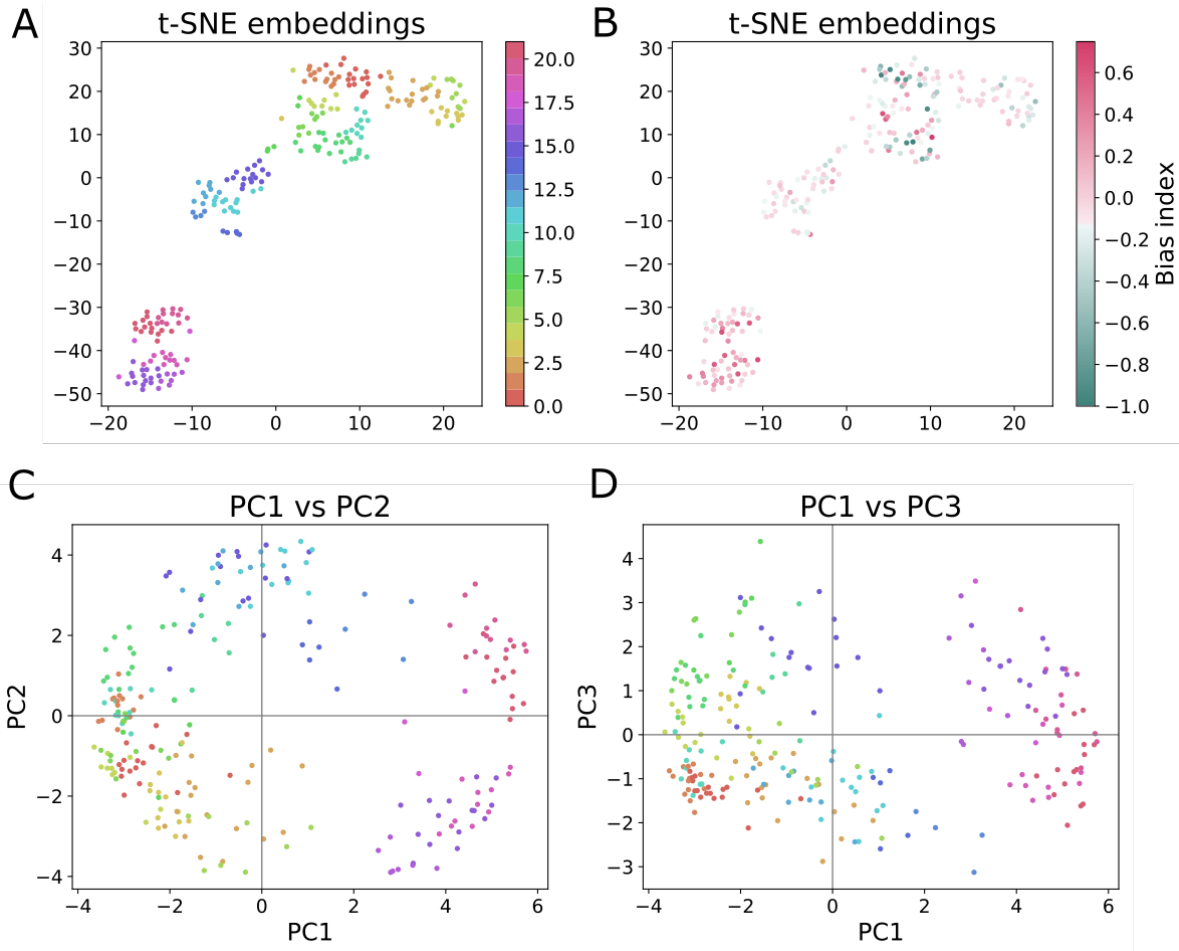
Figure 3.16: t-SNE plots and scatter plots of projection of STAs of rd10 data onto first, second and third principal components.

with previous reports[4, 35, 52–54] we found electrical Gaussian noise a useful tool for characterising the electrical properties of RGCs. Hierarchical clustering of light-evoked data of wild-type retina showed that for all 7 OFF clusters (clusters with the average of bias index <-0.5) had STAs with significant downward deflection (pval<.0001), Also 71% (5/7) of ON clusters (clusters with the average of bias index >0.5) had STAs with significant upward deflection. However, for On-OFF types we did not find specific STA shapes. A similar effect was reported by Sekhar et el [4]. They reported that across the population of 46 RGCs with ON, OFF and ON-OFF preference, STAs of ON and oFF cells reflect consistent upward and downward deflections whereas for ON-OFF cells both upward and downward STAs were observed. In our data we observed that for 83% of ON-OFF clusters (clusters with -0.5 <bias index <0.5) the Average of STA had significant deflection, from which 70% were STAs with significant deflection in negative peaks. However, we think the significant test on the average of STAs is not sufficient since by visual inspection we noticed that many of the ON-OFF clusters include a mixture of both upward and downward

STAs. Similar results were observed for the rd10 retina, with the difference that most of the STAs of the degenerated retina were modulated by rhythmic oscillations. In general, assessment of electrical profiles of different clusters for both healthy and degenerated retina revealed that different RGC types often have different electrical STA shapes.

In addition to clustering RGCs based on their visual-induced activity, we performed clustering based on the electrical profiles. Clustering electrical-induced responses gave us more information about the diversity of electrical STAs among all recorded RGCs types. STAs could be divided into upward and downward groups. Höfling et al.[53] reported similar STAs using hierarchical clustering. However, since they included direct response of RGCs for computing linear filters, the duration of reported STAs in their study was shorter(<20 ms). Inspection of the visual-induced activity of wild-type retina clusters based on their electrical STAs, revealed that all 7 clusters with *upward STAs* correspond to ON RGCs and one of the clusters with *downward STA* represents the activity of OFF RGCs. The other clusters with *downward STAs* showed a contribution of ON and OFF or ON-OFF RGCs in their visual-induced activity. Also, for the rd10 retina the diversity of STA profiles was higher than for wild-type retina owing to the rhythmic oscillations (figure 3.8).

Comparing the results of visual and electrical based clustering of degenerated retina (presented in figures 3.14 and 3.15) showed that the visual responses of rd10 retinas are less variable with electrical STA based clustering than with visually-based clustering. This is most evident in that there are 6 clusters with ON only visual responses for electrical STA-based clustering whereas all of these cells are blended into clusters with OFF responses in the flash-based clustering. Thus, for rd10 data, electrically based clustering does a better job than visual clustering of separating out different visual cell types. This is compelling evidence that visual and electrical response patterns are linked. Furthermore, we noticed that the ON clusters seem more likely to retain an electrical STA, even though the ON pathway is more perturbed by the blocker. From this, we can interpret that the underlying mechanism that leads to the generation of *upward STAs* is independent of Photoreceptor-On bipolar cells synaptic connection.

The origin of rhythmic oscillation of baseline activity in RGCs of mouse models with deficiency in the -subunit of phosphodiesterase, has been studied by several groups [74, 77, 78]. One theory is that these oscillations originate from the electrically-coupled network of AII amacrine cells and ON cone bipolar cells [77, 79]. By applying a blocker of ionotrophic glutamate receptors, Menzler et al [76] reported that electrically coupled interneurons lead to rhythmic oscillations in the rd1 retina. It is possible that interneurons like ACs play a role in retaining the upward STAs of On-RGCs, however it requires performing experiments including the application of Glycinergic and GABAergic synaptic blockers on ACs in either healthy or degenerated retina. We are uncertain about the mechanism that leads to disruption of downward STAs in OFF-RGCs after application of the blocker though. Since the blocker is supposed to inhibit On-bipolar cells pathways we expected to see the opposite effect. To shed more light on this matter we suggest

performing similar experiments on wild-type retina. We can hypothesise that Oscillations in rd10 retina are intrinsic to the ON circuit, and transferred to the off circuit by the AII ACs. Therefore by blocking excitatory drive to the ON circuits, we shut down oscillations in both ON and OFF circuits. It may explain why oscillations are lost in both types. But it does not explain why the OFF cell eSTAs completely disappear.

Another interesting finding was the range of frequency selectivity in the electrical STAs of healthy and degenerated retina. We observed that STAs of the rd10 retina are more frequency selective compared to wild-type retina. The median of peak frequency and bandwidth at 50% of peak were respectively 3.11 Hz and 2.63 Hz in wild-type retina whereas these values were 5 Hz and 1,63 Hz in rd10 retina. Matlab ranksum test with alpha = 0.01 showed significant difference between peaks and bandwidths of healthy and degenerated retina (pvalue = 0.0013 and 0.0052 respectively). A relatively similar frequency range (6.5 Hz) was reported previously in rd10 spontaneous activity [75]. We also observed a significant difference between the PSD peaks of upward (clusters 1-6 figure 3.15) and downward (clusters 7-23) STAs in rd10 retinas (pval=0.0063, ranksum test). Median of mentioned PSD peaks was 6±0.8 Hz for upward STAs and 4.7±0.8 Hz for downward STAs. The statistical test however, did not show a significant difference in frequency selectivity of upward and downward STAs. This is good evidence showing that ON and OFF cells in degenerated retina are prone to be stimulated selectively using different frequencies. It is also in line with the work of Twyford et al[49] on rabbit retina who showed RGCs types respond differently depending on the frequency of stimulation.

Application of a blocker increased the bandwidth significantly from 1.6 Hz up to 4 Hz (pval=1.9195e-05, ranksum test) but it did not change frequency peaks significantly (4.87 Hz). Similar results are observed by performing statistical tests separately for upward and downward STAs .

Also, comparing the wild-type and degenerated retina clustered, revealed there were many fewer ON-OFF clusters in the rd10 data when sorted by electrical STA (two out of 23), whereas when the wild-type is sorted by electrical STA, 50% of clusters are ON-OFF. We think this makes clear that the ON-OFF type is disrupted by degeneration. This is an example of application of electrical stimulation in understanding the retinal circuits, something that was not detected by visual responses.

CONCLUSION

In an effort to find a better alternative for classical supra threshold pulsatile electrical stimulation of the retina, We performed subthreshold noise stimulation to deepen our understanding about the underlying mechanism that leads to indirect activation of RGCs. The concept of electrical noise stimulation has been tested by different groups worldwide with either epiretinal and subretinal configurations [52, 53, 80]. In our recent perspective paper [81](see appendix) we proposed a computational model based on noise correlation analysis to address the possibility of selective activation by simulating the response of different retinal cell classes (photoreceptor, bipolar cell, and RGC) to electrical noise stimulation. In this study we applied the same stimulation strategy on real tissue. We performed epiretinal subthreshold noise stimulation to deepen our understanding of the underlying mechanism that leads to indirect activation of RGCs. Since white Gaussian noise includes a wide range of frequencies it helped us to probe a larger space of stimulation feature domain. By using noise correlation analysis, we were able to extract the linear input filters of the recorded RGCs.

We tried different clustering frameworks to classify the recorded RGCs based on their visual-induced activity. This helped us to characterize the electrical profiles of classified RGCs. In the second chapter, we introduced a method to classify the recorded RGCs to one of the 32 RGS types defined by Baden et al. We used the OGB kernel estimated from the concurrent recording of calcium and electrophysiological data[16]. By convolving our spiking data with this kernel we estimated the so-called pseudo-calcium traces. This allowed us to convert discrete spiking data into continuous signals matching better with real calcium traces. After projecting the pseudocalcium traces into the lower dimension using the sPCA feature space of the reference data set we computed the distance matrix of two datasets by computing the Euclidian distance of each cell to all clusters. Finally, we assigned each cell to the most similar cluster. Although

the algorithm could detect most of the reference clusters, a subset of clusters was missed. A quadruple increase of the sample size however did not change the results significantly. Therefore, we speculated that this was a shortcoming of the clustering method in converting spiking data to pseudocalcium data, mainly because of the missing subthreshold synaptic activity that cannot be captured in spiking data. After assigning the RGCs to one of the defined reference clusters we were able to probe the electrical property of each cell type. We observed that for many OFF sub-types the electrical STAs had a negative peak whereas for some of ON sub-types the electrical STAs contained a positive peak. These results confirmed the previous work of Sekhar et al[4]. denoting ON and OFF cells have the electrical profiles corresponding with their visual counterparts. One of the aims of this study was to find distinct electrical STAs within ON, OFF, and ON-OFF. Although our results showed that findings of Sekhar study are reproducible, current data hardly support strong electrical STA differences within the 3 coarse RGC types. However, Since the classification results were not complete, we decided to implement a different clustering framework based on the ISI distance.

In the third chapter, we reported the results of a new clustering framework. We used two metrics called ISI and SPIKE distance to measure (dis)similarity across different pairs of spike trains. These measures were used by Jouty et al. [64]. and have been shown to be effective for clustering MEA recordings of RGCs. We used the RGC clustering toolbox developed by Jouty et al. to cluster the RGCs based on the computed SPIKE distance matrix. Clustering was performed for wild-type and rd10 retina separately. For wild-type data, clustering yielded 37 clusters which were close to more than 32 clusters numbers defined by Baden et al[16]. Although some of the clusters could be merged or removed, many of them reflect the diverse response properties of RGCs. Since our clustering was merely based on extracted electrophysiological features there was the possibility that some clusters include the activity of spiking amacrine cells. Also some clusters might have been split into two or more clusters if we had the information about the soma size of the cells. Assessment of the electrical STAs of each cluster revealed a clear difference in electrical profiles of many ON and OFF sub-types. Again, we observed that electrical clusters of many OFF cells have *downward* deflection whereas electrical STAs of some On clusters had *upward* deflection. For most of ON-OFF clusters we did not find any specific electrical STA. One reason for that is probably due to the fact that some of these clusters consist of the combination of ON and OFF cells and their electrical STAs cancel each other out after averaging. The similar results had been observed in chapter two by using a different clustering framework. This consistency between the results of two different clustering paradigms shows that our hypothesis is robust against changing the method and reflects the reproducibility of results.

In addition to clustering the light-evoked activity of RGCs, we carried out the clustering for electrical STAs by which 15 different shapes of electrical STAs were detected. Evaluation of the visual activity of corresponding clusters showed that STAs with a positive peak can be produced only by ON RGC sub-types while OFF cells always contribute to the generation of STAs with

negative peaks.

In rd10 data, we observed that clustering the visual-evoked activity of rd10 RGCs yields 12 clusters, most of them reflecting OFF preference. One of the main differences between rd10 STAs and wild-type retina was the rhythmic oscillations. We observed that these oscillations are influenced by the electrical stimulation and their onset can be synchronised with stimulus. However,the phase of the oscillations was not a function of stimulus and depended on the retinal pathways involved in generation of the signals. We showed that upward STA clusters (positive phase) correspond to ON cells and downward STA clusters (negative phase) correspond to OFF ,ON-OFF or combination of ON and OFF cells. Another feature of the rd10 STAs. that was related to the intrinsic property of the degenerated retina, is that they were highly frequency selective with different frequency preference for upward and downward STAs. From these findings we can conclude that the frequency of stimulation and the phase of stimulus play important roles in preferential activation of RGCs in the degenerated retina.

In addition, probing the electrical STAs of degenerated retina showed that for most of the clusters the electrical STAs with negative peak were disrupted after application of a blocker, whereas despite our expectation, the clusters with *upward STAs* corresponding to ON clusters lose the visual response after drugs and retain their STAs. This was evidence that On-bipolar cells' pathways incorporate in the generation of *downward STAs*. From these results we inferred that sources of spiking activities that lead to the generation of *upward STAs* and *downward STAs* may originate from different retinal pathways. One explanation for that might be the effect of AII amacrine cells. The activity of On-RGCs is influenced through AII amacrine cells making electrical synapses at gap junctions to ON cone bipolar cells, whereas OFF-RGCs receive chemical synaptic input from the AII amacrine cells [77, 82, 83].

Furthermore, we noticed that clustering the degenerated retina cells based on electrical STAs gives us information about the visual properties of the ON and OFF cells that were not detectable by visual based clustering. We found these results notable from this perspective that electrical stimulation can teach us something about the retina beyond its application in retinal prosthetics, the information that was not detected through visual stimulation.

The correspondence between the electrical input filters of two major ON and OFF RGC types with their visual activity in healthy and degenerated retina is evidence of the possibility to preferentially activate ON and OFF pathways in the retina. Furthermore, the diversity of STA patterns in *upward STAs* and *downward STAs* can be regarded as a clue that our underlying goal of engineering an electrical stimulus to selectively activate different ON and OFF sub-types such as transient and sustained cells is probably achievable. However, because our approach had some drawbacks such as: (i) lack of precise approach for controlling location of stimulation electrode and, (ii) inability to capture the information about cells morphology, we think more elaborate experiments providing multi-modal data such as morphological features of each cell are required to make a strong argument on that matter.

In summary, we found the Gaussian noise stimulation as a fruitful approach to extract the linear filter of different cell types. Furthermore, applying hierarchical clustering on spike distance based measures of RGC responses was successful in separating different cell types. Our suggestions to achieve more trustworthy data for future studies are as follows:

- Implement high resolution microscopy with spatial resolution of a single cell to capture RGCs morphology and the layer in which they are located. This data can give us useful information about the alpha cells and spiking amacrine cells that can not be distinguished from other cells in physiological clustering. Furthermore, On-OFF RGCs have shown to be detectable from their bistratified dendritic arborizations in the inner plexiform layer (IPL) [77]. Having such information about the morphology of recorded cells can also help us to figure out why ON-OFF clusters did not reflect significant STA. Another challenge would be to associate the RGC spike trains with one of the imaged cells. because, many cells are near each electrode and each electrode can record from multiple cells. To avoid this issue, using patch-clamp recording or implementing very robust spike sorting algorithms is recommended.

- Implement filtered white Gaussian noise for electrical stimulation, to stimulate the retina tissue in an optimal frequency range. This method has been proposed in our recent perspective [81] and tested by Höfling et al [53]. They observed linear filters originating from direct RGCs responses of mouse retina.

- Apply different blockers for each experiment to precisely assess the effect of each retinal pathway in generation of STAs. We have STAs that seem to reflect both PR- and bipolar cell-mediated indirect stimulation of RGCs. Using blockers that suppress the activity of PR and bipolar cells separately can help us to tease these different mechanisms out from each other.

- Implement high resolution MEA for recording electrical activity. With this type of recording we can have access to the electrical activity of one cell in different channels with high spatial resolution. This allows us to inspect the electrical activity of cells at different areas such as axon and soma which provides more information about the spatio-temporal features of input filters.

- Perform similar experiments by patch-clamp recording to compare the results of intracellular and extracellular recordings. One advantage of this method is that the recorded data do not include spiking activity of neighboring cells.

- Perform sub-retinal stimulation by using a separate electrode as a stimulation electrode. In the ideal case the electrode can be controlled by a micromanipulator under a microscope to fix the distance between electrode and the tissue. This will enable us to stimulate the

retina from different regions and see its effect in generation of electrical STAs. Alongside with using different blockers this technique can be the solution to distinguish STAs of PR- and bipolar cell-mediated indirect activity. Furthermore, one of the disadvantages of MEA recording is that the impedance between electrode and tissue can be different from one experiment to another because of the electrode distance and some other parameters. Keeping the electrode distance constant over different experiments can help increase the homogeneity of data across different recordings.

- Apply sparse visual noise to extract the visual STA of RGCs. With our custom visual noise stimuli we were not able to extract the visual STAs of most of the RGCs. It has been reported that sparse-noise has some advantages in estimating the receptive field of different RGC types [84].

- Quantify electrical input filters by providing detailed information about the latency and duration of STAs of each cluster. This helps us to assess the diversity of electrical STAs within ON and OFF types.

- Perform pharmacological manipulations on wild-type retina. We suggest using Glycinergic and GABAergic blockers to assess the influence of ACs interneurons on upward and downward STAs.

BIBLIOGRAPHY

[1] Rupert RA Bourne, Seth R Flaxman, Tasanee Braithwaite, Maria V Cicinelli, Aditi Das, Jost B Jonas, Jill Keeffe, John H Kempen, Janet Leasher, Hans Limburg, et al.
Magnitude, temporal trends, and projections of the global prevalence of blindness and distance and near vision impairment: a systematic review and meta-analysis.
The Lancet Global Health, 5(9):e888–e897, 2017.

[2] Eberhart Zrenner.
Will retinal implants restore vision?
Science, 295(5557):1022–1025, 2002.

[3] Alexander Farnum and Galit Pelled.
New vision for visual prostheses.
Frontiers in Neuroscience, 14:36, 2020.

[4] S Sekhar, A Jalligampala, E Zrenner, and DL Rathbun.
Correspondence between visual and electrical input filters of on and off mouse retinal ganglion cells.
Journal of neural engineering, 14(4):046017, 2017.

[5] S Sekhar, A Jalligampala, E Zrenner, and DL Rathbun.
Tickling the retina: integration of subthreshold electrical pulses can activate retinal neurons.
Journal of neural engineering, 13(4):046004, 2016.

[6] Helga Kolb.
Simple anatomy of the retina by helga kolb.
Webvision: The Organization of the Retina and Visual System, 2011.

[7] Helga Kolb.
Photoreceptors by helga kolb, 2013.

[8] Thomas Euler, Silke Haverkamp, Timm Schubert, and Tom Baden.
Retinal bipolar cells: elementary building blocks of vision.
Nature Reviews Neuroscience, 15(8):507–519, 2014.

[9] Trevor D Lamb.
     Why rods and cones?
     Eye, 30(2):179–185, 2016.

[10] Ido Perlman.
     S-potentials and horizontal cells by ido perlman, helga kolb and ralph nelson.

[11] H Kolb, E Fernandez, and R Nelson.
     Roles of amacrine cells–webvision: The organization of the retina and visual system.
     1995.

[12] Shelley I Fried, Thomas A Münch, and Frank S Werblin.
     Mechanisms and circuitry underlying directional selectivity in the retina.
     Nature, 420(6914):411–414, 2002.

[13] Ralph Nelson.
     Ganglion cell physiology by ralph nelson, 2007.

[14] Haldan Keffer Hartline.
     The response of single optic nerve fibers of the vertebrate eye to illumination of the retina.
     American Journal of Physiology-Legacy Content, 121(2):400–415, 1938.

[15] Stephen W Kuffler.
     Discharge patterns and functional organization of mammalian retina.
     Journal of neurophysiology, 16(1):37–68, 1953.

[16] Tom Baden, Philipp Berens, Katrin Franke, Miroslav Román Rosón, Matthias Bethge, and
     Thomas Euler.
     The functional diversity of retinal ganglion cells in the mouse.
     Nature, 529(7586):345–350, 2016.

[17] Jennifer R Evans and John G Lawrenson.
     Antioxidant vitamin and mineral supplements for slowing the progression of age-related
     macular degeneration.
     Cochrane Database of Systematic Reviews, (7), 2017.

[18] Christian Hamel.
     Retinitis pigmentosa.
     Orphanet journal of rare diseases, 1(1):1–12, 2006.

[19] Henri Lorach, Olivier Marre, José-Alain Sahel, Ryad Benosman, and Serge Picaud.
     Neural stimulation for visual rehabilitation: advances and challenges.
     Journal of Physiology-Paris, 107(5):421–431, 2013.

[20] Marc Peschanski and Christian Jorgensen.
Stem cell transplantation for long-term treatment.
https://www.inserm.fr/en/health-information/health-and-research-from-z/cell-therapy.

[21] Botond Roska and Jose-Alain Sahel.
Restoring vision.
Nature, 557(7705):359–367, 2018.

[22] Michelle E McClements, Federica Staurenghi, Robert E MacLaren, and Jasmina Cehajic-Kapetanovic.
Optogenetic gene therapy for the degenerate retina: Recent advances.
Frontiers in Neuroscience, 14:1187, 2020.

[23] Anne Louise Askou, Thomas Stax Jakobsen, and Thomas J Corydon.
Retinal gene therapy: an eye-opener of the 21st century.
Gene Therapy, pages 1–8, 2020.

[24] José-Alain Sahel and Botond Roska.
Gene therapy for blindness.
Annual review of neuroscience, 36:467–488, 2013.

[25] Anding Bi, Jinjuan Cui, Yu-Ping Ma, Elena Olshevskaya, Mingliang Pu, Alexander M Dizhoor, and Zhuo-Hua Pan.
Ectopic expression of a microbial-type rhodopsin restores visual responses in mice with photoreceptor degeneration.
Neuron, 50(1):23–33, 2006.

[26] Eberhart Zrenner, Karl Ulrich Bartz-Schmidt, Heval Benav, Dorothea Besch, Anna Bruckmann, Veit-Peter Gabel, Florian Gekeler, Udo Greppmaier, Alex Harscher, Steffen Kibbel, et al.
Subretinal electronic chips allow blind patients to read letters and combine them to words.
Proceedings of the Royal Society B: Biological Sciences, 278(1711):1489–1497, 2011.

[27] Lan Yue, James D Weiland, Botond Roska, and Mark S Humayun.
Retinal stimulation strategies to restore vision: Fundamentals and systems.
Progress in retinal and eye research, 53:21–47, 2016.

[28] Philip L Gildenberg.
History of electrical neuromodulation for chronic pain, 2006.

[29] Gustav Fritsch.
About the electrical excitability of the cerebrum.
Arch, anat. Physiol. Knowledge Med., 37:300–332, 1870.

[30] James P Morgan.
The first reported case of electrical stimulation of the human brain.
Journal of the history of medicine and allied sciences, 37(1):51–64, 1982.

[31] Giles S Brindley and Walpole S Lewin.
The sensations produced by electrical stimulation of the visual cortex.
The Journal of physiology, 196(2):479–493, 1968.

[32] TASSICKER GE.
Preliminary report on a retinal stimulator.
The British journal of physiological optics, 13(2):102–105, 1956.

[33] Mark S Humayun, Eugene de Juan Jr, James D Weiland, Gislin Dagnelie, Steve Katona,
Robert Greenberg, and Satoshi Suzuki.
Pattern electrical stimulation of the human retina.
Vision research, 39(15):2569–2576, 1999.

[34] Sébastien Joucla and Blaise Yvert.
Modeling extracellular electrical neural stimulation: from basic understanding to mea-based
applications.
Journal of Physiology-Paris, 106(3-4):146–158, 2012.

[35] David Boinagrov, Susanne Pangratz-Fuehrer, Georges Goetz, and Daniel Palanker.
Selectivity of direct and network-mediated stimulation of the retinal ganglion cells with
epi-, sub-and intraretinal electrodes.
Journal of neural engineering, 11(2):026008, 2014.

[36] Shelley I Fried, Hain-Ann Hsueh, and Frank S Werblin.
A method for generating precise temporal patterns of retinal spiking using prosthetic
stimulation.
Journal of neurophysiology, 95(2):970–978, 2006.

[37] Joseph F Rizzo, John Wyatt, John Loewenstein, Shawn Kelly, and Doug Shire.
Perceptual efficacy of electrical stimulation of human retina with a microelectrode array
during short-term surgical trials.
Investigative ophthalmology & visual science, 44(12):5362–5369, 2003.

[38] Katarina Stingl, Karl Ulrich Bartz-Schmidt, Dorothea Besch, Angelika Braun, Anna Bruck-
mann, Florian Gekeler, Udo Greppmaier, Stephanie Hipp, Gernot Hörtdörfer, Christoph
Kernstock, et al.
Artificial vision with wirelessly powered subretinal electronic implant alpha-ims.
Proceedings of the Royal Society B: Biological Sciences, 280(1757):20130077, 2013.

[39] Mark S Humayun, James D Weiland, Gildo Y Fujii, Robert Greenberg, Richard Williamson, Jim Little, Brian Mech, Valerie Cimmarusti, Gretchen Van Boemel, Gislin Dagnelie, et al.
Visual perception in a blind subject with a chronic microelectronic retinal prosthesis.
Vision research, 43(24):2573–2581, 2003.

[40] Lyndon Da Cruz, Brian F Coley, Jessy Dorn, Francesco Merlini, Eugene Filley, Punita Christopher, Fred K Chen, Varalakshmi Wuyyuru, Jose Sahel, Paulo Stanga, et al.
The argus ii epiretinal prosthesis system allows letter and word reading and long-term function in patients with profound vision loss.
British Journal of Ophthalmology, 97(5):632–636, 2013.

[41] Maesoon Im and Shelley I Fried.
Temporal properties of network-mediated responses to repetitive stimuli are dependent upon retinal ganglion cell type.
Journal of neural engineering, 13(2):025002, 2016.

[42] Archana Jalligampala, Sudarshan Sekhar, Eberhart Zrenner, and Daniel L Rathbun.
Optimal voltage stimulation parameters for network-mediated responses in wild type and rd10 mouse retinal ganglion cells.
Journal of neural engineering, 14(2):026004, 2017.

[43] Yong Sook Goo, Jang Hee Ye, Seokyoung Lee, Yoonkey Nam, Sang Baek Ryu, and Kyung Hwan Kim.
Retinal ganglion cell responses to voltage and current stimulation in wild-type and rd1 mouse retinas.
Journal of neural engineering, 8(3):035003, 2011.

[44] Seung Woo Lee, Krishnan Thyagarajan, and Shelley I Fried.
Micro-coil design influences the spatial extent of responses to intracortical magnetic stimulation.
IEEE Transactions on Biomedical Engineering, 66(6):1680–1694, 2018.

[45] James D Weiland, Steven T Walston, and Mark S Humayun.
Electrical stimulation of the retina to produce artificial vision.
Annual review of vision science, 2:273–294, 2016.

[46] David Tsai, John W Morley, Gregg J Suaning, and Nigel H Lovell.
Survey of electrically evoked responses in the retina-stimulus preferences and oscillation among neurons.
Scientific reports, 7(1):1–14, 2017.

[47] Daniel K Freeman, Donald K Eddington, Joseph F Rizzo III, and Shelley I Fried.
Selective activation of neuronal targets with sinusoidal electric stimulation.
Journal of neurophysiology, 104(5):2778–2791, 2010.

[48] Tianruo Guo, Chih Yu Yang, David Tsai, Madhuvanthi Muralidharan, Gregg J Suaning,
John W Morley, Socrates Dokos, and Nigel H Lovell.
Closed-loop efficient searching of optimal electrical stimulation parameters for preferential
excitation of retinal ganglion cells.
Frontiers in neuroscience, 12:168, 2018.

[49] Perry Twyford and Shelley Fried.
The retinal response to sinusoidal electrical stimulation.
IEEE transactions on neural systems and rehabilitation engineering, 24(4):413–423, 2015.

[50] Perry Twyford, Changsi Cai, and Shelley Fried.
Differential responses to high-frequency electrical stimulation in on and off retinal ganglion
cells.
Journal of neural engineering, 11(2):025001, 2014.

[51] Maesoon Im, Paul Werginz, and Shelley I Fried.
Electric stimulus duration alters network-mediated responses depending on retinal ganglion
cell type.
Journal of neural engineering, 15(3):036010, 2018.

[52] Elton Ho, Alexander Shmakov, and Daniel Palanker.
Decoding network-mediated retinal response to electrical stimulation: implications for
fidelity of prosthetic vision.
Journal of Neural Engineering, 2020.

[53] Larissa Höfling, Jonathan Oesterle, Philipp Berens, and Günther Zeck.
Probing and predicting ganglion cell responses to smooth electrical stimulation in healthy
and blind mouse retina.
Scientific reports, 10(1):1–20, 2020.

[54] Elton Ho, Richard Smith, Georges Goetz, Xin Lei, Ludwig Galambos, Theodore I Kamins,
James Harris, Keith Mathieson, Daniel Palanker, and Alexander Sher.
Spatiotemporal characteristics of retinal response to network-mediated photovoltaic stimu-
lation.
Journal of neurophysiology, 119(2):389–400, 2018.

[55] Sudarshan Sekhar.
*Characterization of Retinal Ganglion Cell Responses to Electrical Stimulation Using White
Noise*.

PhD thesis, Universität Tübingen, 2020.

[56] Helga Kolb.
Morphology and circuitry of ganglion cells.
2011.

[57] Frank S Werblin and John E Dowling.
Organization of the retina of the mudpuppy, necturus maculosus. ii. intracellular recording.
Journal of neurophysiology, 32(3):339–355, 1969.

[58] Stephen M Carcieri, Adam L Jacobs, and Sheila Nirenberg.
Classification of retinal ganglion cells: a statistical approach.
Journal of neurophysiology, 90(3):1704–1713, 2003.

[59] Ronen Segev, Jason Puchalla, and Michael J Berry.
Functional organization of ganglion cells in the salamander retina.
Journal of neurophysiology, 95(4):2277–2292, 2006.

[60] Günther M Zeck and Richard H Masland.
Spike train signatures of retinal ganglion cell types.
European Journal of Neuroscience, 26(2):367–380, 2007.

[61] Karl Farrow and Richard H Masland.
Physiological clustering of visual channels in the mouse retina.
Journal of neurophysiology, 105(4):1516–1530, 2011.

[62] Zohreh Hosseinzadeh, Archana Jalligampala, Eberhart Zrenner, and Daniel Lleweylln Rathbun.
The spatial extent of epiretinal electrical stimulation in the healthy mouse retina.
Neurosignals, 25(1):15–25, 2017.

[63] EJ Chichilnisky.
A simple white noise analysis of neuronal light responses.
Network: Computation in Neural Systems, 12(2):199–213, 2001.

[64] Jonathan Jouty, Gerrit Hilgen, Evelyne Sernagor, and Matthias H Hennig.
Non-parametric physiological classification of retinal ganglion cells in the mouse retina.
Frontiers in Cellular Neuroscience, 12:481, 2018.

[65] Thomas Kreuz, Julie S Haas, Alice Morelli, Henry DI Abarbanel, and Antonio Politi.
Measuring spike train synchrony.
Journal of neuroscience methods, 165(1):151–161, 2007.

[66] Thomas Kreuz, Daniel Chicharro, Conor Houghton, Ralph G Andrzejak, and Florian Mor-
mann.
Monitoring spike train synchrony.
Journal of neurophysiology, 109(5):1457–1472, 2013.

[67] Thomas Kreuz, Daniel Chicharro, Martin Greschner, and Ralph G Andrzejak.
Time-resolved and time-scale adaptive measures of spike train synchrony.
Journal of neuroscience methods, 195(1):92–106, 2011.

[68] Robert Tibshirani, Guenther Walther, and Trevor Hastie.
Estimating the number of clusters in a data set via the gap statistic.
Journal of the Royal Statistical Society: Series B (Statistical Methodology), 63(2):411–423,
2001.

[69] Nguyen Xuan Vinh, Julien Epps, and James Bailey.
Information theoretic measures for clusterings comparison: Variants, properties, normaliza-
tion and correction for chance.
The Journal of Machine Learning Research, 11:2837–2854, 2010.

[70] Geoffrey Hinton and Sam T Roweis.
Stochastic neighbor embedding.
In *NIPS*, volume 15, pages 833–840. Citeseer, 2002.

[71] Peter Welch.
The use of fast fourier transform for the estimation of power spectra: a method based on
time averaging over short, modified periodograms.
IEEE Transactions on audio and electroacoustics, 15(2):70–73, 1967.

[72] Malcolm M Slaughter and Robert F Miller.
2-amino-4-phosphonobutyric acid: a new pharmacological tool for retina research.
Science, 211(4478):182–185, 1981.

[73] Yong Sook Goo, Kun No Ahn, Yeong Jun Song, Su Heok Ahn, Seung Kee Han, Sang Baek
Ryu, and Kyung Hwan Kim.
Spontaneous oscillatory rhythm in retinal activities of two retinal degeneration (rd1 and
rd10) mice.
*The Korean journal of physiology & pharmacology: official journal of the Korean Physiological
Society and the Korean Society of Pharmacology*, 15(6):415, 2011.

[74] Sonia Biswas, Christine Haselier, Anja Mataruga, Gabriele Thumann, Peter Walter, and
Frank Müller.
Pharmacological analysis of intrinsic neuronal oscillations in rd10 retina.
PloS one, 9(6):e99075, 2014.

[75] Jacob Menzler, Lakshmi Channappa, and Guenther Zeck.
Rhythmic ganglion cell activity in bleached and blind adult mouse retinas.
PloS one, 9(8):e106047, 2014.

[76] Jacob Menzler and Günther Zeck.
Network oscillations in rod-degenerated mouse retinas.
Journal of Neuroscience, 31(6):2280–2291, 2011.

[77] Joanna Borowska, Stuart Trenholm, and Gautam B Awatramani.
An intrinsic neural oscillator in the degenerating mouse retina.
Journal of Neuroscience, 31(13):5000–5012, 2011.

[78] Steven F Stasheff, Malini Shankar, and Michael P Andrews.
Developmental time course distinguishes changes in spontaneous and light-evoked retinal
ganglion cell activity in rd1 and rd10 mice.
Journal of neurophysiology, 105(6):3002–3009, 2011.

[79] Yong Sook Goo, Dae Jin Park, Jung Ryul Ahn, and Solomon S Senok.
Spontaneous oscillatory rhythms in the degenerating mouse retina modulate retinal gan-
glion cell responses to electrical stimulation.
Frontiers in cellular neuroscience, 9:512, 2016.

[80] Daniel K Freeman, Joseph F Rizzo III, and Shelley Fried.
Electric stimulation with sinusoids and white noise for neural prostheses.
Frontiers in neuroscience, 4:1, 2010.

[81] DL Rathbun, Nima Ghorbani, Hamed Shabani, Eberhart Zrenner, and Zohreh Hosseinzadeh.
Spike-triggered average electrical stimuli as input filters for bionic vision—a perspective.
Journal of neural engineering, 15(6):063002, 2018.

[82] Helga Kolb.
Circuitry for rod signals through the retina.
Webvision: The Organization of the Retina and Visual System [Internet], 2009.

[83] Michael R Deans, Bela Volgyi, Daniel A Goodenough, Stewart A Bloomfield, and David L
Paul.
Connexin36 is essential for transmission of rod-mediated visual signals in the mammalian
retina.
Neuron, 36(4):703–712, 2002.

[84] Sophia Wienbar and Gregory W Schwartz.
The dynamic receptive fields of retinal ganglion cells.
Progress in retinal and eye research, 67:102–117, 2018.

A

APPENDIX A

Perspective

Spike-triggered average electrical stimuli as input filters for bionic vision—a perspective

D L Rathbun[1,2,3,6], **N Ghorbani**[1,4], **H Shabani**[1,2,4], **E Zrenner**[1,2,3] **and Z Hosseinzadeh**[1,2,5]

[1] Institute for Ophthalmic Research, Eberhard Karls University, 72076 Tübingen, Germany
[2] Werner Reichardt Centre for Integrative Neuroscience (CIN), 72076 Tübingen, Germany
[3] Bernstein Centre for Computational Neuroscience, 72076 Tübingen, Germany
[4] Graduate Training Center of Neuroscience, International Max Planck Research School, 72074 Tübingen, Germany
[5] Center for Regenerative Therapies, Technische Universität, Dresden, Germany

E-mail: daniel.rathbun@uni-tuebingen.de (D L Rathbun)

CrossMark

Abstract

Bionic retinal implants are gaining acceptance in the treatment of blindness from degenerative diseases including retinitis pigmentosa and macular degeneration. *Objective*. A current obstacle to the improved performance of such implants is the difficulty of comparing the results of disparate experiments. Another obstacle is the current difficulty in selectively activating the many different retinal ganglion cell types that are used as separate pathways for visual information to the brain. *Approach*. To address these obstacles, we propose a modelling framework based on white noise stimulation and reverse correlation. In this perspective, we first outline early developments in visual retinal physiology leading up to the implementation of white noise stimuli and spike-triggered averaging. We then review recent efforts to adapt the white noise method for electrical stimulation of the retina and some of the nuances of this approach. *Main results*. Based on such white noise methods, we describe a modelling framework whereby the effect of any arbitrary electrical stimulus on a ganglion cell's neural code can be better understood. *Significance*. This framework should additionally disentangle the effects of stimulation on photoreceptor, bipolar cell and retinal ganglion cell—ultimately supporting selective stimulation of specific ganglion cell types for a more nuanced bionic retinal implant. Finally, we point to upcoming considerations in this rapidly developing domain of research.

Keywords: retinal prosthesis, retinal physiology, retinal implant, white noise, spike-triggered average

(Some figures may appear in colour only in the online journal)

Introduction

Overview

Retinal degenerations like retinitis pigmentosa and macular degeneration cause blindness worldwide. They are characterized by dysfunctional photoreceptors leading to the impairment of light detection in the retina. One approach to restore vision for such degeneration is a retinal prosthetic implant. The electrical stimulation provided by such devices elicit neuronal activity from the retina, perceived by the brain as visual objects called phosphenes.

According to the placement of the electrode array of the device, there are three main categories of retinal implant (Zrenner 2013). Epiretinal implants are placed on the retinal

ganglion cell (RGC) nerve fiber layer within the vitreous space (Weitz *et al* 2015). Subretinal implants are placed between the retina and the retinal pigment epithelium (Zrenner 2013). Finally, suprachoroidal implants are placed between the choroid and sclera near the external surface of the eye (Bareket *et al* 2017).

It is well-established that each of the main categories of retinal implant have the potential to activate RGCs directly (direct activation) or via activation of retinal network elements preceding the RGCs (indirect activation) (Weiland *et al* 2016). Yet, even now, controlling which network elements are activated remains an active domain of research. It is our belief that a better understanding of retinal activation can be achieved through a spike-triggered average (STA)-based modelling framework that we present following the *Introduction*. In this framework, the three neuron classes in the vertical (serial) pathway of the retina (photoreceptor, bipolar cell, and RGC) each have a characteristic filter that they apply to incoming electrical input; and this electrical input filter is passed down the pathway, eventually resulting in RGC action potentials (spikes). The electrical input filter is a formal model of a cell's sensitivity to electrical stimuli. It can be estimated by calculating the average stimulus preceding a response (the spike-triggered average). Functionally, by convolving the input filter with the stimulus, one can estimate how much a cell should be excited by any arbitrary stimulus. Throughout this work we will be careful to distinguish between the neuronal classes of the retina (photoreceptor, horizontal, bipolar, amacrine, and ganglion cells) and types that are found within each of these classes (e.g. ON, OFF, starburst, etc).

To provide the proper context for our modelling proposal, we outline the historical development of visual neuron characterization. This culminates with an overview of Gaussian white noise visual methods of characterization. Having reviewed visual characterization methods, we use this foundation as a springboard to discuss electrical noise characterization. We then exhaustively review recent attempts at adapting such methods to electrical stimulation of the retina for bionic vision (for a related treatment of electrical stimulation modeling, we recommend (Halupka 2017)). We next address specifics of electrical noise stimulation such as subthreshold and suprathreshold stimulation modes and how spike burst responses can be addressed in white noise electrical stimulation.

In addition to understanding how each of the main retinal neuron classes (photoreceptor, bipolar cell, and RGC) respond to electrical stimulation, an important open question remaining is 'How does each of the many cell types (e.g. ON versus OFF) within each class differentially respond to electrical stimulation?' Therefore, in addition to reviewing response characterization and white noise methods in retinal electrostimulation, we also review early work on that question with an emphasis on how the electrical input filter of different cell types within a class can help identify stimuli that selectively activate chosen cell types.

Finally, we conclude with a discussion of how current methods can be elaborated, the implications of so-called 'subthreshold' electrical noise stimulation on bionic vision, and challenges one may encounter with the proposed modelling framework that arise from considerations of the neural code of the retina.

Islands of knowledge

Although it is not obvious, our current understanding of how neural tissue responds to electrical stimulation is actually broken into a number of knowledge islands that only loosely communicate. These island nations are divided by their individual currencies and the uncertain exchange rates between them. On one island, the currency may be voltage, on another, it may be charge, and on others, it may be spatial or time derivatives or integrals of either of these. Examples include current (the time derivative of charge), charge density, current density, voltage curvature, etc. It is customary, therefore, to use simple conversion factors to compare between these different domains. For example, to calculate the current delivered by a voltage pulse, one might simply divide voltage by the impedance of the electrode. To calculate the charge delivered by a current pulse, one might simply integrate current across time. But such simplified conversions (yes, we are also guilty—(see Jalligampala *et al* (2017))) critically overlook considerations of how neural tissue sensitivity to any of these values can be nonstationary across time or space. Likewise, in practice the current produced by an electrode will not necessarily scale as a linear function of voltage (see Cogan (2008)). For example, if one researcher were to stimulate with a very low current, but over a very long time duration, activation of the neuron might not be achieved despite the integral of the current summing to the 'threshold charge' (one which results in a neural response) as determined by another researcher. As another example of flawed conversion, while impedance is normally reported in units of Ohms, allowing us to matter-of-factly substitute it into the familiar $V = IR$ equation, the reality is that the single impedance value is only really valid at the cycling frequency at which it was measured. This reflects that, for a square wave voltage pulse, the combined effect of the resistive and capacitive components of the experimental system will be a distorted current pulse. For more accurate predictions of the current associated with a voltage, electrochemical impedance spectroscopy can be used (Cogan 2008), but even this measure fails to capture the effect on impedance from the recent voltage history. Even the common conversion trick of discussing 'peak' or 'plateau' currents misses the fact that the biological system is integrating across the entire stimulus waveform.

To reconcile these disparate knowledge domains, we propose a modelling framework in which the system filter is estimated using white noise and spike-triggered averaging of the time varying charge passed into the neural tissue. We focus on this charge because, in our experience, this stimulus value most closely correlates to the transmembrane voltage that determines a neuron's response. By expressing neuronal excitation in terms of the instantaneous charge integrated in a leaky fashion by the neuron's filter, we believe that a universal definition of threshold can be achieved. The result will be that disparate experimental paradigms will all arrive at the same definition of what constitutes a threshold stimulus—regardless of stimulus waveform shape (see *A Modelling Framework for Retinal Electrostimulation*).

Retinal activation has many mechanisms

When the retina is stimulated as in a retinal prosthesis, spikes can be elicited from retinal ganglion cells (RGCs) through multiple mechanisms. The simplest mechanism is 'direct stimulation' of the RGC that activates its spike initiating zone (a high-density band of voltage-gated ion channels in the axon initial segment, AIS) (Wollner and Catterall 1986, Boiko *et al* 2003, Fried *et al* 2009, Jeng *et al* 2011, Werginz *et al* 2014). Within the category of direct stimulation are included both (1) an extracellular voltage gradient along the cell, inducing an intracellular current through the RGC dendrites, soma, and axon, thus leading to accumulation of positive ions within the AIS that activates the voltage-gated cation channels underlying the action potential, and (2) the creation of a localized hyperpolarization of the extracellular space adjacent to a segment of membrane with such cation channels (axon, AIS, or even somatic or dendritic segments), thus effectively depolarizing the transmembrane. Within this latter mechanism is the local depolarization of a distal segment of the axon (beyond the AIS) creating a bidirectional action potential—as when passing axons of distal RGCs in the nerve fiber layer are stimulated (Greenberg *et al* 1999, Grumet *et al* 2000, Jensen *et al* 2003, Rizzo *et al* 2003, Nanduri *et al* 2008, Chen *et al* 2009, Nanduri *et al* 2012, Werginz *et al* 2014, Weitz *et al* 2015).

In contrast, 'indirect stimulation' of RGCs is produced by activation of an upstream member of the retinal network that is then propagated to the RGCs through synaptic communication. Bipolar cells (BCs) and photoreceptors (PRs) are the network elements most susceptible to such activation because of their elongated architecture along the voltage gradient, although it may still be possible to directly activate the other elements of the retinal network—amacrine cells, horizontal cells, or even the Müller glial cells (but see Tsai *et al* (2011)). In network stimulation, the more likely mechanism of neuronal activation is the first one described for direct RGC stimulation where a voltage gradient across the retina induces an inverted voltage gradient within the neuron—ultimately depolarizing the presynaptic membrane to activate voltage-gated cation (primarily calcium) channels. However, with the miniaturization of electrodes, it may also someday be possible to locally depolarize the presynaptic membranes of the retinal network in the absence of a large transretinal electrical field. A primary goal of this paper, recognizing these many interacting mechanisms involved in electrical stimulation of the retina, is to lay out a conceptual framework to better understand how activation of the various retinal elements converges in the retinal ganglion cell to give rise to spike patterns that carry all retinal information into the visual centers of the brain.

Tickling the retina

Recently, our group and another in parallel have shown that the integration of sequences of subthreshold pulses can produce RGC spikes (Sekhar *et al* 2016, Ho *et al* 2018). We have termed this 'tickling the retina' to draw attention to this underappreciated approach and the accompanying need for a model of how it works. The main advantage of tickling the retina is

that probing electrical responsiveness of the retina in the context of ongoing stimulation better mimics the *in situ* environment of clinical retinal prostheses. Furthermore, we believe that the integration of ongoing stimulation can provide leverage to activate defined RGC types with greater selectivity than can be achieved with single suprathreshold pulses.

We demonstrate here that reverse correlation techniques can shed light on many active themes in the realm of retinal prosthetics. In particular, the technique of using spike-triggered averaging of a RGC's responses to a (noise) sequence of randomized electrical stimulus amplitudes has recently yielded promising results in this domain (Freeman *et al* 2010b, Sekhar *et al* 2016, 2017, Ho *et al* 2018, Maturana *et al* 2018). A detailed review of these and related studies is provided in *Electrical Noise Stimulation*.

A modelling framework for retinal electrostimulation

Suprathreshold electrical stimulation of the retina has been described using a diverse array of methods and metrics (Sekirnjak *et al* 2006). Example metrics include charge (Humayun *et al* 1999), voltage (Zrenner 2002), current (the time derivative of charge (Jensen *et al* 2003)), charge density (Rizzo 2003), current density (Eickenscheidt *et al* 2012), voltage curvature (Eickenscheidt and Zeck 2014), etc. (these are the *Islands of Knowledge* mentioned before). It is customary, therefore, to use simple conversion factors to compare between these different domains, but with the inherent shortcomings discussed in the *Introduction: Islands of Knowledge*. To reconcile these disparate windows into retinal electrostimulation, and to do so in the context of retinal network stimulation, we propose measuring the composite retinal filter using white noise and spike-triggered averaging of the time-varying charge that is passed into the neural tissue. It is this charge that is carried by the current through the tissue; and it is the ongoing flow of this charge which establishes and maintains the voltage gradients across the retina which, in turn, depolarize the voltage-activated membranes of the retinal neurons. Thus, electrical stimulation of the retina can be understood in terms of its effect on the retinal encoding of spikes that are provided as the retina's only output to the rest of the brain. With such a common currency, what have previously been mutually irreconcilable lines of research will be unified within a single framework.

Because typical prosthetic stimulation of the retina generates an electrical field spanning the thickness of the retina, all retinal neurons have the opportunity to respond depending on the spatio-temporal contrast along the field. Therefore, we propose that the electrical input filter of the retinal network during such stimulation is best understood as the combination, through the feedforward synaptic pathway of the retina, of electrical input filters from each element of the retinal circuit (figure 1). This composite filter is then passed through a nonlinear function for generation of RGC spiking responses. In this modelling framework, photoreceptors (PRs), bipolar cells (BCs), and RGCs each have their own electrical input filter for extracellular stimulation (figure 1(b)). The convolution
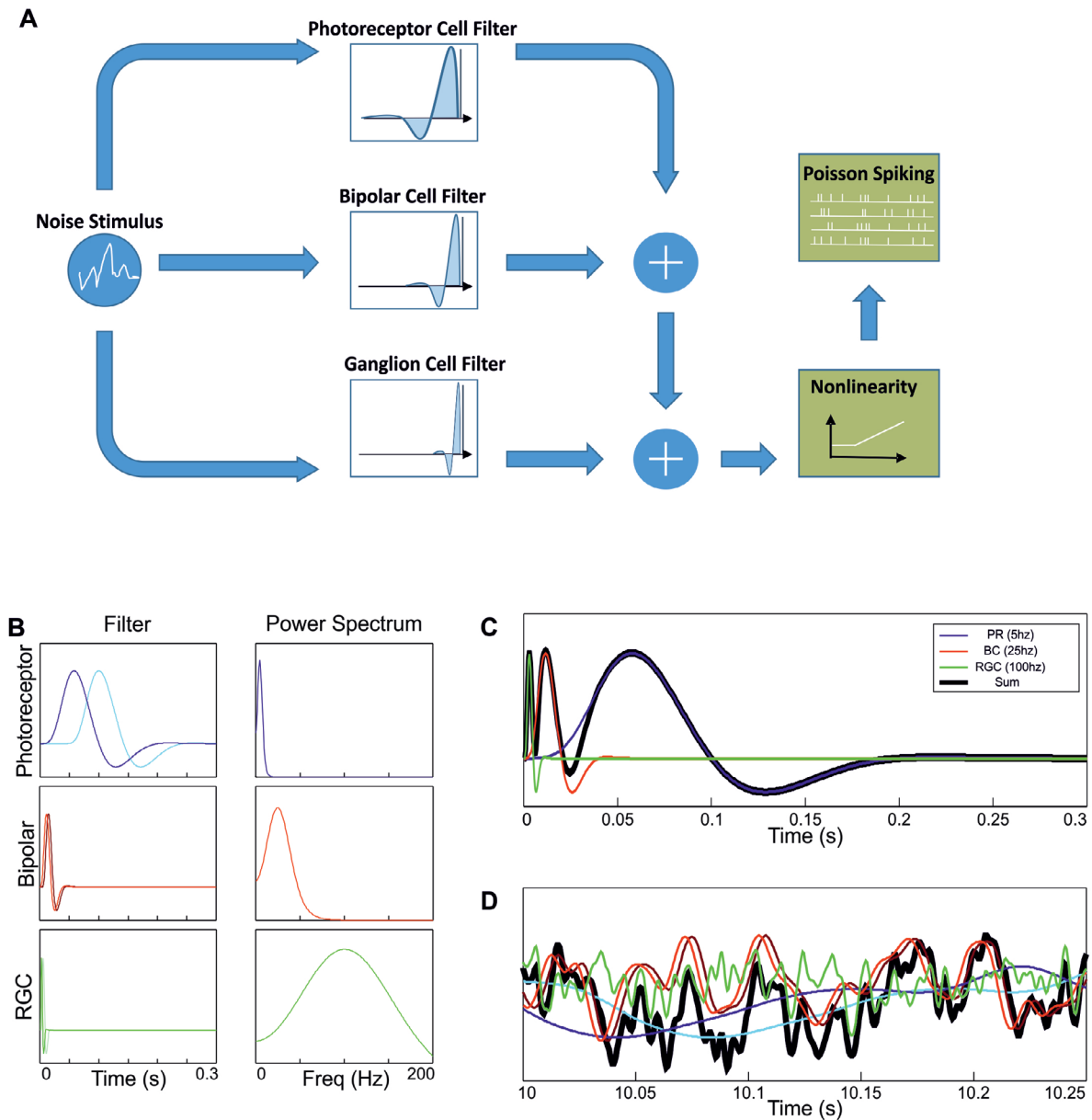
Figure 1. Three-stage filter. (A) Proposed modelling framework for how direct electrical noise stimulation of photoreceptor (PR), bipolar cell (BC), and retinal ganglion cell (RGC) may be combined to yield ganglion cell spiking responses. (B) (Left) In the proposed model, the PR, BC, and RGC filters are each shifted such that their peak latencies match the typical RGC spiking latencies for each source (100, 15, and 2 ms respectively; Boinagrov *et al* (2014)). (Right) The corresponding power spectrums show peaks at 5, 25 and 100 Hz, respectively ((Freeman *et al* 2010a); but see also (Twyford and Fried 2016)). (C) The three time-shifted filters are combined to yield the compound filter that would be measured from the RGC as a STA. (D) The generator signals resulting from presenting a noise sequence to each cell as well as the net RGC generator signal created by summing all shifted signals as described in (A). Vertical axes in (B)–(D) are in arbitrary units.

of these filters with the electrical stimulus yields the generator signal for each cell (figure 1(d)). However, for BCs, this generator signal must then be combined with that of the PR—but altered slightly by synaptic transmission to mimic feedforward input from PR to BC. This compound BC generator signal is then modified further as it is synaptically transmitted to the RGC and combined with that neuron's electrical generator signal to produce the compound generator signal of the RGC. Ultimately, the compound RGC generator signal is subjected to a spiking nonlinearity to produce the spike train that is used for generating the STA (e.g. Paninski *et al* (2007)). Thus, with careful experimental design, we believe it will be possible to

measure an electrical input filter from the RGC that reflects the filtering properties of not only the RGC but also the BC and PR (figure 1(c)).

The linear system modelling framework that we propose for electrical stimulation is similar to many previous visual models (e.g. Wohrer and Kornprobst (2009)), and estimates the duration and shape of the retinal circuit's memory for past charge delivery, thus capturing its temporal filtering behavior. It has the advantage of being empirically based on easily recorded spiking responses and the actual flow of charge through the tissue rather than the suspected charge or the command signal of the stimulator. In terms of converting
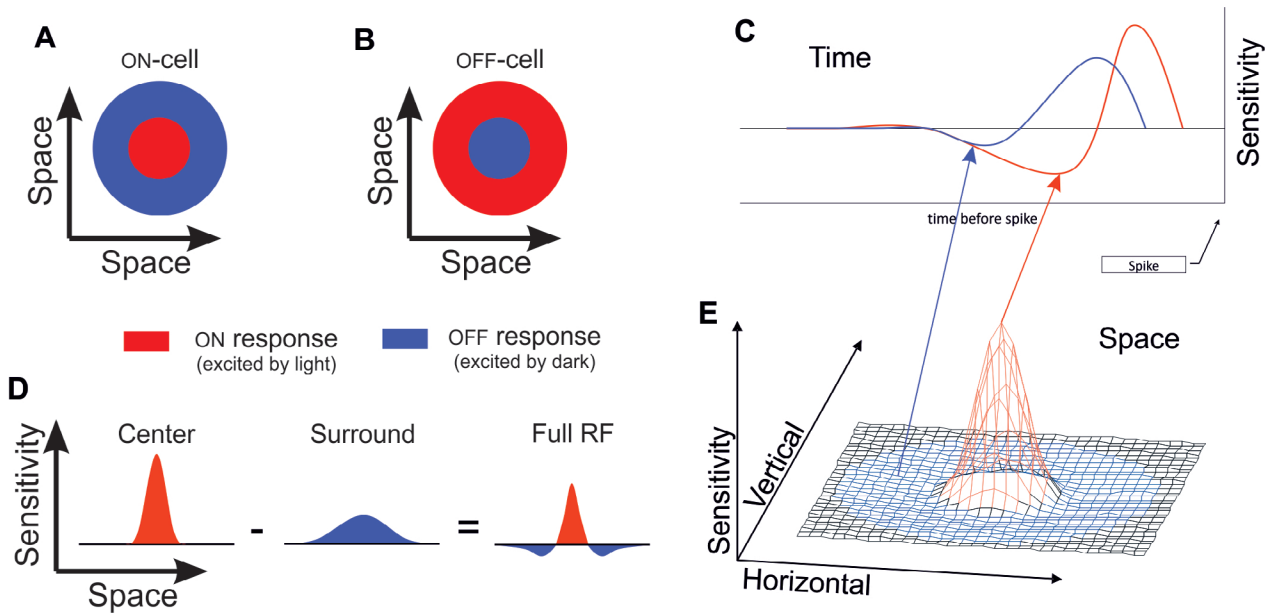
Figure 2. Spatiotemporal receptive fields. Antagonistic center and surround mechanisms contribute to the retinal ganglion cell visual receptive field in space for ON (A) and OFF (B) cells. Center and surround mechanisms combine in both time (C) with the surround delayed relative to the center, and in space (D) and (E) with the surround coextensive with the center. The net effect is a sensitivity profile in both time and space (C) and (E) combined) termed the spatiotemporal receptive field (STRF). (Adapted with permission from Rathbun (2009), figure 1.3.)

stimulation levels and threshold values between different studies, the modelling framework we propose will allow all researchers to talk about stimulation thresholds in the same units—that is to say 'integrated charge'. The instantaneous integrated charge of any arbitrary stimulus can simply be calculated as the convolution of the temporal stimulus charge sequence and the compound linear filter described here.

Visual response characterization

The receptive field

For any sensory neuron, there is a circumscribed region of sensory space over which the neuron is responsive to stimulation (figure 2). This region is termed the receptive field (RF). In visual neuroscience, the RF was first probed with punctate stimuli by luminaries such as Adrian and Matthews (1927), Hartline (1938), Granit (1946), Barlow (1953), Kuffler (1953), Hubel and Wiesel (1961) and Rodieck (1965). Such 'hand-mapping' was highly valuable in establishing a foundation for understanding how visual neurons integrate stimulation both across the RF and across time. Over the spatial extent of the RF, neurons typically vary in sensitivity, with sensitivity highest in the center of the RF, and smoothly falling off to the RF periphery (figures 2(d) and (e)). Moreover, due to lateral inhibition in visual networks, the RF typically has a center/surround structure in which stimuli that activate the center region inhibit the surround and vice versa. The consequence is to enhance local contrast, thus sharpening the spatial selectivity of the neuron. Across time, most sensory neurons act as leaky integrators over their RF. A leaky integrator is a circuit element that accumulates the effects of input stimuli over recent time, but slowly leaks this integrated input over time such

that the influence of previous stimuli completely vanishes if enough time has passed (figure 2(c)). Accordingly, it is useful to think of the RF of a visual neuron as applying a complex space-time filter to the visual stimulus (Rodieck 1965). For example, for some RGCs, the spatial RF evolves over time, imparting a selectivity to the neuron for stimulus frequency (Moore *et al* 2013).

Building on this concept of visual neurons as spatiotemporal filters, later researchers shifted to systematically characterizing their responses to sine wave stimuli that occupy well-defined spatiotemporal frequency bands of the stimulus space (Enroth-Cugell and Robson 1966). By combining a neuron's sensitivity to different frequencies, one can build a linear model of the neuron's filter in a given stimulus dimension (Shapley and Lennie 1985, Brodie *et al* 1978). This systematic sine-wave stimulation and accompanying formal modeling laid the conceptual groundwork for white noise methods.

White noise stimulation and the STA

Building on the success of sine wave-based linear models, spike-triggered averaging has been used to understand the filtering properties of visual neurons in both the spatial and temporal domains for many decades (Marmarelis and Naka 1972, 1973a, 1973b, 1973c, Korenberg and Hunter 1986, Ringach and Shapley 2004, Sharpee 2013). In generating the spike-triggered average (STA), the stimuli that precede each neuronal spike are averaged together to yield an estimate of the input filter for that neuron. Tightly coupled to spike-triggered averaging has been the presentation of *Gaussian white noise* stimuli. Here, the term 'white' indicates that the distribution of frequency amplitudes (e.g. across the temporal domain) is relatively flat, in analogy to the photon frequency distribution
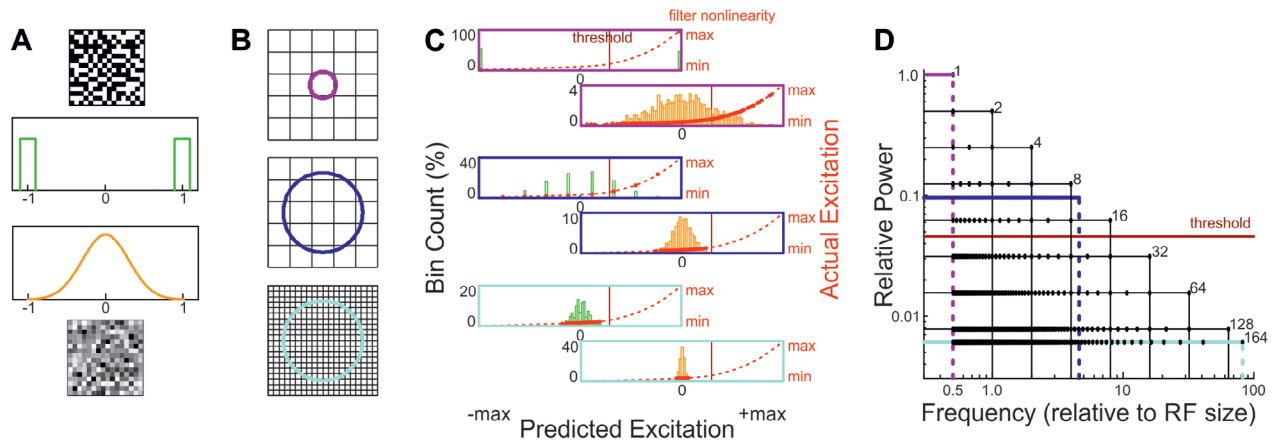
Figure 3. Matching stimulus and receptive field sampling density. (A) Binary (top) and Gaussian (bottom) stimulus amplitude distributions and example stimulus frames for a 16×16-check spatial layout. (With such stimuli, instead of 'pixel' the term 'check' is often used in analogy to a checkerboard in order to discriminate between stimulus elements and pixels of the visual display device.) For each video frame of a time-varying stimulus, the brightness of each check is drawn independently from either the binary or the Gaussian distribution. (B) Relationship of the neuronal receptive field (RF) size to the stimulus with either one (top), a few (middle), or many (bottom) checks being integrated by the RF. (C) Generator signal sampling distributions (arbitrary units) produced by the stimulus/RF combinations shown in (B). In each pair of plots, sampling distributions for binary (left) and Gaussian (right) stimuli are shown. Bar colors correspond to the stimulus distributions in (A); plot borders correspond to the stimulus/RF pairings of (B); the underlying stimulus/response nonlinearity of the cell is the dotted red line with sampled points indicated by red dots, and the threshold indicated in maroon. Left y axis corresponds to bar heights, right y axis corresponds to the nonlinearity. (D) Spatial frequency power spectrum of the RF-filtered stimulus relative to the Nyquist frequency of the stimulus. Black points indicate the frequencies that can be sampled for any given RF/stimulus pairing. The three pairings of (B) are indicated with lavender, blue, and cyan lines. Threshold of the cell is shown in maroon.

of white light. This is achieved by sampling the amplitude values (e.g. brightness) randomly from a Gaussian distribution at regular intervals across the stimulus domain (e.g. time). Such white stimuli are often also referred to as 'noise' stimuli, in analogy to their resemblance to a noisy audio signal—reflecting the fact that the power-balanced frequencies are uncorrelated in their phases. For visual stimulation, such a Gaussian white noise stimulus can be sampled simultaneously across multiple orthogonal stimulus domains such as time, space, and color (Devries and Baylor 1997, Chichilnisky 2001). In contrast to earlier sine wave experiments this process can be much more efficient, as the entire frequency space can be probed simultaneously with a single noise stimulus rather than sequentially with multiple different sine waves.

Binary noise and noise stimulus design

We address the binary noise case here because it is particularly useful in understanding important nuances of noise stimulus design. A common special case of the Gaussian noise stimulus is binary noise. At first glance, this would seem to be a contradiction in that Gaussian and binary distributions are mutually exclusive. However, the central limit theorem demonstrates that if enough binary samples are integrated by a system, the distribution of integrated values approaches a Gaussian distribution (as shown in figure 3(c), left plots). This points to an important consideration in the design of any noise stimulus for spike-triggered averaging. Specifically, it is important not only to consider the distribution of stimulus amplitudes but also the expected filter shape of the neuron as well as the filter size relative to the stimulus sampling resolution. This point is elaborated for the spatial domain in figure 3. In matching the

stimulus to the neuronal filter, a balance must be struck. On the one hand, it is desirable to generate a wide range of neuronal excitation levels so that the input/output function of stimulus versus response can be sampled densely—especially the degree of nonlinearity in this function. The prediction of how much a stimulus should excite a neuron based on a linear convolution of that stimulus with the neuron's filter is called the 'generator signal' (Chichilnisky 2001). The generator signal can be loosely interpreted as a prediction of the non-spiking membrane potential of the neuron, as is typically measured with patch-clamp recordings. Mathematically, the expression of this generator signal is equivalent to a dimensionality reduction whereby the multiple stimulus dimensions are reduced to a single dimension corresponding to the predicted excitation level of the cell. On the other hand, competing with the need for high-density sampling is the need for the stimulus frequencies to be sampled with enough power that the filter shape can be determined with sufficient resolution. Figure 3(d) demonstrates how the power at which stimulus frequencies are sampled decreases as more frequencies are sampled. Beyond a threshold power, the neuron will not respond to the stimulus frequencies. To elaborate, if the match between the stimulus presentation density and the neuronal filter is such that only one stimulus element influences the response at each time point (figure 3(b), upper plot), the generator signal distribution remains the same as the original stimulus distribution (figure 3(c), upper pair of plots). Additionally, only low-frequency stimuli (relative to the RF size) can be presented (figure 3(d), lavender lines). In contrast, if the stimulus is designed such that the filter integrates across too many stimuli, the generator signal distribution becomes much narrower around the stimulus mean (figure 3(c), lower pair of plots) and, although many

frequencies are sampled, the sampling power at all frequencies falls below the threshold detection level (figure 3(d), cyan lines). Therefore, it is critically important that a noise stimulus is designed such that both the generator signal and sampled frequencies span a wide range of values at a sampling density that is useful for the question at hand. In the examples in figure 3(c), the top plot for the Gaussian stimulus and the middle plot for the binary stimulus provide the best sampling of the filter nonlinearity. This tradeoff between stimulus power and sampling density is a crucial, but often neglected consideration in the design of noise stimuli.

Electrical noise stimulation

In analogy to the success of *visual* noise stimulation, multiple groups have sought to develop a method of delivering noise-based *electrical* stimulation to the retina. In doing so, the typical goal is that temporal filters can be estimated for prosthetic stimulation of the retina. The earliest electrical noise stimulation we have identified in the visual prosthesis literature was by Ryu *et al* (2009), and revisited in Ryu *et al* (2017), although the use of noise in auditory electrostimulation predates this by more than two decades (Motz and Rattay 1986, Morse and Evans 1996). Curiously, while noise stimulation was used to examine the fidelity of the current amplitude encoding in the spike train, the data does not appear to have been used to calculate the electrical input filter via STA. At stimulation rates of 1–10 Hz, it is possible that temporal integration across subsequent pulses was rare and that only single-pulse activation was observed.

In a more relevant study by Freeman *et al* (2010b), electrical current was modulated by a binary noise sequence from a nearby epiretinal stimulating electrode during cell-attached patch-clamp recordings of RGCs. For both spiking responses and the membrane voltage, reverse-correlation kernels (electrical input filters) were calculated, yielding a biphasic waveform with a peak latency of 25 ms and a likely preferred frequency around 5–10 Hz. Although promising, we are unaware of any work following up on this first demonstration of STAs relevant to prosthetic vision.

A few years later, Lorach *et al* (2015) delivered a 'sparse' spatio-temporal binary noise stimulus to their subretinal electrode while recording ganglion cell spike trains. Sparse refers to sequential stimulation at single points in the stimulation space, in contrast to simultaneous stimulation at all points. They reported maps of the spatial and temporal sensitivity profiles that they termed an electrical receptive field (eRF). To create these maps, only one of the 142 electrodes were stimulated at a time, at a refresh rate of 2 Hz. Because of this low rate and sparse design, we consider this method to be more analogous to the visual hand mapping discussed earlier rather than the noise-based STA method, since a rate of 2 Hz appears insufficient for multiple pulses to be integrated by the temporal filters of the retina that have been subsequently reported. In this paper, the temporal response pattern was reported, but this pattern is best identified as an 'impulse response', in contrast to the related but distinct 'temporal filter' that is typically produced from noise stimulation. A common mistake is

to assume that the impulse response and temporal filter are identical, however, this equivalence is only true in a purely linear system (unlike the nonlinear retina). The most important distinction here is that the impulse response only provides temporal information about the spiking response pattern after the activation threshold has been crossed. In contrast, the input filter estimated from noise stimulation better reflects the generator signal leading up to a spiking event. These two time series, the impulse response and the temporal filter, are only identical if the relationship between generator signal and response is perfectly linear (Bracewell 1986). Interestingly, the spacing of electrodes (70 μm pitch) is appropriately matched to the spatial eRF to allow true noise mapping—had the authors activated multiple pixels at a time as in their more recent paper (Ho *et al* 2018). Based on these earlier methods, however, only points in the receptive field which can independently activate the cell were mapped. With non-sparse Gaussian noise mapping—even at a stimulation frequency of 2 Hz, one could expect such methods to yield a full mapping of the excitatory and inhibitory eRF regions.

Shortly following the Lorach *et al* work, Maturana *et al* (2016) extensively examined Gaussian white noise estimation of the spatial eRF. They too stimulated at a frequency too low to probe the temporal filter (10 Hz). Although their electrodes were subretinal, they primarily examined direct RGC stimulation. They found that weighting pulse amplitudes across 2, or 3 electrodes in proportion to the eRF was more efficient than naïvely weighting all effective electrodes equally. Furthermore, they found the same 1, 2, or 3 effective electrodes for both cathodic-first and anodic-first biphasic pulses. Using spike-triggered covariance (STC) analysis, they found that the STA estimate of the spatial eRF was typically sufficient to explain how RGCs responded to direct stimulation by combinations of electrode, and that higher order interactions between electrodes played little role in RGC responsiveness. Importantly, the STC analysis revealed that simple STAs, while often correct, had weak amplitudes due to the antagonistic effects of similarly effective cathodic-first and anodic-first biphasic pulses in the STA calculation process. A recent study that similarly examined the eRF can be found in Esler *et al* (2018), demonstrating how these methods are being quickly adopted by the research community. Interestingly, this latter study showed that the types of linear models described here are good approximations for much more complex biophysical models of retinal electrical stimulation.

More recently, our group (Sekhar *et al* 2016, 2017) and another (Ho *et al* 2018) have finally been successful in measuring temporal electrical input filters from network-based stimulation of RGCs. We first reported this success in 2016 when we stimulated the mouse retina epiretinally with 1 ms, cathodic, voltage-controlled pulses delivered at a rate of 25 Hz and with an amplitude distribution largely falling below single pulse activation thresholds (figure 4). We found that the electrical input filters of many retinal ganglion cells had a strong negative deflection with peak latencies typically in the range of 100 to 400 ms (figure 4(c)). Mathematically, the STA can be thought of as a vector in stimulus space pointing from the center of the original stimulus distribution towards
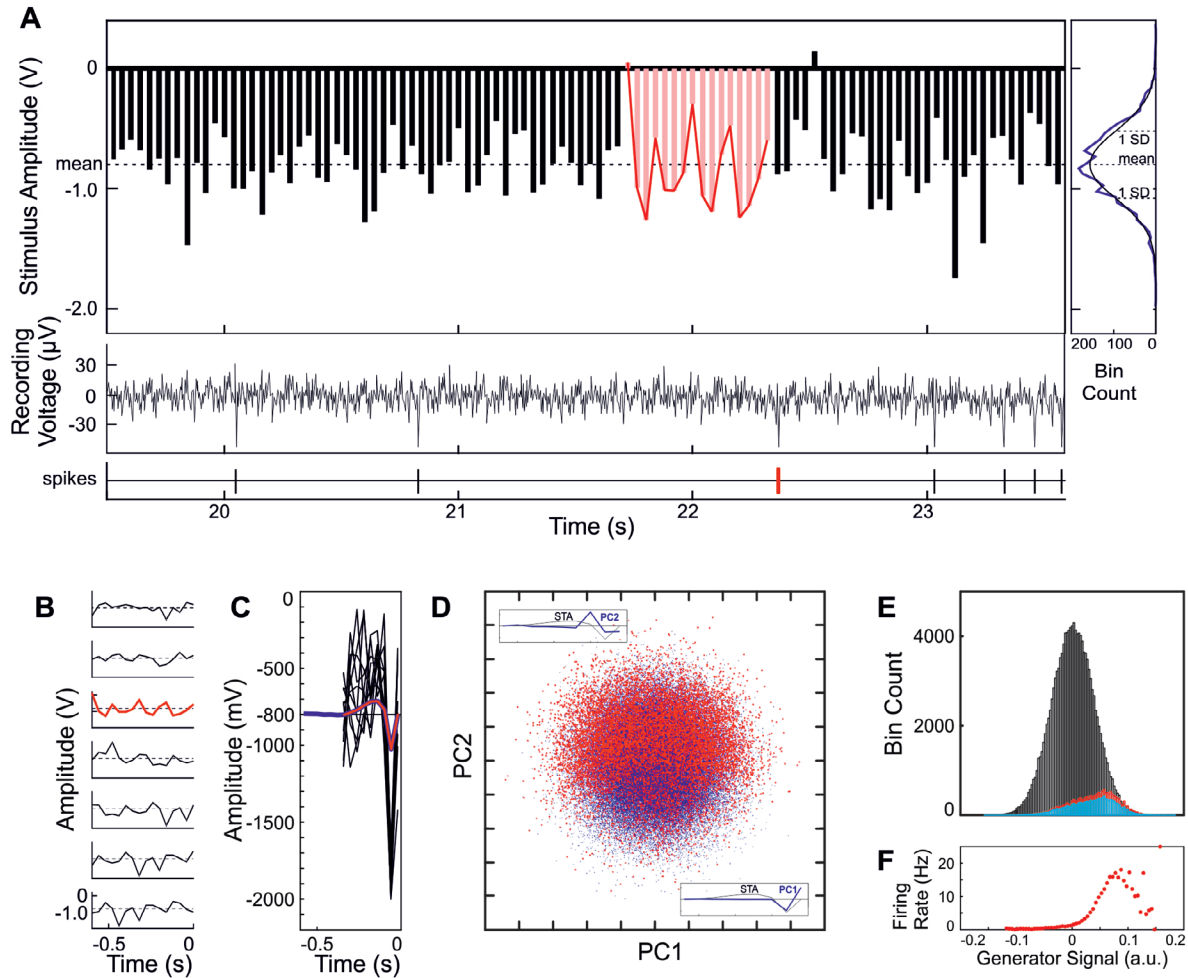
Figure 4. Spike-triggered Averaging. (A) Stimulus segment (top) containing a random pulse amplitude sequence of 1 ms pulses at 25 Hz with accompanying high-pass filtered voltage recording (middle) and spike train rastergram (bottom). An example pulse sequence and its associated spike are highlighted in red. Pulse amplitudes were drawn randomly with replacement from a Gaussian distribution shown at right in blue. Dotted lines mark mean and SD voltages. (B) Sample pulse amplitude sequences of the seven spikes from (A). (C) Average pulse modulation sequence preceding all spikes (blue) overlaid with individual sequences that best matched the STA (black) and the significant kernel used for calculating the generator signal (red). (D) Scatterplot of the first and second principal component amplitudes for all stimulus waveforms (blue points) with waveforms preceding spikes overlaid in red. Insets show the principal components overlaid with the STA. (E) Generator signal was calculated by convolving stimulus sequences with the STA kernel. Generator signal distributions for all stimuli (black), for spike-associated stimuli (blue) and for spike count weighted spike-associated stimuli (red) are overlaid. (F) The spike generation nonlinearity derived from (E). For high signal values low sample size leads to uncertain firing probability estimates. (Adapted from Sekhar *et al* (2016), figure 1. © IOP Publishing Ltd. All rights reserved.)

the center of the spike-associated stimulus ensemble (figure 4(d)) (Schwartz *et al* 2006). By plotting the probability that stimuli of a given generator signal range will elicit a spike, the nonlinearity relating generator signal to neuronal response can be estimated (figures 4(e) and (f)). Examining the stimulation frequency for pulse trains, we found that 10 Hz seldom yielded useful filters. In contrast, 50 Hz stimulation produced very smooth filters; however, because of the lower temporal contrast of the stimulus (as discussed for spatial resolution in figure 3), such fine resolution stimulation drove fewer spikes—requiring longer recording times to yield enough data for STAs. Accordingly, we settled on 25 Hz pulse trains as an optimal frequency to provide smooth STAs in a reasonably short recording time. Likewise, we compared 20% versus 35% contrast in the Gaussian distribution of pulse amplitudes and found that, while both contrasts produced useful filters, the

higher contrast drove higher firing rates. We next examined the STAs of degenerated mouse retinas and found them to be drastically altered relative to healthy retinas. We concluded that the healthy filters are likely the result of photoreceptor (PR) stimulation being passed on through the retinal network to the RGC and therefore, the electrical input filter measured under these conditions primarily reflects the filter of PRs. Complementary to these experiments, Ho *et al* (2018) used a subretinal electrode array to stimulate the rat retina with a spatiotemporal binary noise sequence at a refresh rate of 20 Hz. Both their study and ours found filters with peak sensitivities in the 2–10 Hz range, although our filters tended to have slower onset latencies and longer durations. Based on these frequencies as well as the effects of degeneration and PR transmission blockade, they agreed with our conclusion that the filters are primarily the result of PR stimulation transmitted to RGCs
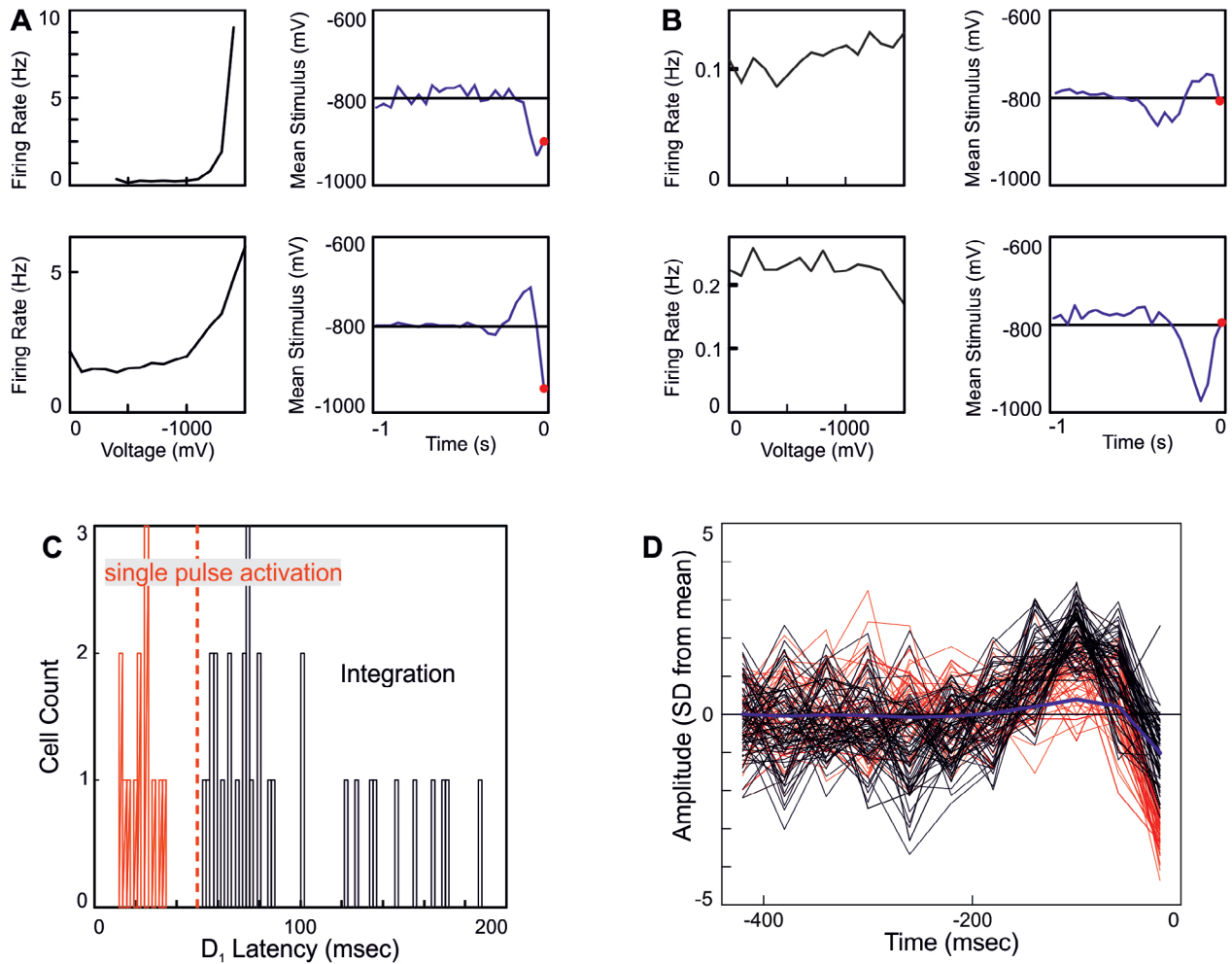
Figure 5. Two stimulation modes—single pulse and pulse integration. (A) For two example cells, the firing rate within 40 ms of a pulse is plotted against the amplitude of that pulse to yield a voltage-response curve (left), demonstrating the threshold for single pulse activation via network stimulation. The STA for each cell is shown in blue at right. (B) As in (A), but for two RGCs that do not respond to single pulse stimulation. Note the red point in each of the 4 STAs. The RGCs in (A) exhibit notable single pulse activation in the first time point to the left of 0 in their STAs while the RGCs in (B) do not. (C) Distribution of first STA deflection latencies when STAs are not corrected for single-pulse activation. (D) Overlay of pulse modulation waveforms with (red) and without (black) single pulse activation for another sample cell. (Adapted from Sekhar *et al* (2017), S2. © IOP Publishing Ltd. All rights reserved.)

via the retinal network. We suspect, however, that given the higher frequency, multiphasic filters they sometimes reported that PR-mediated stimulation may have combined with bipolar cell (BC) stimulation for some cells (see *Modelling Retinal Electrostimulation*). We also suspect that some of the filters reported in the Ho *et al* study resulted from single suprathreshold pulse activation rather than the integration of multiple pulses (as discussed in the next section). This supposition is based on their fast onset latencies, short peak latencies, and narrow widths—although the Nyquist limit of 20 Hz stimulation (10 Hz) makes it difficult to be certain.

Finally, in a paper published by Maturana *et al* (2018), synaptic blockers were used to distinguish direct and indirect activation by a space-time varying electrical noise stimulation. While their previous discovery—that the spatial eRF characterizes well the linear interactions of multiple electrodes—holds true for direct stimulation, indirect stimulation appears to involve more nonlinear interactions. By stimulating at rates of 10, 20, and 30 Hz, they reinforce that rates higher than

10 Hz are necessary to accurately detect electrical input filter components arising from network activation.

'Subthreshold' stimulation

Our use of electrical white noise confirmed our suspicion that stimulation of the network to activate RGCs can function through two distinct mechanisms (figure 5). On the one hand, Single pulse amplitudes that are strong enough can activate the network by themselves (figure 5(a)). On the other hand, analogous to the integration of subthreshold postsynaptic potentials that is a basic principle of neuroscience, a series of 'subthreshold' electrical pulses can be integrated by the network to achieve activation (figures 5(a) and (b)). It is this latter mechanism that we have termed 'tickling the retina' and that has proven useful in understanding the electrical input filter. Appreciation of these two mechanisms requires a reevaluation of the concept of the electrical stimulation threshold. Traditionally, single pulses have been delivered while some

aspect of the pulse (amplitude, duration, shape, interphase interval, etc) was varied to determine the value beyond which reliable stimulation can be achieved. This value is then termed the threshold. However, recognizing that neurons can integrate multiple *subthreshold* stimuli across time, such a simple concept of threshold becomes muddled. In the *Modelling Retinal Electrostimulation* section we introduce the concept of an integrated charge threshold to delineate between these two mechanisms of electrical activation.

In examining our electrical STAs, we found evidence in some RGCs that single pulse activation and multi-pulse, integrative activation might be combined into a single STA (figures 5(a) and (d)). While integrative activation tended to have a peak latency above 50 ms, the single pulse activation had latencies closer to 20 ms (figure 5(c)). To validate this observation, we plotted the firing rate of the RGC during the 40 ms interval following each pulse against the amplitude of that pulse (figures 5(a) and (b)). As suspected, RGCs with a contribution from single pulse activation showed a strong increase in firing rate approaching the high end of our stimulus pulse amplitude distribution (figure 5(a)). In contrast, RGCs with no contribution from single pulse activation did not show such a firing rate increase (figure 5(b)). In order to better represent the integrative electrical input filter, we subsequently nullified the first time sample in the STA by setting it to the mean stimulus value, thus discarding the contribution of single pulse activation (within 40 ms latency of each pulse).

Conveniently, the plot of firing rate versus pulse amplitude relates directly to earlier studies of the voltage amplitude threshold for single pulses (figure 6). Beyond this relationship, however, calculating the single pulse amplitude threshold from noise stimulation has two advantages. First, because long recovery periods are not interleaved between successive pulses, the resolution with which voltage amplitudes can be probed is much higher for a fixed recording time, providing for a much more detailed voltage-response curve than in traditional studies (Jalligampala *et al* 2017). Second, by measuring the voltage-response function in the context of ongoing electrical stimulation, the adaptive phenomenon of desensitization (Weiland *et al* 2016) is held constant and the adaptation state of the retina is better matched to that of real-world prosthetic stimulation (Hosseinzadeh *et al* 2018). It will be informative to compare such white-noise generated stimulus-response curves to those generated under traditional methods in the same experiment. In doing so, we expect to better understand the role of adaptation (visual and electrical) in altering the sensitivity and gain of RGC coding in response to electrical stimulation.

Spike burst correction

In our indirect stimulation experiments, we have found that RGCs respond to noise stimulation with both individual (tonic) spikes and bursts of multiple spikes in short succession. The fraction of spikes that occur in a burst appears to vary across the RGC population but is expected to be somewhat stereotyped within each of the many RGC types (Wong
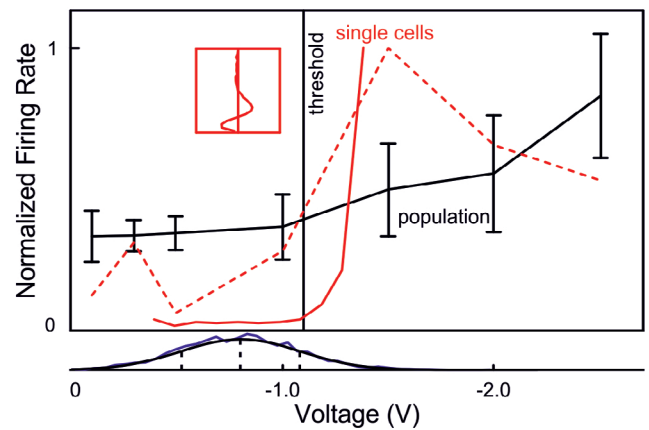

Figure 6. Measuring threshold from noise stimulation. Overlay of voltage-response curves for: (1) a single RGC (dotted, red) and (2) a large population (solid, black) using traditional methods (1 ms pulses presented at 5 s intervals, 20 repetitions each, response integration window: 10–100 ms, (per (Jalligampala *et al* 2017))) as well as for (3) a single cell using white noise (thick, red). Inset is to scale on the voltage axis and demonstrates the amplitude of the STA relative to the voltage-response curve for the cell stimulated with white noise (thick red line). White noise stimulus distribution from figure 3 is replotted below for context. (Adapted from Sekhar *et al* (2016), figure 3. © IOP Publishing Ltd. All rights reserved.)

et al 2012). By examining the time intervals before and after each spike, we were able to classify each spike as either a tonic spike or for bursts, a first spike, intra-burst spike, or last spike (figures 7(a) and (b)). When electrical stimulation triggers a burst of spikes, the undesired effect will be to smear out the STA across time. This is because the latency between the triggering stimulus and each of the spikes in the burst increases for later spikes. This poses a problem when the STA is being used to understand the average stimulus that drives an RGC to respond. Accordingly, we have described a method of correcting for temporal smear in the STA caused by bursts (Sekhar *et al* 2016). The result is the first spike-triggered average (fSTA). In such burst correction, the first spike of each burst is identified. Then the contribution of the stimulus preceding that burst is weighted by the number of spikes in the burst to reflect the reality that stronger stimuli tend to produce bursts with more spikes in them. While burst correction had little effect for some RGCs (figure 7(c)), we found that others exhibited notable changes in the shape and timing of their STAs (figure 7(d) and (e)). So far, we have found little difference between STAs calculated with only corrected burst responses versus those calculated with only tonic spikes, suggesting that one can consider tonic spikes to be bursts of only one spike. However, more work is needed to fully explore how tonic and burst spikes in the retina may encode distinct information about electrical stimulation.

Type-specific retinal stimulation

The neurons of the retina can be divided into five primary cellular *classes* (photoreceptor, horizontal, bipolar, amacrine, and ganglion), each of which incorporates numerous *types* and subtypes (Masland 2011, Baden *et al* 2016, Franke *et al*
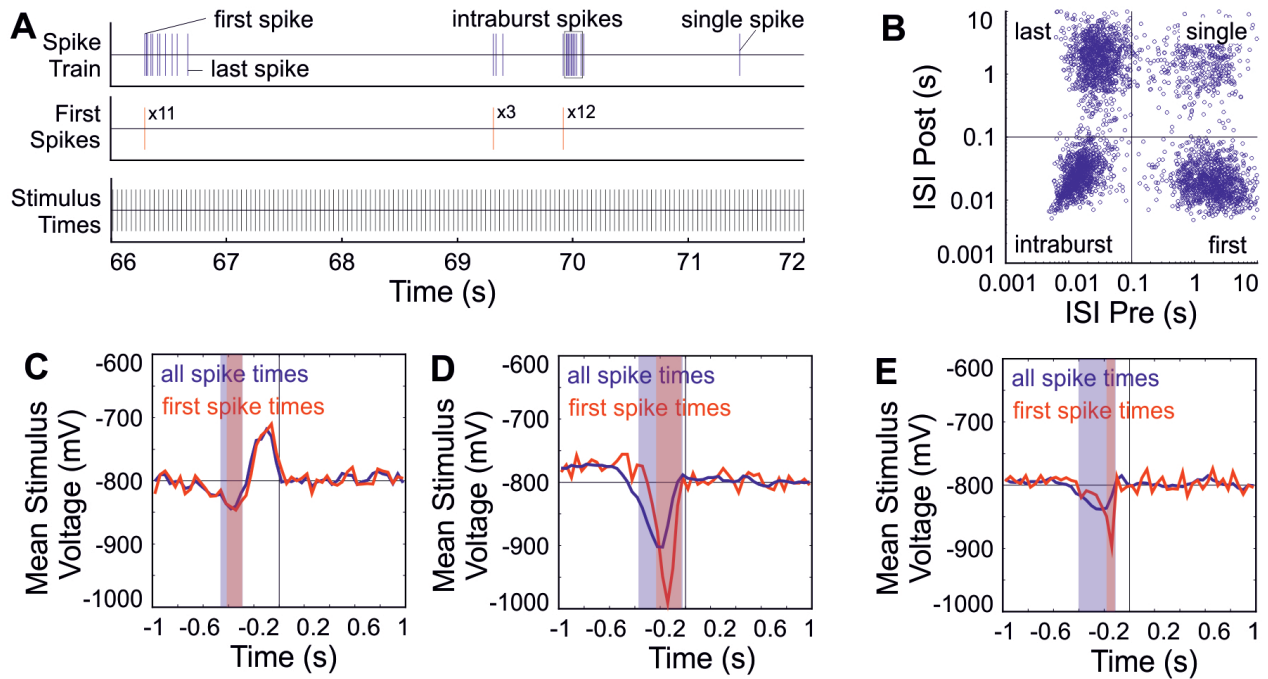
Figure 7. Burst Correction. (A) Classification of RGC spikes: all spikes within 100 ms of each other were considered burst spikes, while remaining spikes were singleton (tonic) spikes. Burst spikes were classified as either first, last, or intraburst spikes. To correct STA calculations for burst responses, the first spike of each burst was weighted according to the number of spikes in the burst. (B) A plot of following interspike interval (ISI) against preceding ISI for every spike of an RGC reveals these four spike categories. (C)–(E) Uncorrected (blue) and burst corrected (red) STAs for three example cells showing the range of effects for burst correction. Shaded regions mark negative deflections for each STA. (Adapted from Sekhar *et al* (2016), figure 2. © IOP Publishing Ltd. All rights reserved.)

2017). Within the feedforward pathway of PR to BC to RGC, it has been shown that temporal filtering for electrical stimulation becomes progressively higher in preferred frequency (Freeman *et al* 2010a, Twyford and Fried 2016).

Of particular interest are the many types of retinal ganglion cells which differ from each other due to their individual cellular physiologies as well as their pattern of inputs from the retinal network (Baden *et al* 2016). Crucially, Wong *et al* (2012) showed a diversity of electrical responses in RGCs due to their intrinsic physiological properties. With the inclusion of the diversity of network connections that is known to exist, it is reasonable to hope that many RGC types will have key electrical stimulation patterns that can selectively activate them without strongly activating other RGC types. As an early foray into this domain, both we and Ho *et al* (2018) have demonstrated that the electrical input filters for visual ON and OFF RGCs tend to be mirror reflections of one another, likely due to dominant activation of photoreceptors (figure 8). This result reflects earlier work by Freeman *et al* (2010a). In that study, they used a similar systems modeling approach to ours, but with the presentation of current-controlled sinusoids with varying temporal frequencies—sampling just one frequency at a time in contrast to white noise stimulation. Their strategy echoes early developments in visual response characterization using sinusoids. They found that visual ON cells tended to respond during the anodal phase of a slow (5 Hz) sine wave while OFF cells responded during the cathodal phase. Other recent contributions to growing evidence of cell-type selective stimulation include (Guo *et al* 2014, Goetz *et al* 2015,

Twyford and Fried 2016, Im and Fried 2016, Qin *et al* 2017, Im *et al* 2018, Guo *et al* 2018).

It remains unclear whether the differential filters found in healthy retina will be reflected in degenerate retina. Likewise, it remains unknown whether the different RGC types will each have a unique filter. Nevertheless, as noise stimulation methods become more refined and our ability to functionally discriminate RGCs improves (see Baden *et al* (2016)) we expect that further differences in electrical input filter shapes (spatial and/or temporal) that correlate with functional RGC type will be revealed. In doing so, we expect that methods will be derived that allow bionic retinal implants to selectively address the different visual information channels of the retina, and thus provide a more nuanced visual percept for implant patients (Barriga-Rivera *et al* 2017). Indeed, the diversity of electrical spatiotemporal receptive fields recently described in Maturana *et al* (2018) provides strong support for such optimism.

Another domain of controversy for the electrical filters that have been recently described is the upper limit they may place on the maximal possible stimulation frequency. With electrical filters on the order of 500–1000 ms in duration, a reasonable expectation is that discrete stimulation may only be possible at rates around 1 Hz. However, a relevant detail that remains unknown is whether integration of electrical stimulation resets after a response. If there is no reset, then continuous stimulation could achieve much higher rates than discrete stimulation. Also unknown is the filter duration for bipolar cell-mediated activation of RGCs. While photoreceptors seem
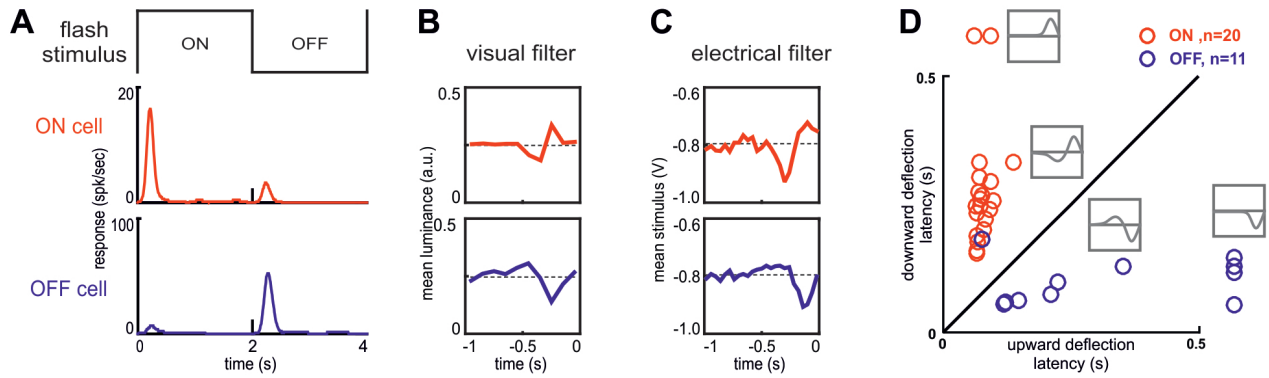
Figure 8. Correspondence of visual and electrical responses. (A) responses of example ON (red) and OFF (blue) RGCs to on/off flashing stimulation. (B) Visual input filters (STAs) for these cells calculated from full-field, 10 Hz, Gaussian visual noise stimulation. (C) Electrical input filters (STAs) of the same cells calculated from 25 Hz, cathodic, Gaussian noise electrical stimulation as described above. (D) Latencies of the upward and downward electrical input filter deflections for a population of cells. Some cells have monophasic filters while others are biphasic (schematic inserts). (Adapted with permission from Sekhar *et al* (2017) figures 3 and 5, first appeared in Rathbun and Hosseinzadeh (2017), figure 4.)

to have the long filters described thus far, bipolar cells are expected to have notably shorter filters that could support higher stimulation rates.

Discussion and future directions

Multidimensional sampling

As with visual noise, electrical noise has the ability to more efficiently sample from the potential stimulus space (figure 9). In the method we developed, we only explored the amplitude dimension as a proof-of-principle (Sekhar *et al* 2016). Nevertheless, even this dimension was sampled more efficiently than in more traditional methods (see figure 6). In contrast, the binary noise stimulus used in Freeman *et al* (2010b) better sampled the duration space, but at the expense of the amplitude dimension. In the future, researchers should strive to develop stimulation and recording methods that will allow multiple dimensions to be probed simultaneously.

In contrast to our focus on stimulus dimensionality in time, many other researchers have examined the spatial dimension of the eRF with noise stimuli (Lorach *et al* 2015, Maturana *et al* 2016, Halupka 2017, Halupka *et al* 2017). The use of noise stimuli allows powerful computational methods like the STA, spike-triggered covariance (STC), and linear-nonlinear-linear modeling (Halupka *et al* 2017) to be used. Nevertheless, more traditional hand-mapping styles of estimating the eRF have also been used by a number of researchers recently (Stett *et al* 2000, 2007, Eickenscheidt *et al* 2012, Jepson *et al* 2014, Sim *et al* 2014, Stutzki *et al* 2016). Combining spatial and temporal noise mapping has proven to be a difficult task, however two reports this year demonstrate that such multidimensional eRF mapping is possible (Ho *et al* 2018, Maturana *et al* 2018). By incorporating the spatial dimensions into noise stimulation, even more refined methods of RGC type-specific stimulation may be discovered.

In contrast to asking about the underlying spatial eRF, many researchers have pursued electrical field shaping strategies to understand how multiple simultaneously activated electrodes

can be weighted to best direct stimulation to a chosen neuron (Savage *et al* 2012, Matteucci *et al* 2013, Dumm *et al* 2014, Spencer *et al.* 2018). Beyond considering combinations of stimulating electrode, field shaping also considers the role of return electrode in determining the path taken by current flow. In modern neuroprosthetics, field shaping (including current steering and current focusing) is a relatively new field of discussion that has been more extensively pursued for cochlear implants (Bonham and Litvak 2008). The field shaping concept considers the overlap of individual electrical fields from several electrodes and their influence on the overall electric field. It is applied either to focus the current in order to excite a narrowing region in tissue or to redirect the pulses for excitation in different regions of the tissue (Dumm *et al* 2014). It is reasonable to expect that field shaping techniques might support cell-specific stimulation above and beyond that achievable by tailoring stimulation to the characteristic eSTRFs of selected RGC types. Furthermore, it appears that in a fully 3D structure like the LGN or optic nerve, such multielectrode approaches will be necessary. However, related work to date in the optic nerve (Yan *et al* 2016) indicates that percepts are much more likely to involve nonlinear interactions between electrodes when visual space is represented in a disorganized 3D structure—requiring much more sophisticated modeling. In such cases, deep learning, *in silico*, neural networks may be the best approach (McIntosh *et al* 2016).

Stimulation thresholds

We have used the term 'subthreshold' pulses here to indicate single pulses that cannot independently drive responses. Nevertheless, by presenting a sequence of pulses that are integrated by the neuron to elicit a response, the neuron is driven above its threshold for activation. Thus, the sequence of subthreshold pulses can be considered to be a suprathreshold stimulus. We are not the first to make this observation that spreading stimulation out over extended time can reduce the stimulus amplitude necessary to elicit a response (Grumet *et al* 2000, Johnson *et al* 2004, Sekirnjak *et al* 2006, Ye *et al*
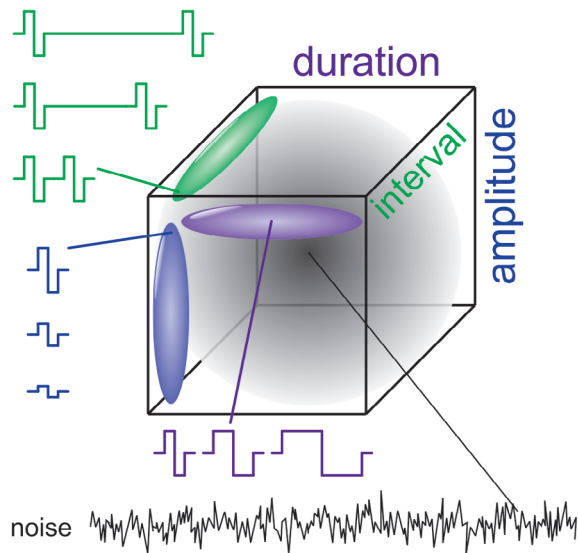
Figure 9. Noise samples stimulus space. Electrical stimuli are drawn from a high-dimensional space of parameters. Three such parameters for a train of pulses are amplitude, duration, and interpulse interval. White noise stimuli, however, draw randomly from this parameter space. (Adapted with permission from Rathbun and Hosseinzadeh (2017), figure 2.)

2008, Boinagrov *et al* 2010, Goo *et al* 2011, Eickenscheidt *et al* 2012, Samba *et al* 2015). In fact, this relationship underlies the classic strength-duration curve. However, we do differ slightly from the traditional understanding of the strength-duration relationship embodied in the Weiss and Lapicque equations (Rabinovitch *et al* 2016). In our approach, we seek to explicitly model the leakiness of integration through a finite temporal filter (e.g. Horsager *et al* (2009)). It is this leakiness that results in the asymptotic minimal stimulation threshold for arbitrarily long pulses (rheobase). We feel that shifting from thinking in terms of a single threshold charge with an asymptotic rheobase to thinking in terms of a threshold of the generator signal (integrated charge) for a neuron modeled with a finite temporal filter will prove more useful in characterizing the set of stimuli that are expected to drive a response from the retina.

Fading

An outstanding problem in artificial vision is fading—in which phosphenes tend to disappear with repeated stimulation at a constant level. The strength and speed of fading is proportional to the stimulation frequency. Perceptual fading has been reported in some Argus II subjects (Fornos *et al* 2010, Stronks *et al* 2013) and as well in Alpha-IMS subjects (Zrenner *et al* 2011, Stingl *et al* 2013). The latter patients overcame fading using relatively low stimulation rates of 1–20 bursts per second, but at the cost of visibly blinking percepts.

While it appears that fading has a strong cortical contribution, the desensitization of electrical responses in the retina due to repetitive stimulation has been investigated as one target to minimize fading. A common misconception of retinal desensitization is that pulse trains eliminate electrical

responses. In contrast, most reports of desensitization point to a marked reduction, but not elimination of electrical responses (Freeman and Fried 2011, Jensen and Rizzo 2007, Ryu *et al* 2009). Perhaps surprisingly, the subthreshold white noise stimulus we presented yielded robust, ongoing responses, despite being presented at a frequency of 25 Hz that is typically expected to induce strong desensitization. Likewise, others have confirmed that robust responses persist at high frequencies as long as the pulse amplitudes are modulated over time (Maturana *et al* 2018, Ho *et al* 2018). Desensitization typically compares pulse train responses to a single isolated pulse response (an atypical stimulation pattern for bionic vision applications). We suspect that the robust responses we and others have observed at high stimulation rates reflect the encoding of stimulation changes in the context of a saturated desensitization mechanism. In effect, this amounts to stimulating within the context of a fixed electrical adaptation state—the absence of which compounds typical studies on desensitization. Furthermore, we speculate that the use of primarily subthreshold pulses in such a sequence may further reduce the effects of desensitization. Whether low-amplitude pulse modulation can drive visual perception without engaging cortical fading remains an outstanding question of great interest.

Neural coding

An interesting yet unresolved issue, not only in retinal prosthetics but also in neuroscience at large, is the relative importance of firing rate versus the precise timing and pattern of individual spikes—rate coding versus temporal coding (Freeman *et al* 2011). Prostheses which target the retinal network (indirect RGC stimulation) tend to incorporate a presumption that the natural pattern of spikes generated by complex interactions in the network may be necessary for visual perception—a temporal code (Lee *et al* 2013, Im and Fried 2015, Im *et al* 2018). In contrast, in direct stimulation some investigators emphasize firing rate while others emphasize the temporal spiking pattern (Ryu *et al* 2011, Fried *et al* 2006). While indirect stimulation has the problem that precise control of the firing rate and pattern is difficult, direct stimulation necessitates an explicit model of visual encoding to employ temporal coding (e.g. Fried *et al* (2006)). Accordingly, because the spiking response to electrical stimulation could be encoded in both bursts and tonic spikes, it is important to consider such coding in calculating STAs. Here, we have briefly presented a method developed to account for the influence of burst coding on the STA. As more is learned about temporal coding in the retina, further modifications to the STA method may become necessary. An open question is whether burst spikes and tonic spikes convey distinct information about electrical stimulation of the retina.

Oscillations

Related to bursts, a common spiking pattern seen in degenerated retinas is subthreshold membrane oscillations which

strongly bias the timing of both tonic spikes and bursts toward the peak of the oscillation. Recent work has demonstrated that electrical stimulation can shift the phase of these oscillations, entraining subsequent burst cycles (Goo *et al* 2015, Haselier *et al* 2017). With respect to STAs, this poses a particular problem in that both the first volley of spikes driven by the electrical stimulus and subsequent entrained cycles will be reflected in the STA. Accordingly, we have seen evidence of such oscillations in the rd10 mouse retina (Sekhar *et al* 2017). In order to better depict the average stimulus that drives responses in the rd10 retina, it will be necessary to develop a method to separate contributions of the stimulus shape and the ongoing oscillations from the STA.

Building the model

Throughout this work, we have referred to a proposed modelling framework rather than an explicit model. This is because many of the important details of models falling within this framework may vary from model to model. Furthermore, many of the details for implementation of such models remain uncertain. In figure 1, we indicate that electrically-stimulated PR signals are passed synaptically to the BC where they are combined with electrical stimulation signals intrinsic to the BC. A similar process happens from BC to RGC. Nevertheless, we have remained agnostic as to how exactly these signals are combined. The relationship between depolarization and neurotransmitter release will entail a certain degree of nonlinearity owing to physiological limitations. Due to processes like consumption of the readily releasable pool of vesicles, this nonlinearity might have multiple kinetic parameters. Within the BC and RGC, it is unclear how direct stimulation and synaptic inputs will be weighted relative to one another. Additionally, it is unclear whether the two signals (BC electrical generator signal and PR synaptic input for BC; RGC generator signal and BC synaptic input for RGC) will be summed linearly or not.

Beyond refining the details of the proposed framework, we expect that a number of elaborations may be necessary. As noted in figure 5, retinal neurons can be stimulated through at least two distinct mechanisms. Traditionally, a single short stimulus greater than the threshold can be used to drive spikes at short latency from stimulus onset. Complementarily, if the stimulus is more subtle, an extended stimulus waveform that matches the electrical input filter can elicit a response. In the framework presented, we have assumed that all instantaneous stimuli are subthreshold and that only the integrative mechanism is engaged. This is useful since single pulse activation could complicate input filter estimation and obscure the fast filter of direct RGC stimulation and possibly even the BC indirect filter, depending on stimulus design. Another potential elaboration may be the need to incorporate higher order stimulus-response correlations. While the STA is a good estimate of the first order stimulus-response relationship, higher order interactions are well documented for visual stimulation. Yet another elaboration that may be necessary is the incorporation of a spike history feedback term. It is well known that

the Poisson distribution is an imperfect model for RGC spike train statistics. By incorporating a feedback term, effects like the refractory period, network inhibition, and post-inhibitory rebound can be reflected in the modeled spike train (Pillow *et al* 2005).

As implied above, it will be useful to continue to develop noise stimuli beyond the temporal noise our group has examined. Other groups have had recent success in combining both time and space. A continuing constraint however is achieving sufficient resolution in each dimension for full characterization of the spatiotemporal receptive field. Spatially, there is currently a limit on the order of 50 μm pitch for electrode spacing. An obstacle in the temporal domain is the need to record neural signals in the presence of electrical stimulation artifacts. While we would love to present our noise stimulus at 1 kHz rather than the 25 Hz we used, such high stimulation rates would obliterate the neural signal with artifacts. However, based on the temporal filtering expected for the primary cells of the retina (1–100 Hz), it may be possible to design a band-pass filtered noise stimulus that is effectively continuous in time—thus reducing artifact amplitudes enough to preserve the neural signals.

Finally, as explicit models are developed within this framework, it will become necessary to implement iterative model fitting. While we have presented the STA as an estimate of the electrical input filter, and the generator signal-firing rate curve as an estimate of the nonlinearity, these functions are only good first approximations. By simultaneously fitting these two functions as well as the synaptic parameters, spiking history feedback function, and possibly higher order stimulus-response correlation functions, the various elements of the model should come into sharper focus. Toward that end, a strong stimulus-response correlation is important. To date, we have found that our methods produce only modest correlations. By stimulating more strongly, while remaining within the subthreshold, integrative domain, it should be possible to drive more reliable responses that are still useful for the modeling described above.

Conclusions

Investigations of the retina's response to electrical stimulation have advanced significantly in the past twenty years. Recently, a growing body of work has sought to apply linear systems analysis to this domain. Of particular interest is the use of white noise stimuli to characterize the linear filtering behavior of the retina to electrical stimulation. We have proposed a modelling framework for such research that we hope may address ongoing challenges in bionic vision. By expressing stimulation of the retina in terms of integrated charge—taking into account the leaky memory of retinal neurons—a more useful understanding of the stimulation may be realized. Furthermore, by carefully measuring the spatio-temporal filtering properties of individual retinal ganglion cells, we expect that stimuli can be identified to selectively activate each of the approximately thirty different RGC types. Finally, modeling the temporal integration of the retina should enable the use

of lower amplitude stimuli that minimize retinal desensitization and reduce perceptual fading of bionic visual percepts. Ultimately, the linear systems framework is hypothesized to facilitate substantially improved bionic vision for future recipients of retinal prostheses.

Acknowledgments

Author contributions

DR drafted the manuscript. All authors contributed equally to the final text and figures.

Competing financial interests

DR has received surplus equipment on loan and minor support for supplies from Retina Implant AG. EZ is Advisor to Retina Implant AG, stock holder and co-inventor of patents held by this company. However, Retina Implant AG had no influence on the planning and execution of the work presented here.

We therefore declare no competing financial interests.

ORCID iDs

D L Rathbun https://orcid.org/0000-0001-7387-7944
N Ghorbani https://orcid.org/0000-0003-3867-0459
H Shabani https://orcid.org/0000-0003-2057-1364
E Zrenner https://orcid.org/0000-0003-2846-9663
Z Hosseinzadeh https://orcid.org/0000-0003-3407-7754

References

Adrian B Y E D and Matthews R 1927 THE action of light on the eye. Part II. The processes involved in retinal excitation *J. Physiol.* **64** 279–301

Baden T *et al* 2016 The functional diversity of retinal ganglion cells in the mouse *Nature* **529** 345–50

Bareket L *et al* 2017 Progress in artificial vision through suprachoroidal retinal implants *J. Neural Eng.* **14** 045002

Barlow H B 1953 Summation and inhibition in the frog's retina *J. Physiol.* **119** 69–88

Barriga-Rivera A *et al* 2017 Visual prosthesis: interfacing stimulating electrodes with retinal neurons to restore vision *Frontiers Neurosci.* **11** 620

Boiko T *et al* 2003 Functional specialization of the axon initial segment by isoform-specific sodium channel targeting *J. Neurosci.* **23** 2306–13

Boinagrov D *et al* 2014 Selectivity of direct and network-mediated stimulation of the retinal ganglion cells with epi-, sub- and intraretinal electrodes *J. Neural Eng.* **11** 026008

Boinagrov D, Loudin J and Palanker D 2010 Strength-duration relationship for extracellular neural stimulation: numerical and analytical models *J. Neurophysiol.* **104** 2236–48

Bonham B H and Litvak L M 2008 Current focusing and steering: modeling, physiology, and psychophysics *Hear. Res.* **242** 141–53

Bracewell R N 1986 *The Fourier Transform and its Applications* vol 31999 (New York: McGraw-Hill)

Brodie S E, Knight B W and Ratliff F 1978 The spatiotemporal transfer function of the limulus lateral eye *J. Gen. Physiol.* **72** 167–202

Chen S C *et al* 2009 Simulating prosthetic vision: I. Visual models of phosphenes *Vis. Res.* **49** 1493–506

Chichilnisky E J 2001 A simple white noise analysis of neuronal light responses *Netw. Comput. Neural Syst.* **12** 199–213

Cogan S F 2008 Neural stimulation and recording electrodes *Annu. Rev. Biomed. Eng.* **10** 275–309

Devries S H and Baylor D A 1997 Mosaic arrangement of ganglion cell receptive fields in rabbit retina *J. Neurophysiol.* **78** 2048–60

Dumm G *et al* 2014 Virtual electrodes by current steering in retinal prostheses *Investigative Ophthalmol. Vis. Sci.* **55** 8077–85

Eickenscheidt M and Zeck G 2014 Action potentials in retinal ganglion cells are initiated at the site of maximal curvature of the extracellular potential *J. Neural Eng.* **11** 036006

Eickenscheidt M *et al* 2012 Electrical stimulation of retinal neurons in epiretinal and subretinal configuration using a multicapacitor array *J. Neurophysiol.* **107** 2742–55

Enroth-Cugell C and Robson J G 1966 The contrast sensitivity of retinal ganglion cells of the cat *J. Physiol.* **187** 517–52

Esler T B *et al* 2018 Biophysical basis of the linear electrical receptive fields of retinal ganglion cells *J. Neural Eng.* **15** 55001

Fornos A P, Sommerhalder J and Pelizzone M 2010 Dynamics of visual perception upon electrical stimulation of the retina *Investigative Ophthalmol. Vis. Sci.* **51** 3027

Franke K *et al* 2017 Inhibition decorrelates visual feature representations in the inner retina *Nature* **542** 439–44

Freeman D K and Fried S I 2011 Multiple components of ganglion cell desensitization in response to prosthetic stimulation *J. Neural Eng.* **8** 016008

Freeman D K *et al* 2010a Selective activation of neuronal targets with sinusoidal electric stimulation *J. Neurophysiol.* **104** 2778–91

Freeman D K, Rizzo J F and Fried S I 2010b Electric stimulation with sinusoids and white noise for neural prostheses *Front. Neurosci.* **4** 28

Fried S I *et al* 2009 Axonal sodium-channel bands shape the response to electric stimulation in retinal ganglion cells *J. Neurophysiol.* **101** 1972–87

Fried S I, Hsueh H A and Werblin F S 2006 A method for generating precise temporal patterns of retinal spiking using prosthetic stimulation *J. Neurophysiol.* **95** 970–8

Goetz G *et al* 2015 Contrast sensitivity with a subretinal prosthesis and implications for efficient delivery of visual information *Investigative Ophthalmol. Vis. Sci.* **56** 7186–94

Goo Y S *et al* 2011 Retinal ganglion cell responses to voltage and current stimulation in wild-type and rd1 mouse retinas *J. Neural Eng.* **8** 035003

Goo Y S *et al* 2015 Spontaneous oscillatory rhythms in the degenerating mouse retina modulate retinal ganglion cell responses to electrical stimulation *Front. Cell. Neurosci.* **9** 512

Granit R 1946 The distribution of excitation and inhibition in single-fibre responses from a polarized retina *J. Physiol.* **105** 45–53

Greenberg R J *et al* 1999 A computational model of electrical stimulation of the retinal ganglion cell *IEEE Trans. Biomed. Eng.* **46** 505–14

Grumet A E, Wyatt J L J and Rizzo J F III 2000 Multi-electrode stimulation and recording in the isolated retina *J. Neurosci. Methods* **101** 31–42

Guo T *et al* 2014 Selective activation of ON and OFF retinal ganglion cells to high-frequency electrical stimulation: a computational modeling study *Conf. Proc. IEEE Eng. Med. Biol. Soc. 2014* pp 6108–11

Guo T *et al* 2018 Closed-loop efficient searching of optimal electrical stimulation parameters for preferential excitation of retinal ganglion cells *Frontiers Neurosci.* **12** 168

Halupka K 2017 Prediction and shaping of visual cortex activity for retinal prostheses *PhD Thesis* University of Melbourne (http://hdl.handle.net/11343/191701)

Halupka K J *et al* 2017 Neural responses to multielectrode stimulation of healthy and degenerate retina *Investigative Ophthalmol. Vis. Sci.* **58** 3770–84

Hartline H K 1938 The response of single optic nerve fibers of the vertebrate eye to illumination of the retina *Am. J. Physiol.* **121** 400–15

Haselier C *et al* 2017 Correlations between specific patterns of spontaneous activity and stimulation efficiency in degenerated retina *PLoS One* **12** e0190048

Ho E *et al* 2018 Spatiotemporal characteristics of retinal response to network-mediated photovoltaic stimulation *J. Neurophysiol.* **119** 389–400

Horsager A *et al* 2009 Predicting visual sensitivity in retinal prosthesis patients *Investigative Ophthalmol. Vis. Sci.* **50** 1483–91

Hosseinzadeh Z *et al* 2018 The spatial extent of epiretinal electrical stimulation in the healthy mouse retina *NeuroSignals* **25** 15–25

Hubel D H and Wiesel T N 1961 Integrative action in the cat's lateral geniculate body *J. Physiol.* **155** 385–98

Humayun M S *et al* 1999 Pattern electrical stimulation of the human retina *Vis. Res.* **39** 2569–76

Im M and Fried S I 2015 Indirect activation elicits strong correlations between light and electrical responses in ON but not OFF retinal ganglion cells *J. Physiol.* **593** 3577–96

Im M and Fried S I 2016 Temporal properties of network-mediated responses to repetitive stimuli are dependent upon retinal ganglion cell type *J. Neural Eng.* **13** 025002

Im M, Werginz P and Fried S I 2018 Electric stimulus duration alters network-mediated responses depending on retinal ganglion cell type *J. Neural Eng.* **15** 36010

Jalligampala A *et al* 2017 Optimal voltage stimulation parameters for network-mediated responses in wild type and rd10 mouse retinal ganglion cells *J. Neural Eng.* **14** 026004

Jeng J *et al* 2011 The sodium channel band shapes the response to electric stimulation in retinal ganglion cells *J. Neural Eng.* **8** 036022

Jensen R J *et al* 2003 Thresholds for activation of rabbit retinal ganglion cells with an ultrafine, extracellular microelectrode *Investigative Ophthalmol. Vis. Sci.* **44** 3533–43

Jensen R J and Rizzo J F 2007 Responses of ganglion cells to repetitive electrical stimulation of the retina *J. Neural Eng.* **4** S1–6

Jepson L H *et al* 2014 Spatially patterned electrical stimulation to enhance resolution of retinal prostheses *J. Neurosci.* **34** 4871–81

Johnson L *et al* 2004 Electrical stimulation of isolated retina with microwire glass electrodes *J. Neurosci. Methods* **137** 265–73

Korenberg M J and Hunter I W 1986 The identification of nonlinear biological systems: LNL cascade models *Biol. Cybern.* **55** 125–34

Kuffler S W 1953 Discharge patterns and functional organization of mammalian retina *J. Neurophysiol.* **16** 37–68

Lee S W, Eddington D K and Fried S I 2013 Responses to pulsatile subretinal electric stimulation: effects of amplitude and duration *J. Neurophysiol.* **109** 1954–68

Lorach H *et al* 2015 Photovoltaic restoration of sight with high visual acuity *Nat. Med.* **21** 476–82

Marmarelis P Z and Naka K 1972 White-noise analysis of a neuron chain: an application of the Wiener theory *Science* **175** 1276–8

Marmarelis P Z and Naka K I 1973a Nonlinear analysis and synthesis of receptive-field responses in the catfish retina. I. Horizontal cell leads to ganglion cell chain *J. Neurophysiol.* **36** 605–18

Marmarelis P Z and Naka K I 1973b Nonlinear analysis and synthesis of receptive-field responses in the catfish retina. II. One-input white-noise analysis *J. Neurophysiol.* **36** 619–33

Marmarelis P Z and Naka K I 1973c Nonlinear analysis and synthesis of receptive-field responses in the catfish retina. III. Two-input white-noise analysis *J. Neurophysiol.* **36** 634–48

Masland R H 2011 Cell populations of the retina: the Proctor lecture *Investigative Ophthalmol. Vis. Sci.* **52** 4581–91

Matteucci P B *et al* 2013 Current steering in retinal stimulation via a quasimonopolar stimulation paradigm *Investigative Ophthalmol. Vis. Sci.* **54** 4307–20

Maturana M I *et al* 2016 A Simple and accurate model to predict responses to multi-electrode stimulation in the retina *PLoS Comput. Biol.* **12** e1004849

Maturana M I *et al* 2018 Electrical receptive fields of retinal ganglion cells: influence of presynaptic neurons *PLoS Comput. Biol.* **14** e1005997

McIntosh L T *et al* 2016 Deep learning models of the retinal response to natural scenes *Adv. Neural Inf. Process. Syst.* **29** 1369–77 (PMID: 28729779)

Moore B D *et al* 2013 Spatiotemporal flow of information in the early visual pathway *Eur. J. Neurosci.* **39** 593–601

Morse R P and Evans E F 1996 Enhancement of vowel coding for cochlear implants by addition of noise *Nat. Med.* **2** 928–32

Motz H and Rattay F 1986 A study of the application of the Hodgkin–Huxley and the Frankenhaeuser–Huxley model for electrostimulation of the acoustic nerve *Neuroscience* **18** 699–712

Nanduri D *et al* 2008 Retinal prosthesis phosphene shape analysis *Conf. Proc. IEEE Eng. Med. Biol. Soc. 2008* pp 1785–8

Nanduri D *et al* 2012 Frequency and amplitude modulation have different effects on the percepts elicited by retinal stimulation *Investigative Ophthalmol. Vis. Sci.* **53** 205–14

Paninski L, Pillow J and Lewi J 2007 Statistical models for neural encoding, decoding, and optimal stimulus design *Prog. Brain Res.* **165** 493–507

Pillow J W *et al* 2005 Prediction and decoding of retinal ganglion cell responses with a probabilistic spiking model *J. Neurosci.* **25** 11003–13

Qin W *et al* 2017 Single-compartment models of retinal ganglion cells with different electrophysiologies *Network* **28** 74–93

Rabinovitch A *et al* 2016 The Weiss–Lapicque and the Lapicque–Blair strength—duration curves revisited *Biomed. Phys. Eng. Express* **2** 015019

Rathbun D L 2009 *Spike Timing and Information Transmission at the Retinogeniculate Synapse* (Davis: University of California)

Rathbun D L and Hosseinzadeh Z 2017 Die netzhaut kitzeln *Systembiologie.de* **12** 13–7

Ringach D and Shapley R 2004 Reverse correlation in neurophysiology *Cogn. Sci.* **28** 147–66

Rizzo J F 2003 Methods and perceptual thresholds for short-term electrical stimulation of human retina with microelectrode arrays *Investigative Ophthalmol. Vis. Sci.* **44** 5355–61

Rizzo J F *et al* 2003 Perceptual efficacy of electrical stimulation of human retina with a microelectrode array during short-term surgical trials *Investigative Ophthalmol. Vis. Sci.* **44** 5362–9

Rodieck R W 1965 Quantitative analysis of cat retinal ganglion cell response to visual stimuli *Vis. Res.* **5** 583–601

Ryu S B *et al* 2009 Electrically-evoked neural activities of rd1 mice retinal ganglion cells by repetitive pulse stimulation *Korean J. Physiol. Pharmacol.* **13** 443–8

Ryu S B *et al* 2011 Decoding of temporal visual information from electrically evoked retinal ganglion cell activities in photoreceptor-degenerated retinas *Invest. Ophthalmol. Vis. Sci.* **52** 6271–8

Ryu S B *et al* 2017 Amplitude modulation-based electrical stimulation for encoding multipixel spatiotemporal visual information in retinal neural activities *J. Korean Med. Sci.* **32** 900–7

Samba R, Herrmann T and Zeck G 2015 PEDOT-CNT coated electrodes stimulate retinal neurons at low voltage amplitudes and low charge densities *J. Neural Eng.* **12** 16014

Savage C O *et al* 2012 Can electric current steering be used to control perception of a retinal prosthesis patient *Conf. Proc. IEEE Eng. Med. Biol. Soc. 2012* pp 3013–6

Schwartz O *et al* 2006 Spike-triggered neural characterization *J. Vis.* **6** 484–507

Sekhar S *et al* 2016 Tickling the retina: integration of subthreshold electrical pulses can activate retinal neurons *J. Neural Eng.* **13** 1–9

Sekhar S *et al* 2017 Correspondence between visual and electrical input filters of on and off mouse retinal ganglion cells *J. Neural Eng.* **14** 046017

Sekirnjak C *et al* 2006 Electrical stimulation of mammalian retinal ganglion cells with multielectrode arrays *J. Neurophysiol.* **95** 3311–27

Shapley R and Lennie P 1985 Spatial frequency analysis in the visual system *Annu. Rev. Neurosci.* **8** 547–83

Sharpee T O 2013 Computational identification of receptive fields *Annu. Rev. Neurosci.* **36** 103–20

Sim S L *et al* 2014 Simultaneous recording of mouse retinal ganglion cells during epiretinal or subretinal stimulation *Vis. Res.* **101** 41–50

Spencer T C, Fallon J B and Shivdasani M N 2018 Creating virtual electrodes with 2D current steering *J. Neural Eng.* **15** 35002

Stett A *et al* 2000 Electrical multisite stimulation of the isolated chicken retina *Vis. Res.* **40** 1785–95

Stett A, Mai A and Herrmann T 2007 Retinal charge sensitivity and spatial discrimination obtainable by subretinal implants: key lessons learned from isolated chicken retina *J. Neural Eng.* **4** S7–16

Stingl K T K *et al* 2013 Artificial vision with wirelessly powered subretinal electronic implant alpha-IMS *Proc. R. Soc.* B **280** 1–8

Stronks H C, Barry M P and Dagnelie G 2013 Electrically elicited visual evoked potentials in Argus II retinal implant wearers *Investigative Ophthalmol. Vis. Sci.* **54** 3891–901

Stutzki H *et al* 2016 Subretinal electrical stimulation reveals intact network activity in the blind mouse retina *J. Neurophysiol.* **116** 1684–93

Tsai D *et al* 2011 Responses of starburst amacrine cells to prosthetic stimulation of the retina *Conf. Proc. IEEE Eng. Med. Biol. Soc. 2011* pp 1053–6

Twyford P and Fried S 2016 The retinal response to sinusoidal electrical stimulation *IEEE Trans. Neural Syst. Rehabil. Eng.* **24** 413–23

Weiland J D, Walston S T and Humayun M S 2016 Electrical stimulation of the retina to produce artificial vision *Annu. Rev. Vis. Sci.* **14** 273–94

Weitz A C *et al* 2015 Improving the spatial resolution of epiretinal implants by increasing stimulus pulse duration *Sci. Transl. Med.* **7** 318ra203

Werginz P, Fried S I and Rattay F 2014 Influence of the sodium channel band on retinal ganglion cell excitation during electric stimulation—a modeling study *Neuroscience* **266** 162–77

Wohrer A and Kornprobst P 2009 Virtual Retina: a biological retina model and simulator, with contrast gain control *J. Comput. Neurosci.* **26** 219–49

Wollner D A and Catterall W A 1986 Localization of sodium channels in axon hillocks and initial segments of retinal ganglion cells *Proc. Natl Acad. Sci. USA* **83** 8424–8

Wong R C S *et al* 2012 Intrinsic physiological properties of rat retinal ganglion cells with a comparative analysis *J. Neurophysiol.* **108** 2008–23

Yan Y *et al* 2016 Electrically evoked responses in the rabbit cortex induced by current steering with penetrating optic nerve electrodes *Investigative Ophthalmol. Vis. Sci.* **57** 6327–38

Ye J H *et al* 2008 Functional connectivity map of retinal ganglion cells for retinal prosthesis *Korean J. Physiol. Pharmacol.* **12** 307–14

Zrenner E 2002 The subretinal implant: can microphotodiode arrays replace degenerated retinal photoreceptors to restore vision? *Ophthalmologica* **21 6** 8–20

Zrenner E 2013 Fighting blindness with microelectronics *Sci. Transl. Med.* **5** 210ps16

Zrenner E *et al* 2011 Subretinal electronic chips allow blind patients to read letters and combine them to words *Proc. R. Soc.* B **278** 1489–97